FATIGUE BEHAVIOR OF AN ADVANCED MELT-INFILTRATED SIC/SIC COMPOSITE AT 1200˚C IN AIR AND IN STEAM

THESIS

Boucher, Nicholas, Captain, USAF
AFIT-ENY-MS-17-M-242

DEPARTMENT OF THE AIR FORCE
AIR UNIVERSITY

AIR FORCE INSTITUTE OF TECHNOLOGY

Wright-Patterson Air Force Base, Ohio

AFIT-ENY-MS-17-M-242

FATIGUE BEHAVIOR OF AN ADVANCED MELT-INFILTRATED SIC/SIC COMPOSITE AT 1200˚C IN AIR AND IN STEAM

THESIS

Presented to the Faculty

Department of Aeronautical and Astronautical Engineering

Graduate School of Engineering and Management

Air Force Institute of Technology

Air University

Air Education and Training Command

In Partial Fulfillment of the Requirements for the

Degree of Master of Science in Material Science and Engineering

Nicholas J. Boucher, B.S.

Captain, USAF

March 2017

AFIT-ENY-MS-17-M-242

FATIGUE BEHAVIOR OF AN ADVANCED MELT-INFILTRATED SIC/SIC COMPOSITE AT 1200˚C IN AIR AND IN STEAM

Nicholas J. Boucher, B.S.

Captain, USAF

Committee Membership:

Marina B. Ruggles-Wrenn, PhD

Chair

Craig Przybyla, PhD

Member

Thomas Eason, PhD

Member

Abstract

The tension-tension fatigue behavior of an advanced melt-infiltrated (MI) silicon carbide/silicon carbide (SiC/SiC) ceramic matrix composite (CMC) was investigated at 1200°C in air and in steam. The MI composite consisted of ten 0/90 plies of Hi-Nicalon™ SiC fibers woven in a five harness satin weave (5HSW). The fibers were coated with boron nitride coating applied using chemical vapor infiltration (CVI) to provide a weak fiber-matrix interphase. The weave was coated with a CVI SiC matrix layer followed by infiltration with SiC particulate slurry and molten silicon. Nine tensile specimens of the material were used in a pilot investigation of mechanical performance at elevated temperature. One specimen was used in a monotonic tensile test at 1200°C in air to determine tensile properties. The remaining specimens were tested in tension-tension fatigue; four were tested in air and four in steam. Tests were performed at 1200°C at 1.0 Hz with a stress ratio of minimum to maximum stress of R=0.05. Maximum stress ranged from 120 to 160 MPa in air and from 100 to 120 MPa in steam. Fatigue run-out was defined as 2×10^5 cycles. All specimens that achieved fatigue run-out were tested in tension to failure to evaluate retained strength and modulus. Strain accumulation and changes in modulus with cycles were measured to qualitatively evaluate damage development. The fatigue life was shorter in steam with a fatigue limit between 110 and 120 MPa. The fatigue limit in air was between 120 and 130 MPa. Specimens that achieved fatigue run-out retained 83-97% of their tensile strength. Post-test microstructure of the composite was examined in order to study damage and failure mechanisms.

Acknowledgments

Research efforts of any scale are impossible to do alone. I wouldn't be able to succeed without the genuine good will of the technicians at AFIT and AFRL, especially Jamie, Josh, Tommy and Kathleen. My lab mates, Tom and Ronnie, were a great resource for bouncing ideas off of. Having other students go through similar thesis work lent a feeling of camaraderie to our efforts. I would like to thank my wife who supported me through the heavy coursework and late nights of draft revision. Of course, I would like to thank Dr. Ruggles-Wrenn for her attention to detail, passion for science, and guidance.

Table of Contents

List of Figures

List of Tables

FATIGUE BEHAVIOR OF AN ADVANCED MELT-INFILTRATED SIC/SIC COMPOSITE AT 1200˚C IN AIR AND IN STEAM

I. Introduction

The success of future aircraft in the US Air Force depends on increasing their performance while reducing their fuel consumption. Operational requirements demand that more energy must be extracted from every pound of fuel, which means the engine must be more thermally efficient. The efficiency of an ideal heat engine is given by

$$\eta = \frac{T_1 - T_2}{T_1} = 1 - \frac{T_C}{T_H}$$

Where T_1 is the engine source temperature (hot temperature) and T_2 is the sink temperature, or cold temperature [1]. To maximize efficiency, engines must operate at higher temperatures. A standard turbine is capable of reaching temperatures over 2100°C [2], but its nickel-based superalloy turbine blades are limited to a temperature of 1100°C with film cooling [3]. These alloys have provided steady gains in aircraft performance, as shown in Figure 1, but they require forced-air cooling to avoid melting. These cooling systems have reached a performance limit, since any further introduction of cooling air will start to reduce the combustor temperature [4].

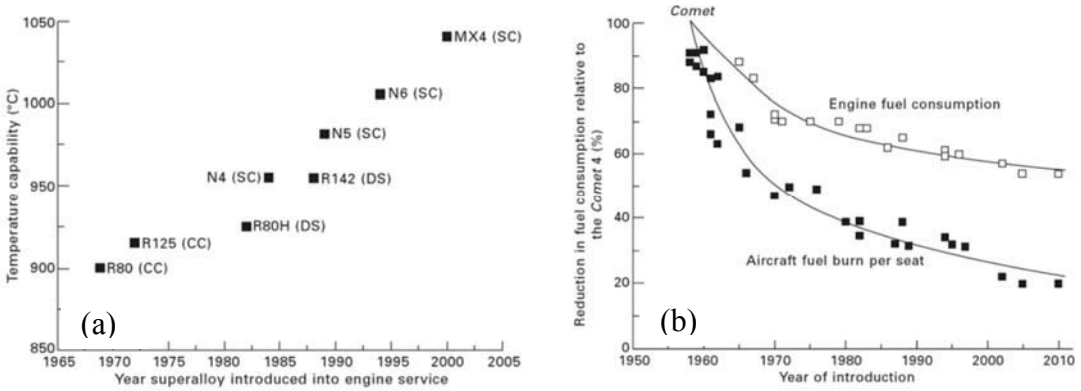

Figure 1: (a) Temperature capability of Nickel alloys; and (b) reduction of fuel consumption corresponding to year of alloy introduction [5]

New materials are now needed continue the trend of higher operating temperatures. Ceramic and refractory materials are capable of withstanding the environment of a combustor, and are up to four times less dense than nickel alloys. They do not need the heavy and complex cooling systems currently used to force cooling air into the turbine rotors. However, they do not have the required toughness to survive hundreds of hours and thousands of cycles that engine components sustain [4], [6]. To solve this dilemma, engineers have been studying ceramic matrix composites (CMCs) for use in aircraft engines. These materials have a toughness advantage over bulk ceramics from the addition of a secondary toughening phase. The inclusion of fibers, particles or whiskers slows brittle fracture of the ceramic. However, the complex failure mechanisms in these materials make it hard to predict the fatigue life. Extensive testing is done to ensure that the laminate can maintain strength, stoichiometry, and oxidation resistance at elevated temperatures while undergoing fatigue cracking [7]. Engineers must better understand the fabrication and performance of these materials before using them to meet the strict reliability requirements of gas turbine engines. Work has already been done on testing full-scale components made of CMC, such as nose cones for space vehicles, combustion chamber liners, and nozzles for high-temperature engines [8], [9]. Questions about whether or not a material is suitable for a particular application will not be the focus of this of this research. The purpose of this research is to evaluate a melt-infiltrated (MI) silicon carbide fiber/silicon carbide matrix (SiC/SiC) CMC at 1200°C in air and steam to determine its tensile, fatigue, and microstructural properties in representative oxidizing environments in order to objectively compare it to prior work on earlier generations of CMCs.

II. Background

2.1 Ceramic Materials

Ceramic materials have long been known to be chemically inert, stiff, abrasion resistant, and stable at high temperature due to the ionic character of its atomic bonding. However, this same property at the atomic level inhibits large-scale dislocation motion seen in metals, schematically shown in Figure 2.

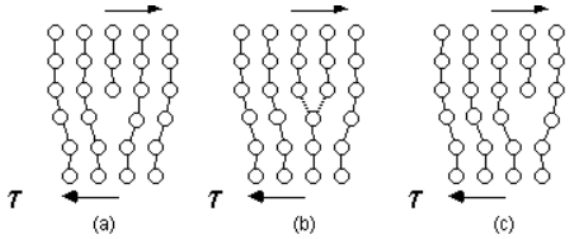

Figure 2: Generalized dislocation motion in a lattice [10]

The stress needed for dislocation movement, or Pierels stress, is much higher in ceramics due to the strength of the bonds [10]. There is more resistance to plastic flow in the material, so cracks in the material can propagate rapidly and catastrophically [11]. The properties of a few engineering ceramics, including fracture toughness, are listed in Table 1. Note the comparison to the nickel-based superalloy, Inconel 600.

Table 1: Properties of select engineering ceramics [12]

	Density [g/cc]	**Elastic Modulus** [GPa]	**Flexural Strength** [MPa]	**Tensile Strength** [MPa]	**Fracture Toughness** [Mpa√m]	**Max Temperature in air** [°C]
Silicon Carbide	3.21	476	324	310	4	1400
Silicon Nitride	3.31	317	679 - 896	360 - 434	5.0 - 8.0	1500
Aluminum Nitride	3.25	308	428	233.5	3.5	1600
Boron Carbide	2.51	445	375	155	3	750 - 1700
Boron Nitride	2.28	675	51.8	2.41	2.6	985
Alumina	3.7 - 3.97	393	310 - 379	260 - 300	4.5	1750
Zirconia	6.04	207	900	248	13	500
Nickel Superalloy (Inconel 600)	8.47	200	--	550-700	~ 100	1200

Monolithic ceramic materials are fabricated using powder sintering techniques, reaction forming, hot pressing, or chemical vapor deposition [13]. Ceramics generally perform better when there are fewer defects such as voids introduced in processing, as these can initiate cracking under cyclic loading. While this is of particular concern in the sintering of ceramics, in which uniform particles are hot pressed together, the same flaws can be introduced during any of the high-temperature processing methods [14, p. 542]. The inability to carefully control the flaw distribution leads to variability in the fracture strength of these materials, limiting their use in applications that have strict requirements for fatigue and creep performance [15].

Starting materials	Method	Product
Gases	Chemical vapor deposition	Films, monoliths
Gas–liquid	Directed metal oxidation	Monoliths
Gas–solid	Reaction bonding	Monoliths
Liquid–solid	Reaction bonding	Monoliths
Liquids	Sol–gel process	Films, fibers
	Polymer pyrolysis	Fibers, films
Solids (powders)	Melt casting	Monoliths
	Sintering of powders	Monoliths, films

Figure 3: Common ceramic fabrication techniques [13]

The greatest drawback to overcome when designing structures using monolithic ceramics is their vulnerability to catastrophic failure, so they are commonly used in applications where high toughness is not required, or where fractured material can be easily replaced, such as furnace liners and leading edge tiles on high-velocity aircraft. The moving components in the hot section of the engine that have the more stringent requirements must be much more damage tolerant. A full 70% of aircraft engine repair costs are material costs [16]. Introducing a ceramic material with a fracture toughness as as low as 5 kPa$\sqrt{m}$ would be disastrous in this application. Nature does not provide a suitable alternative, though in the case of Zirconia (ZrO_2), a transformation mechanism can operate in the grains, in which stress ahead of a crack tip causes a local increase in volume, inducing a phase change that absorbs energy and drastically increases the toughness of the material [17]. Using a similar concept, a secondary ceramic phase can be added to a bulk material to increase its toughness.

2.2 Composites

The term “composite” refers to a wide range of engineered materials that combine two or more components that differ in structure or chemistry in order to combine their useful properties while avoiding their individual drawbacks [4]. The constituents retain their material properties

when combined in the composite; i.e., they do not react chemically [18]. Typically when referring to composites, polymer-matrix composites such as carbon-fiber reinforced polymer (CFRP) come to mind. This material uses multiple layers, or plies, of woven carbon fibers bound together with a resin to form a strong, lightweight material. The plies consist of fiber strands, or tows, woven together with a specific pattern as illustrated in Figure 4.

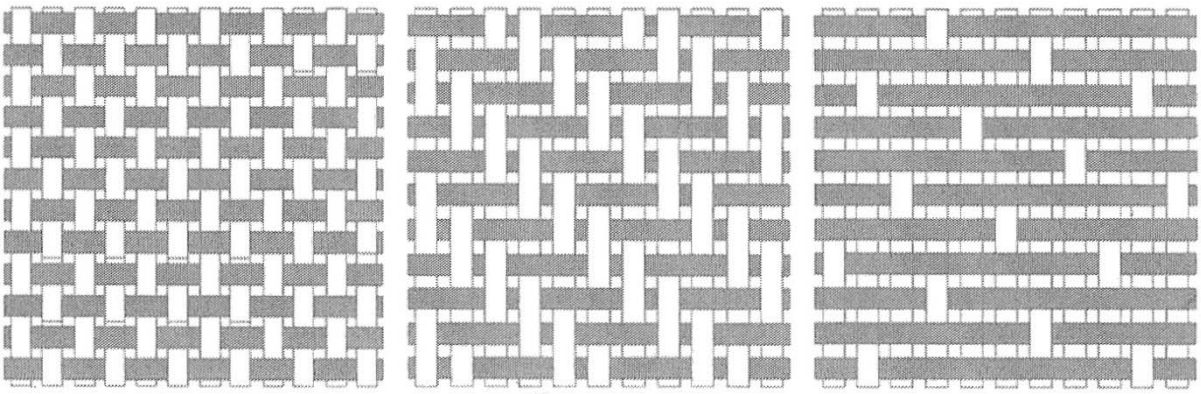

Figure 4: Examples of fabric weave styles (left to right) : (a) plain weave, (b) 2x2 twill, and (c) eight-harness satin weave [19]

In a typical polymer matrix composite, the bond between the fibers and the matrix must be as strong as possible in order to transfer load to the fiber material. The properties of the fibers dominate the performance of the material. The composite approach can be extended to ceramics, but it is done with an emphasis on increasing toughness rather than ultimate tensile strength. Like polymers, ceramics can be fabricated into thin, flexible fibers, and bonded together in a ceramic matrix. However, the fiber and matrix are both high-modulus, brittle materials. In some cases, such as SiC/SiC CMC, the constituents are the same material. The intent of composite design in this case is to introduce energy dissipating mechanisms rather than direct strengthening of a matrix material [11].

2.3 Ceramic Matrix Composites

2.3.1 General Information

Ceramic-matrix composites were developed to take advantage of the high-temperature and chemical-resistant properties of the material while overcoming the low fracture toughness of bulk ceramic. Unlike polymer-matrix or even metal-matrix composites, the reinforcing phase is not used for additional strength, but rather as a method to slow crack growth. Toughening can be accomplished by slowing crack growth ahead of the crack propagation direction, or by bridging the crack after it opens [20]. Deflection ahead of the crack is achieved through the use of ductile particles, which absorb strain energy at the crack tip. Bridging can be accomplished by incorporating fibers or whiskers into the matrix. The discussion here will be on the performance of a continuous fiber-reinforced CMC in which both the fiber and matrix are silicon carbide.

Since the fiber and matrix have roughly the same modulus and strength, transferring the maximum amount of load from the matrix to the fiber through a strong bond is not the goal of reinforcement. A strong bond allows cracks that form in the matrix to propagate through the fibers. A strong bond between the constituents creates a solid ceramic that is no different from bulk material. If the bond is weak, the crack propagates around the reinforcement, and the fiber slides along the interface with the matrix. This crack bridging and fiber sliding slows the strain energy release as the fracture surfaces form, giving the ceramic a quasi-ductile behavior [11]. At the matrix cracking stress, the material exhibits softening as cracks begin to propagate through the matrix. Deflection occurs multiple ways. Once cracks reach a fiber, load is transferred to the fiber, which can be considered as applying a closure force to the crack. Then, the crack can progress along the fiber/matrix interface, which is called progressive debonding. Alternatively, the crack propagates around the fiber and continues. Load is increasingly transferred to the fibers

by friction at the interface until fibers begin to fail. When 15%-30% of the fibers in the cross section have failed, the maximum strength is reached. Here, the maximum load has been transferred to the remaining fibers, which can support no more load, and fail [21]. A schematic of the tensile behavior of fiber-toughened material is shown in Figure 5.

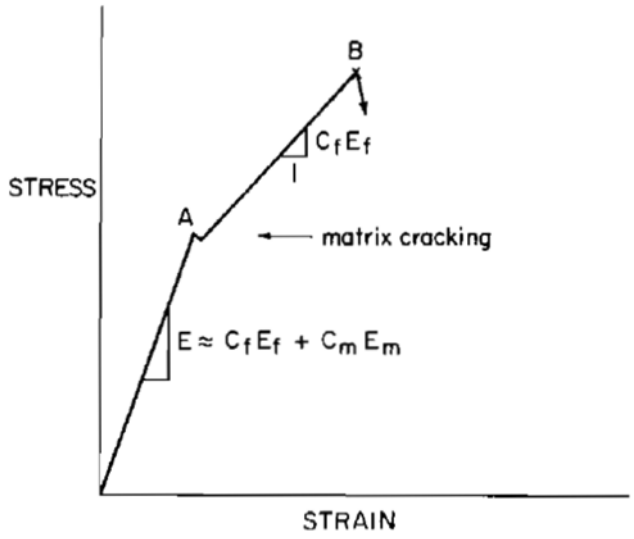

Figure 5: Schematic of (A) matrix cracking stress and (B) ultimate fiber failure [22]

In fiber-toughened CMCs, a weak fiber/matrix bond is enabled through two different mechanisms. The first is by using a porous matrix, which prevents the fibers from being subjected to a stress singularity at the interface. The second method is using a strong matrix with a weak interphase material at the interface, which is preferred due to the higher strength of the matrix overall [23]. Boron Nitride (BN) and pyrolytic carbon (PyC) are typically used as the interface material due to their layered graphitic structure. This facilitates microcracking in the interphase without propagating the crack through the fiber due to the anisotropy of the layered material [11]. Figure 6 illustrates this phenomenon. With enhanced fracture toughness, CMCs become an extremely attractive material for high-temperature applications requiring long life

components. Figure 7 illustrates the comparative strength retention of CMCs against other engineering materials.

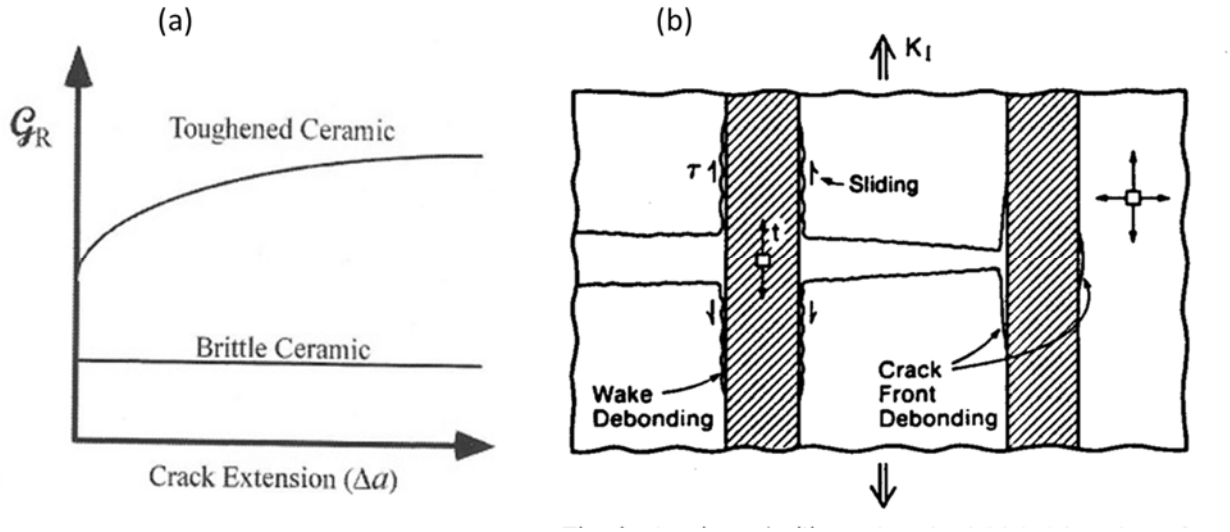

Figure 6: (a) The strain energy needed to grow the crack increases as the fibers bridge, unlike bulk ceramic that is susceptible to fast fracture [20], (b) fiber bridging in the crack wake and crack deflection [24]

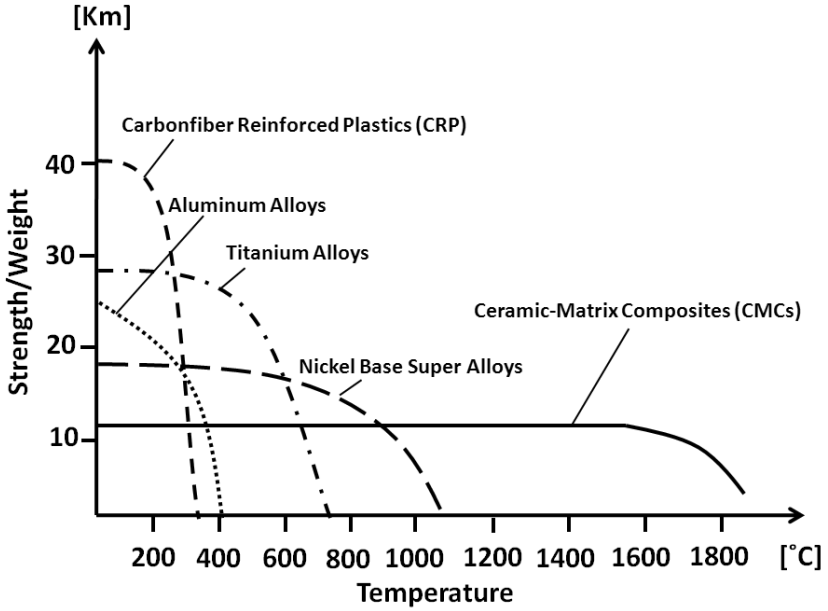

Figure 7: Retained strength at temperature [25]

2.3.2 Oxide and Non-Oxide CMCs

Since CMCs are intended for use at high temperatures, oxidation is a primary concern for performance. Both oxide and non-oxide ceramics can be fashioned into composites. Oxide materials have a primary advantage of already being oxidized. The most commonly used materials in this family are alumina or alumina-silicate materials. They can perform at high temperatures and have an initial high tensile strength [26] . However, these materials are prone to creep due to their fine grain structure required for fiber flexibility [27]. Non-oxide ceramics, on the other hand, are more resistant to creep, but the material and particularly the fibers must be protected against oxidation [28].

Since SiC is a non-oxide, it is prone to oxidation. Active oxidation, schematically shown in Figure 8, results in removal of material and weakening of the fibers. It occurs at low pressure according to $SiC + O_2 \rightarrow SiO_2 + CO$. Passive oxidation resulting in the buildup of an oxide layer proceeds at higher partial pressure according to $2SiC + 3O_2 \rightarrow 2SiO_2 + 2CO$. Oxidation continues through the SiO_2 layer in a similar manner to other oxides, meaning the oxygen in the environment diffuses through the layer and contacts the SiC beneath, and the products of the reaction diffuse back out through the oxide layer. However, the buildup of a cohesive silica layer at the surface does provide protection by slowing down the active oxidation process [29].

In a high-temperature environment, the interphase that gives a CMC its desired properties is also subject to erosion and oxidation. As the matrix cracks under stress, the oxidizing elements can penetrate the material and attack the fibers. The interphase, particularly in the case of boron nitride, can serve a second purpose by forming an amorphous borosilicate layer that “heals” the cracking and somewhat prevents further ingress of the environment. However, the BN interphase can be consumed by the formation of B_2O_3 which escapes as a gas above 1000°C in air, or lower

temperatures in steam [30]. The oxidation behavior of the fiber, interphase, and matrix materials has a profound impact on the performance of the composite in fatigue.

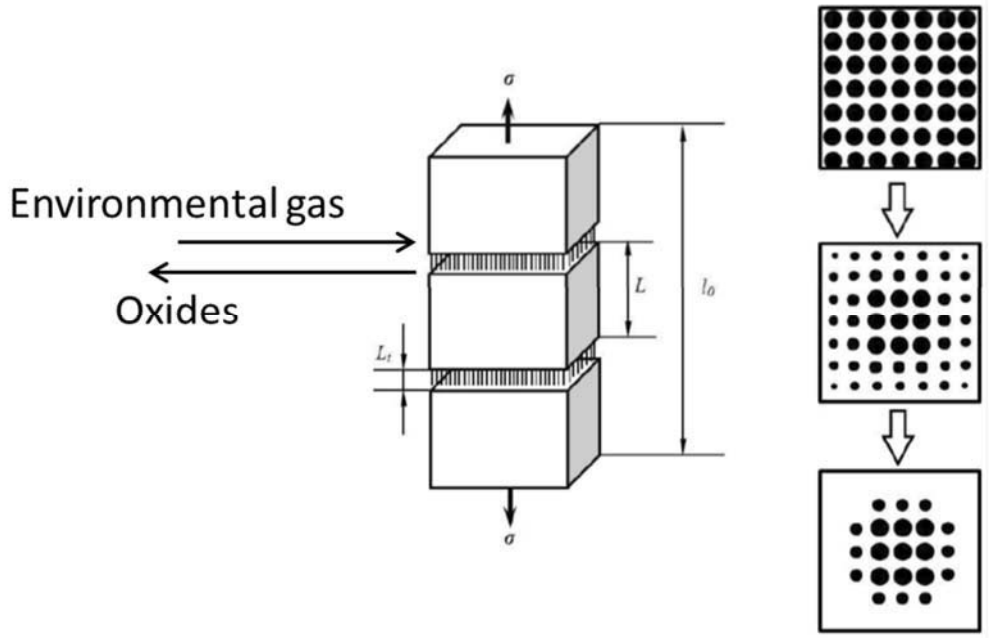

Figure 8: Model of active fiber oxidation in a C/SiC composite showing ingress of environmental gas through cracking, and reduction of fiber load-bearing cross section [31]

2.3.3 Melt-Infiltrated CMCs

Silicon melt infiltration (SMI) is a fabrication method that can densify the composite material in one step and typically produces a more dense final product than those produced through chemical vapor infiltration (CVI). The CMC melt-infiltration procedure involves introducing a liquid slurry of silicon into a woven preform, where it reacts with free carbon to form silicon-carbide [14]. The fibers must be protected with a coating against the high temeprature liquid to preserve their stoichiometery. Boron nitride or an overcoating of carbon can be used for this purpose on Hi-Nicalon™ fibers intended for applications in high temperatures or oxidizing atmosphere [8]. An additional overcoating of 0.5 to 5 um of SiC or Si_3N_4 is applied to protect the BN from liquid silicon infiltration and to partially densify the

green body before infiltration. Preforms are then heated and infiltrated by precursor carbon and SiC particles. Finally, the liquid Si is introduced at 1420°C in vacuum, which allows capillary forces to pull the liquid into the preform. The Si has low viscosity and good wettability, which fills the preform rapidly. It reacts simultaneously with the carbon to form the SiC matrix. The microstructure consists of SiC granules built up on the preform and may incorporate the pre-existing SiC grains. Silicon has to be infiltrated continuously so that it can continue to diffuse through the fibers as the SiC reaction takes place. If too much free Silicon is introduced, it can react unfavorably with other materials or the oxidizing environment. Additionally, crystalline SiC is contained within the SiC matrix, meaning that the resulting matrix is multiphase. In general, MI materials tend to exhibit better interlaminar shear strength than CVI materials, but above 1300°C, residual silicon from the fabrication process may start to react with the fiber interphase and the fiber itself, reducing the life of the specimen [32].

2.3.4 Previous Research on SiC/SiC Ceramic Matrix Composites

Other authors have performed studies of CMC materials at high temperatures in air and in steam using similar methodology to the present work. The previous tests were conducted at 1200°C on composite specimens fabricated using chemical vapor infiltration (CVI). Table 2 shows a summary of mechanical properties of the CMCs investigated prior to this work.

Christensen [33] studied the mechanical behavior of a composite reinforced with Hi-Nicalon™ fibers woven in an eight-harness satin weave (8HSW). The material was processed by chemical vapor infiltration of SiC into the woven fiber preforms. Before the infiltration, the preforms were coated with boron nitride (BN) fiber coating to decrease the bond strength between the fibers and the matrix. The composite consisted of eight plies of woven fabric in a 0°/90° layup, with a finished fiber volume of approximately 34% and a porosity of ~9.5%.

Tensile stress-strain behavior and tensile properties were evaluated in tensile tests performed at 1200ºC. Christensen reported the following material properties at 1200°C: ultimate tensile strength (UTS) of 217 MPa, elastic modulus of 240 GPa, failure strain of 0.25%, and proportional limit of 110 MPa (~51% UTS). Tension-tension fatigue tests were conducted at 1200°C at frequencies of 0.1, 1.0, and 10 Hz. Stress levels ranged from 80 to 120 MPa in air and from 60 to 110 MPa in steam. Run-out was defined as 2 x 10^5 cycles for 1.0 Hz and 10 Hz, and 10^5 cycles for 0.1 Hz. The fatigue limits observed at 1.0 Hz were 100 MPa (46% UTS) in air and 80 MPa (37% UTS) in steam. All specimens tested in air retained 100% of their tensile strength and only one specimen tested in steam showed a loss in strength. Christensen reported 88% stiffness retention in all run-out specimens. Christensen concluded that the damage and failure of the composite in both air and steam environments developed through the growth of oxidation-assisted matrix cracks. In the air environment, at loading frequencies of 0.1 and 1.0 Hz this mechanism operated at higher stress conditions (>110 MPa), whereas at 10 Hz this mechanism was triggered at lower stresses (>80 MPa). Damage development and failure were accelerated in the presence of steam.

Delapasse [34] also studied tension-tension fatigue behavior of a composite reinforced with Hi-Nicalon™ fibers woven in an eight-harness satin weave and processed by CVI. The material had an oxidation-inhibiting matrix consisting of alternating layers of silicon carbide and boron carbide. Laminated fiber preforms were produced from eight plies of woven fabric in a 0°/90° layup symmetric about mid-plane with warp and fill plies alternated. Before the infiltration, the preforms were coated with a pyrolytic carbon coating (~0.40 μm thick) with boron carbide overlay (~1.0 μm thick) to decrease bonding between the fibers and the matrix. The composite had a finished fiber volume of approximately 34.8% and a density of ~2.56

g/cm^3. Delapasse reported the following mechanical properties at 1200°C: UTS of 307 MPa, elastic modulus of 208 GPa, failure strain of 0.69%, and proportional limit of 116 MPa (~38% UTS). Delapasse focused on tension-tension fatigue performance of the Hi-Nicalon™/SiC-B_4C ceramic composite at 1200°C in air and in steam. Delapasse reported that presence of steam had little influence on the fatigue performance at 1.0 Hz, but noticeably degraded fatigue lifetimes at 0.1 Hz for fatigue stresses ≥ 120 MPa. In the Hi-Nicalon™/SiC-B_4C composite, the oxidation embrittlement of the fibers is limited by the multilayered self-healing matrix, which reacts with oxygen and forms fluid oxide phases that seal the matrix cracks as soon as they are formed. As a result, the oxygen is trapped in the glassy phases and is inhibited from attacking the fibers. Thus, Delapasse proposed that the fatigue performance of the Hi-Nicalon™/SiC-B_4C composite was controlled by the creep resistance of the fibers.

Lee [35] also studied the Hi-Nicalon^{TM}/SiC-B_4C composite previously investigated by Delapasse. Whereas Delapasse investigated the mechanical performance of this composite at 1200°C, Lee focused on fatigue performance at 1300°C. He focused on fatigue behavior at 1.0 Hz only. Lee reported the following mechanical properties at 1300°C: UTS of 311 MPa, elastic modulus of 180 GPa, failure strain of 0.53%, and proportional limit of 117 MPa (~38 %UTS). Apparently, a temperature increase from 1200°C to 1300°C had little effect on tensile properties and proportional limit of the Hi-Nicalon^{TM} /SiC-B_4C composite. Lee conducted tension-tension fatigue tests in air and in steam at 1300°C at 1.0 Hz. Fatigue stress levels ranged from 70 to 160 MPa. Lee reported that the presence of steam had minimal effect on fatigue performance at 1300°C; the cyclic lives obtained in steam were close to those obtained in air. Lee concluded that at 1300°C in air and in steam, the damage and failure of the composite were primarily due to the creep of fibers. In air, the oxidation embrittlement of the Hi-Nicalon^{TM} fibers was successfully

limited by the multilayered self-healing matrix, which reacts with oxygen and forms fluid oxide phases that seal the matrix cracks as soon as they are formed. Lee proposed that the fiber degradation was most likely caused by an intrinsic creep-controlled flaw growth mechanism and that the fatigue performance of the Hi-Nicalon^{TM} /SiC-B_4C composite at 1300°C in air and in steam was controlled by the creep resistance of the fibers.

Table 2: Summary of mechanical properties of CMC materials tested under similar conditions

	Christensen	**Delapasse**	**Lee**
Material	Hi-Nicalon^{TM}/BN/CVI-SiC	Hi-Nicalon^{TM} /SiC-B_4C	Hi-Nicalon^{TM} /SiC-B_4C
Test Temperature	1200°C	1200°C	1300°C
Thermal expansion coefficient, 1/°C	6.06E-06	4.82E-06	4.74E-06
Avg UTS	217 MPa	306.8 MPa	311 MPa
Avg Elastic Modulus	246.5 GPa	206.3 GPa	180 GPa
Strain at Failure	0.25%	0.69%	0.57%
Proportional Limit	110 MPa	116.3 MPa	117 MPa
Fatigue Limit, Air, 1.0 Hz	100 MPa	100 MPa	70 MPa
Fatigue Limit, Steam, 1.0 Hz	80 MPa	100 MPa	100 MPa

III. Material and Test Specimen

3.1 Material Specifications

The material system studied in this thesis work was an advanced melt-infiltrated (MI) silicon carbide/silicon carbide (SiC/SiC) ceramic matrix composite (CMC) fabricated by Rolls-Royce Corporation. The composite is reinforced with Hi-Nicalon™ fibers woven in a five-harness satin weave (5HSW), illustrated in Figure 9. This particular weave allows the fabric to be more flexible during forming [36].

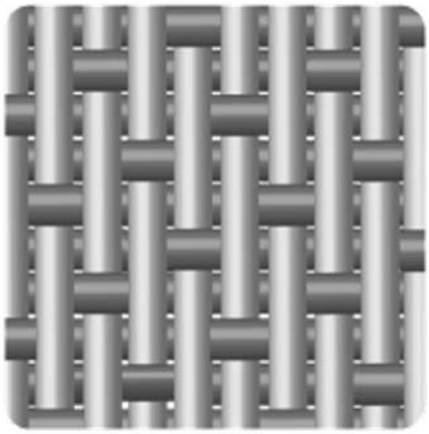

Figure 9: 5-harness satin weave (5HSW)

The material utilizes Hi-Nicalon™ fibers as in the previous studies, which are known for their excellent tensile strength and temperature resistance [37]. The fibers have exceptionally low oxygen content and consist primarily of β-SiC with trace amounts of free carbon and SiO_2. Laminated fiber preforms were produced from 10 plies of woven fiber fabric in a 0/90 layup symmetric about mid-plane with warp and fill plies alternated. The preforms were coated with BN via chemical vapor infiltration (CVI) to decrease bonding between fibers and matrix. Then a CVI-SiC coating was applied to rigidize the preforms and to protect the fibers, followed by slurry infiltration of SiC particulates and infiltration of molten Si to fill in the remaining porosity.

The composite had a finished fiber volume of ~5.67%, density of ~2.63 g/cm^3, open porosity of ~0.77 vol% and closed porosity of ~6.63 vol% [38]. The overall microstructure of the CMC is presented in Figure 10.

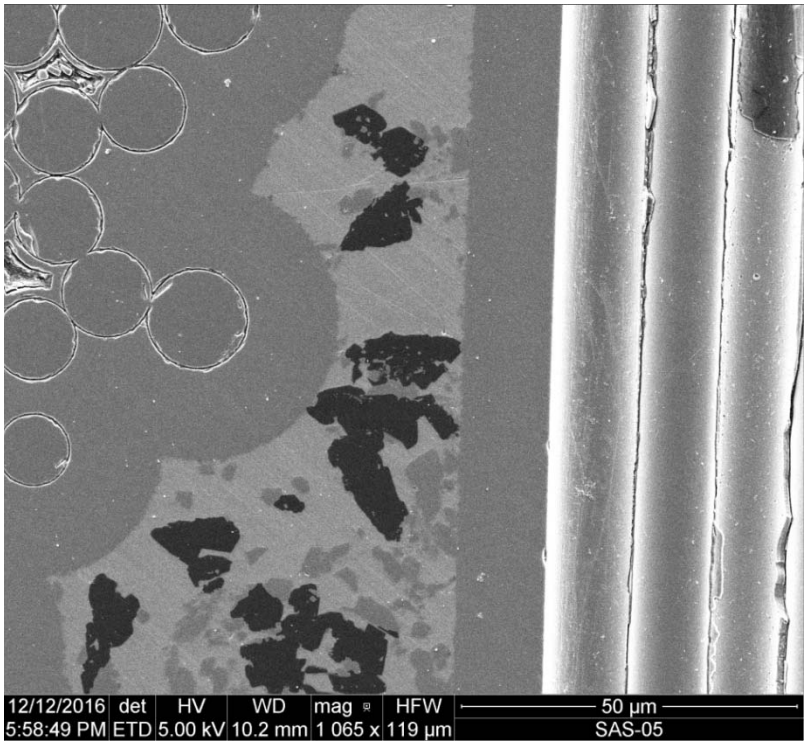

Figure 10: As-processed microstructure of Hi-Nicalon™/BN/SMI-SiC composite.

3.2 Test Specimen

Dogbone-shaped specimens were machined from panels of the CMC using diamond grinding to specifications in Figure 11. The width and thickness measured in the gauge sections are summarized in Table 3. Note that for each specimen, the width and thickness were measured in three different locations within the gauge section to obtain an average width and thickness. Notably, all variations between these measurements were within $\pm$ .015 mm.

Table 3: Specimen dimensions

Specimen Number	Gage Width (mm)	Gage Thickness (mm)	Gage Cross Section (m^2)
16-031	8.01	2.72	2.18E-05
16-032	8.00	2.72	2.18E-05
16-033	8.01	2.76	2.21E-05
16-044	8.02	2.71	2.17E-05
16-045	8.03	2.72	2.18E-05
16-046	8.03	2.77	2.22E-05
16-056	8.00	2.69	2.15E-05
16-057	8.00	2.70	2.16E-05
16-058	8.02	2.72	2.18E-05
16-059	7.99	2.75	2.20E-05

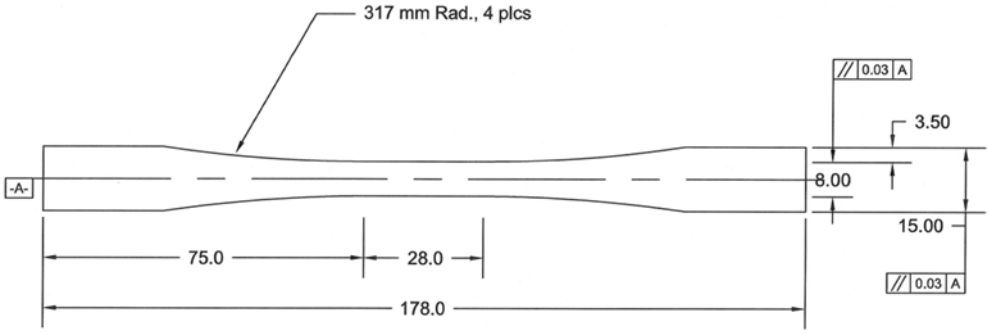

Figure 11: Specimen dimensions (mm)

Rectangular fiberglass tabs were bonded to the gripping sections of the dogbone-shaped specimens using M-bond 200 adhesive in order to protect the composite from being crushed in the grips of the testing machine. Nominal tab thickness was 0.8 mm. During the tabbing process, notable curvature was observed along the length of the specimens. To confirm this, the specimen was clamped into the top grip and a picture was taken to show if the bottom of the specimen was closer to one side of the open grip than the other. The specimen was rotated about the long axis and the process repeated. A curved specimen would deflect equal amounts in both orientations as shown in Figure 12. All but one of the specimens exhibited such noticeable curvature. It is

recognized that when the tensile load is applied, a bent specimen will be subject to combined tension and bending rather than pure tension.

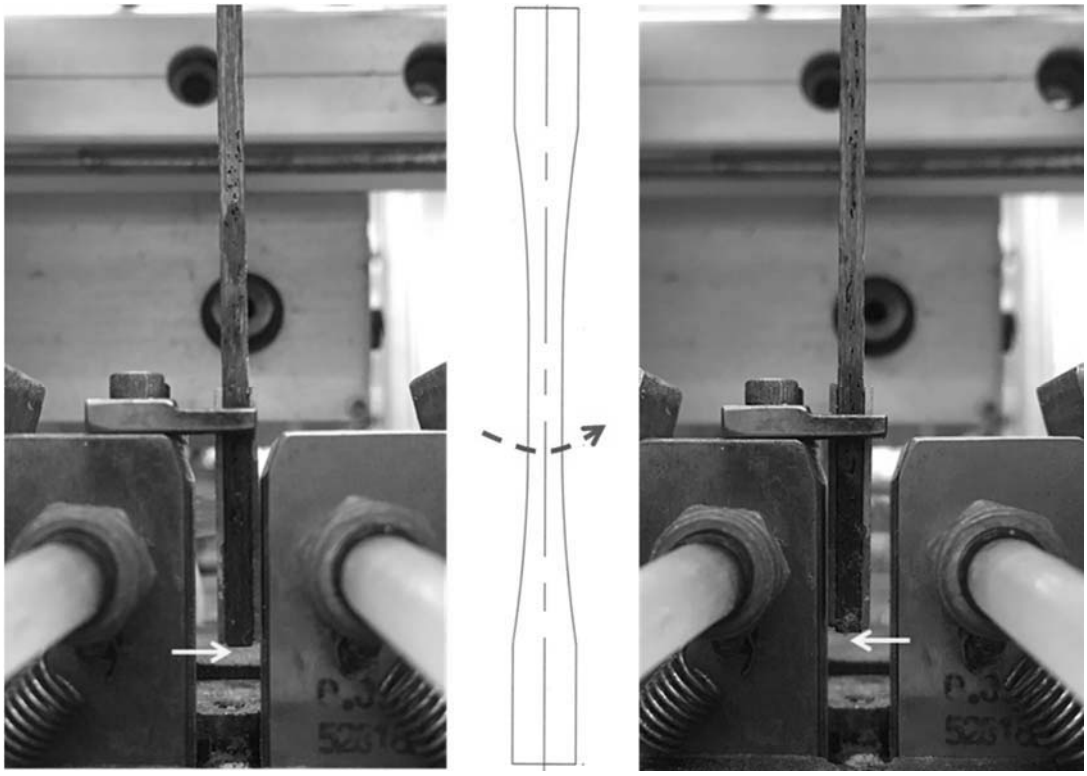

Figure 12: When clamped at the top, curvature of the specimen caused the free end to deflect. Rotating the specimen showed equal deflection in the opposite direction.

While the density of the material is comparable to the composites studied by Christensen, Delapasse and Lee, multiple large voids were present and clearly visible to the naked eye (see Figure 13). It has been demonstrated that an oxidizing environment enters the CMC material through fatigue-induced matrix cracks and attacks the oxidation-prone fibers [39]. Likewise, such large openings will allow the oxidizing environment to penetrate much further into the material and accelerate composite failure, since it is recognized that the strength of the fiber/matrix interface is reduced in high-temperature oxidizing environments, increasing the interface wear rate and reducing the life of the material [40].

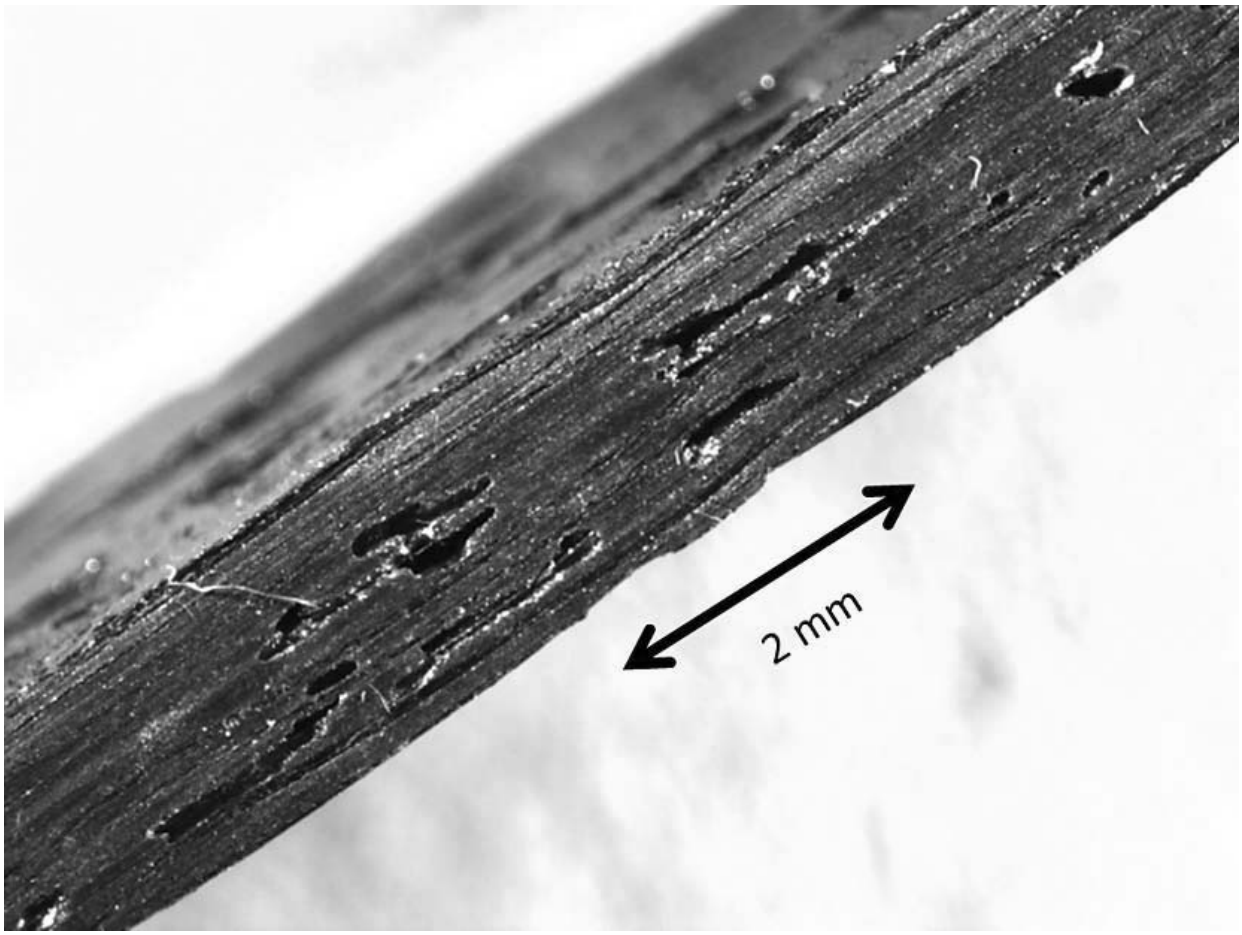

Figure 13: Optical micrograph of as-machined test specimen. Voids ranging from 0.5 mm to 2 mm in size are clearly visible.

IV. Experimental Setup and Procedure

4.1 Test Equipment

All tests were performed on the 5 kip MTS 810 test frame shown in Figure 14. A FlexTest 40 digital controller was used in all tests for input signal generation and data acquisition. The specimens were heated using an AMTECO Hot Rail two-zone furnace. Temperature was controlled using MTS 409.83B controllers. Wedge grips were water-cooled at approximately 15°C using a Naslab model HX-75 chiller. The grip surfaces were coated with a Surfalloy texturing to prevent slip, and were cleaned between runs to remove any material that remained caught on the surface. Grip pressure was set at 11 MPa. Strain measurement was accomplished with an MTS 632.15 high-temperature uniaxial extensometer of 12.5 mm gage length. The extensometer was cooled with a stream of low-pressure laboratory air, and was held in place against the test specimen with a low-contact-force spring.

An alumina susceptor, shown in Figure 15, was used in order to create a nearly 100% steam environment around the gage section of the test specimen and to protect the furnace elements from the steam environment. Steam was generated using an AMTECO steam generator and deionized water and was delivered to the susceptor through an alumina feeding tube to ensure the test chamber was fully saturated. Silica wool was used on the exterior of the furnace to provide additional insulation.

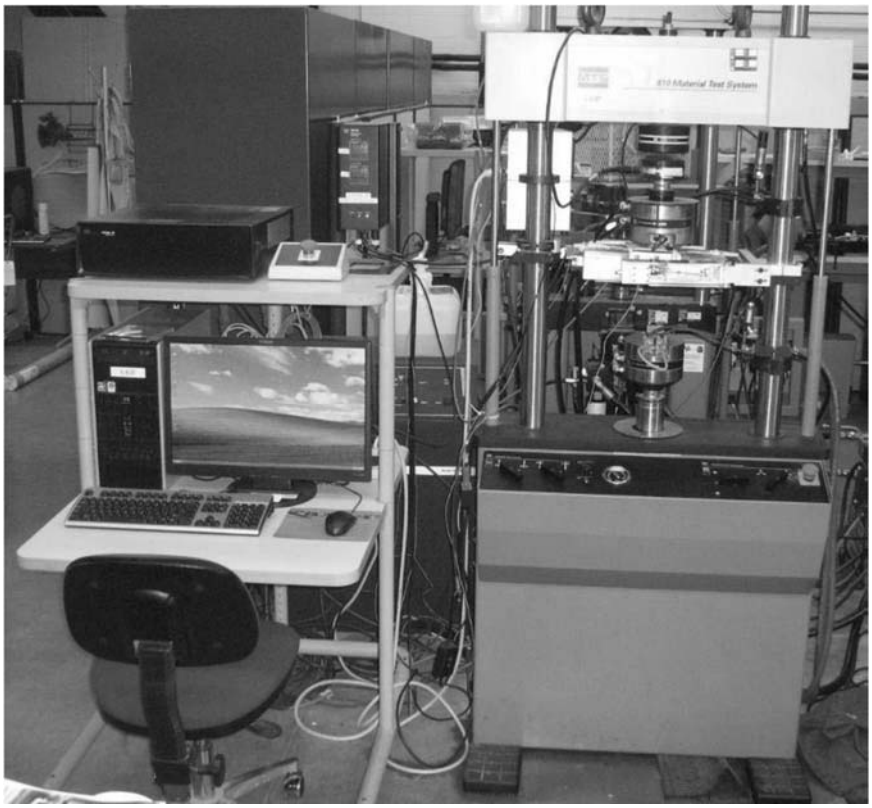

Figure 14: 5 kip MTS load frame and Flex Test 40 digital controller

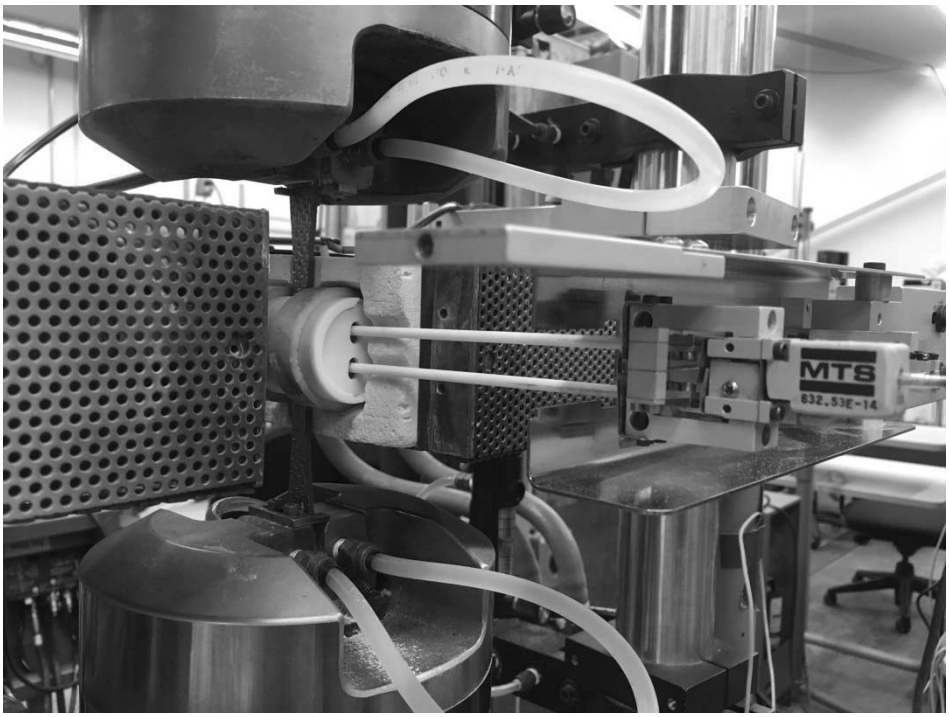

Figure 15: Furnace, susceptor and extensometer in preparation for testing.

4.2 Temperature Calibration

The alumina susceptor was used in all tests performed in this effort. When testing in air, the susceptor provides additional thermal mass in the test chamber and radiates heat uniformly towards the specimen, thus stabilizing the specimen temperature. For testing at elevated temperature, a specimen was instrumented with two type R thermocouples to calibrate the furnace on a periodic basis (see Figure 16). The furnace controllers (using non-contacting S-type thermocouples exposed to the ambient environment near the test specimen) were adjusted to determine the settings needed to achieve the desired temperature of the test specimen. The determined settings were then used in actual tests.

Figure 16: Calibration thermocouples. The metal wires caused blackening on the alumina plates used to hold the bead against the specimen

To find the desired control settings, the temperature of the furnace was first raised to 1000°C, then slowly raised until the thermocouples on the calibration specimen read 1200° $\pm$ 5°C. An Omega HH501BR type-R thermocouple meter was used to measure the temperature of the thermocouples. During temperature calibration the testing machine was in load control with

load held at zero to allow for thermal expansion of the specimen. Calibration was repeated twice for both environments to ensure steady-state temperature was maintained around 1200°C without overheating the specimen. Calibration was repeated if new furnace elements were installed. Set points are listed in Table 4.

Table 4: Temperature controller set points determined for testing at 1200°C

Test Environment	Set Point, Left	Set Point, Right
Air	1265	1250
Steam	1290	1275

4.3 Microstructural Characterization

The virgin material as well as the tested specimens were prepared before examination with the optical microscope and scanning electron microscope (SEM). A sample of virgin material was sectioned and mounted in epoxy, yielding three different views of the microstructure. The pucks were polished in a Beuhler autopolisher using a grit progression from 220-grit to 1-μm diamond suspension, outlined in Table 5. Water was used as lubrication. Once polished, the pucks were ultrasonically cleaned in alcohol for 30 s, dried, and sputter coated with approximately 15 nm of carbon to provide a conductive path to the microscope stage.

Table 5: Polishing procedure for virgin material specimen [41]

Step	Surface	Grit Size	Time (Estimated)	Spin Direction	Base Speed	Head Speed	Pressure
1	Piano DGD	220	1:00 min increments, until Planar grinding step is achieved.	Complimentary	300 rpm	50 rpm	10 lbs
2	Piano DGD	500	5:00 min	Complementary	150 rpm	50 rpm	8 lbs
3	Piano DGD	1200	5:00 min	Complimentary	150 rpm	50 rpm	8 lbs
4	Piano DGD	2000	4:00 min	Complimentary	150 rpm	50 rpm	8 lbs
5	Piano DGD	4000	3:00 min	Complimentary	150 rpm	50 rpm	8 lbs
6	VerduTex	1 μm	3:00 min	Contra-rotation	150 rpm	50 rpm	8 lbs

Optical micrographs of the tested specimens (both the top and bottom sections) were taken with a Zeiss Stereo V12 equipped with a Zeiss AxioCam HRc digital camera. Then, the fracture surface was removed from the bottom portion of the failed specimen using a dry 20-LC diamond saw to cut approximately 2 cm away from the fracture surface. The saw was stopped before completing the cut, leaving a small ligament of material to hold the fracture end in place to prevent it falling into the saw. Using tweezers, the fracture end was broken off. Taking care to not touch the fracture surface, carbon tape was used to blot dust off of the base of the cut. The specimen was then mounted to a microscope sample stage using carbon tape. Images were taken of the fracture surfaces on a FEI Quanta 200 SEM, and energy dispersive spectroscopy (EDS) analysis was performed with a Quanta 650 machine. Only the fracture surfaces of the bottom portions of the test specimens were examined with an SEM. When a specimen fails the testing system is immediately shut off and the bottom portion of the failed specimen is removed from the furnace. Thus the fracture surface of that portion of the failed specimen is exposed to significant temperatures and prolonged oxidation for a few minutes at most. The top portion of the specimen remains in the oxidizing environment for a longer time and are not examined with the SEM.

4.4 Experimental Procedure

In all tests, a specimen was heated to test temperature at 1°C/min, and held at temperature for 30 minutes prior to testing. The same procedure was used for testing in air and in steam.

4.4.1 Monotonic Tension Test

Due to the limited number of test specimens, only one was tested in tension to failure at 1200°C in laboratory air. After reaching steady-state temperature, the tensile test was performed

in displacement control at a constant rate of 0.05 mm/s. Strain, force, actuator displacement, and furnace temperature were all recorded continuously during the test.

4.4.2 Fatigue Testing

Eight specimens were tested in tension-tension fatigue at 1200°C. Four specimens were tested in air and four were tested in steam. Tension-tension fatigue tests were performed in load control with a frequency of 1.0 Hz using a sinusoidal waveform and a ratio of minimum to maximum stress R = 0.05. Fatigue run-out was set at 2 x 10^5 cycles. Strain, force, displacement, and furnace temperature were recorded during each phase of the test. Data were collected in separate files during the different phases of each test. During warm-up, the temperature and strain were sampled every 2 seconds to provide a record of thermal expansion. During the "Ramp_to_min" phase, data (i.e. strain, force, displacement, and furnace temperature) was collected at a sample rate of 100Hz. Then, "Peak_Valley" data (strain, force, displacement, and furnace temperature at the peak and valley of a cycle) were recorded for every cycle during the fatigue portion of the test. The "Cyclic" phase collected strain, force, displacement, and furnace temperature at a sample rate of 50 Hz for certain specified cycles in order to assess the evolution of the hysteresis behavior, strain accumulation with cycles and modulus changes with cycles. These data were collected at:

i) cycles 1 to 10,

ii) every 10^{th} cycle between cycles 20 and 100,

iii) every 100^{th} cycle between cycles 100 and 1000,

iv) every 1000_{th} cycle between cycles 1000 and 10000, and

v) every 10000_{th} cycle between cycles 10000 and run-out.

If the specimen achieved fatigue run-out, it was unloaded to zero load, then tested in tension to failure at 1200°C to determine the retained tensile properties. Strain, displacement, force and temperature data was recorded with a sample rate of 100Hz in the "Tensile" file for the test. The screen shot in Figure 17 shows the MTS procedure used for fatigue testing.

Great care was taken to ensure that during a fatigue test, the specimen would experience the correct temperature throughout the test. In addition, it was imperative that the specimen did not go into compression. If the temperature dropped 5 degrees or more due to the loss of an element, the software would turn off the furnace, zero the load on the actuator, and stop data collection. The procedure was reset and restarted after the furnace element was replaced and the set points re-calibrated.

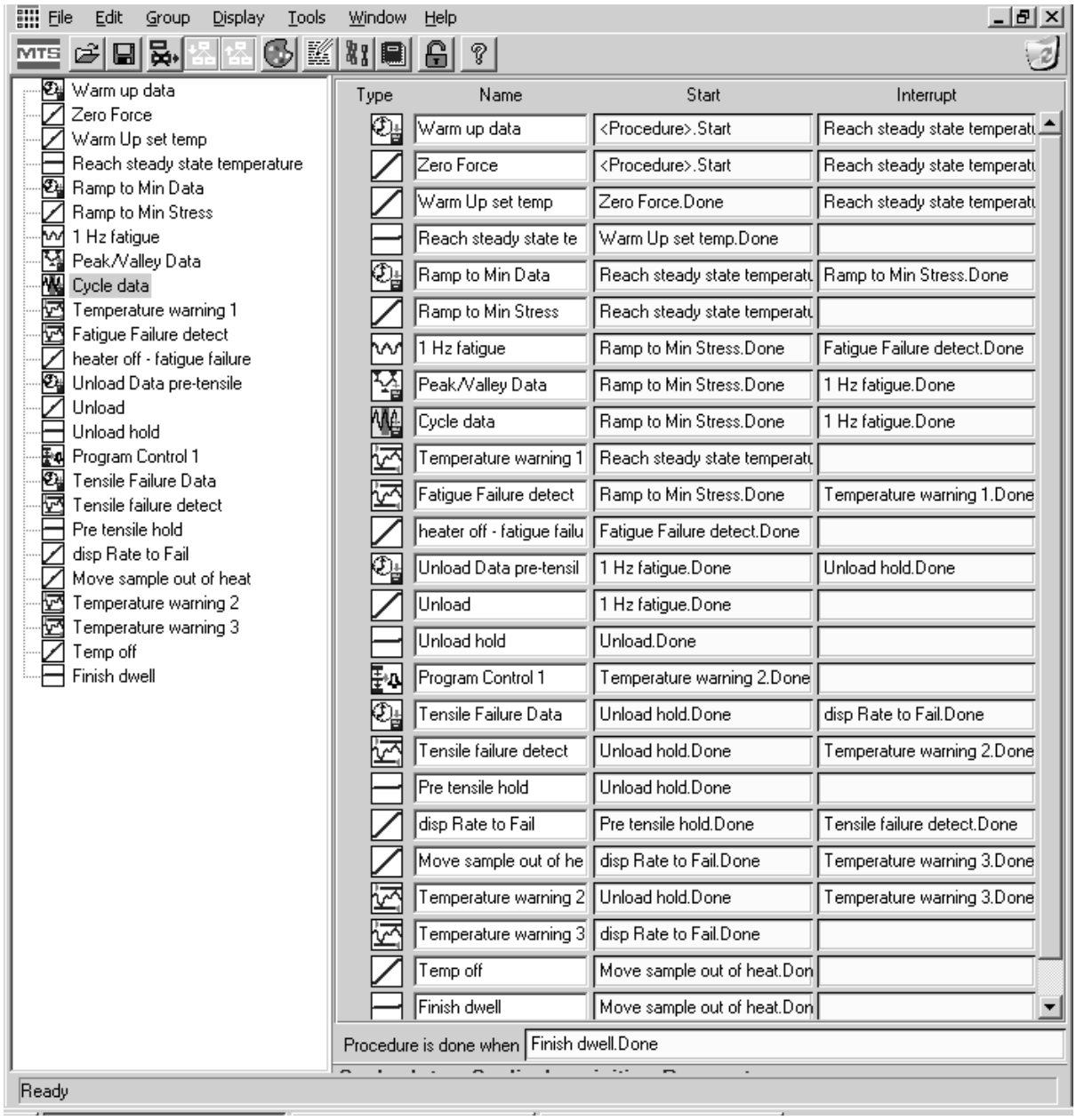

Figure 17: Fatigue test procedure

V. Results and Discussion

5.1 Chapter Overview

Results of all tests are discussed in this chapter. Section 5.2 discusses thermal expansion and presents coefficients of thermal expansion determined in each test. Section 5.3 presents results of the tension test to failure performed in order to determine tensile properties. Section 5.4 presents the results of the tension-tension fatigue tests performed in laboratory air and in steam. Section 5.5 discusses the effects of prior fatigue on tensile properties. Analysis of composite microstructure is presented in Section 5.6. All tests performed in this work are summarized in Table 6. All tests were performed at 1200°C. Fatigue tests were conducted with a ratio of minimum to maximum stress of R = 0.05. Fatigue run-out was set to 2 x 10^5 cycles.

Table 6: Summary of Hi-Nicalon™/BN/SMI-SiC ceramic matrix composite test results at 1200°C

Specimen	Test Environment	Maximum Stress (MPa)	Elastic Modulus (GPa)[b]	Cycles to Failure (N)	Time to Failure (h)	Failure Strain (%)
			Tensile Test			
16-059	Air	239	217	-	-	0.410
			Tension-Tension Fatigue Test			
16-031	Air	120	226.8	200000[a]	55.6	0.392
16-044	Air	130	202.6	4506	1.30	0.110
16-045	Air	140	228.5	2200	0.60	0.067
16-057	Air	160	145.4	1220	0.30	0.015
16-033	Steam	100	252.3	200000[a]	55.6	0.402
16-046	Steam	110	110.7	200000[a]	55.6	0.403
16-032	Steam	120	234.3	5311	1.50	0.113
16-058	Steam	130	229.6	3201	0.90	0.132

a. Run-out. Failure of specimen did not occur when the test was terminated.
b. For fatigue specimens, modulus is determined from the first cycle.

5.2 Thermal Expansion

The coefficient of thermal expansion (CTE) was determined from strain and temperature data obtained during the warm-up portion of each test. The CTE was determined as

$$\alpha = \frac{\varepsilon}{\Delta T}$$

Where ε is the thermal strain measured upon completion of warm-up, and ΔT is the difference between room temperature (23°C) and the test temperature (1200°C). The thermal strain varied from 0.41% to 0.54%, with an average thermal strain of 0.49%. The average CTE was calculated as 4.19 x 10^{-6} 1/°C with a standard deviation of 0.39 x 10^{-6} 1/°C. Note that Delapasse [34] and Lee [35] reported a CTE of 4.74 x 10^{-6} 1/°C for the Hi-Nicalon™/SiC-B_4C composite, while Christensen reported a CTE of 6.06 x 10^{-6} 1/°C for the Hi-Nicalon™/BN/CVI-SiC composite. Thermal strains measured in this work are summarized in Table 7 together with the calculated coefficients of linear thermal expansion.

Table 7: Thermal strain and coefficient of linear thermal expansion for Hi-Nicalon™/BN/SMI-SiC

Specimen	Thermal Strain (%)	Coefficient of Linear Thermal Expansion (10^{-6} / °C)
16-031	0.503	4.39
16-057	0.537	4.57
16-045	0.496	4.24
16-032	0.480	4.09
16-033	0.408	3.50
16-058	0.539	4.58
16-046	0.444	3.78
16-044	0.520	4.40
16-059	0.554	4.70
Average	0.498	4.25
Std. Dev.	0.048	0.40

5.3 Monotonic Tension

Due to a very limited number of specimens available for this work, only one specimen was tested in tension to failure to determine the tensile properties. The tensile stress-strain curve is shown in Figure 18. At 1200°C the ultimate tensile strength (UTS) was 239 MPa. The elastic modulus was 217 GPa, and the failure strain was 0.41%. The proportional limit was determined as the stress at which the stress-strain curve departs from linearity, or 135 MPa (56% of UTS). Tensile properties are compared in Table 8 to the properties of Hi-Nicalon™/BN/CVI-SiC and Hi-Nicalon™/SiC-B_4C composites.

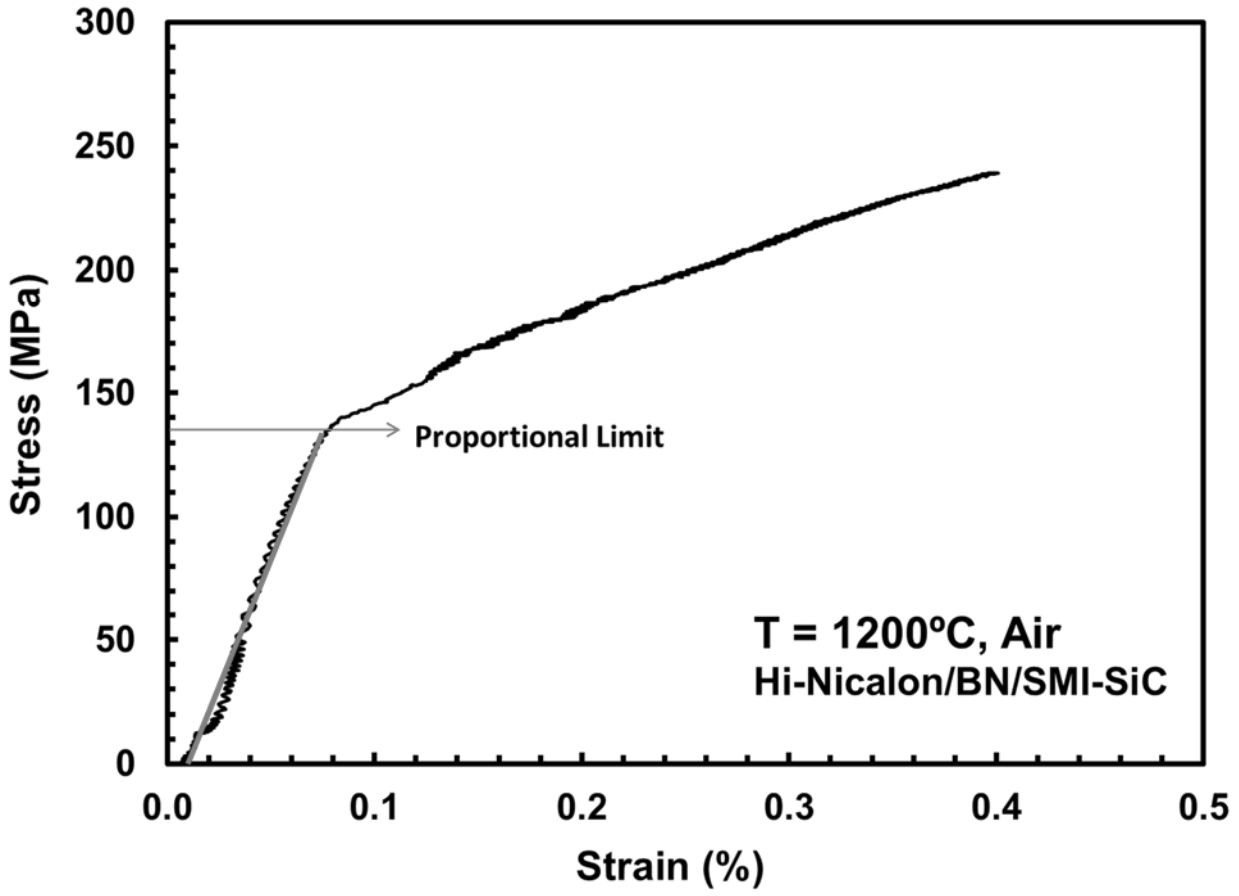

Figure 18: Tensile stress-strain curve obtained for Hi-Nicalon™/BN/SMI-SiC at 1200°C in laboratory air.

Table 8: Tensile properties obtained for Hi-Nicalon™/BN/SMI-SiC, Hi-Nicalon™/BN/CVI-SiC and Hi-Nicalon™/BN/SiC-B_4C composites at 1200°C in laboratory air at a constant displacement rate of 0.05mm/s.

Material	Elastic Modulus (GPa)	Proportional Limit (MPa)	UTS (MPa)	Failure Strain (%)
Hi-Nicalon™/BN/SMI-SiC	217.1	135	239	0.412
Hi-Nicalon™/BN/CVI-SiC[a]	246.5	110	217	0.250
Hi-Nicalon™/SiC-B_4C[b]	206.3	116	307	0.686

a. Data from Christensen [31]
b. Data from Delapasse [32]

Tensile stress-strain curves obtained for the Hi-Nicalon™/BN/SMI-SiC composite at 1200°C are compared to those obtained for the Hi-Nicalon™/BN/CVI-SiC and Hi-Nicalon™/SiC-B_4C composites in Figure 19. Note that the stress-strain curves obtained for all three composites at 1200°C exhibit a nearly bilinear behavior. The stress-strain behavior is linear up to the proportional limit, where nonlinear behavior caused by matrix cracking occurs. Afterwards, the stress-strain curves continue with a decreased slope. The UTS value produced for the Hi-Nicalon™/BN/SMI-SiC composite is similar to that obtained for the Hi-Nicalon™/BN/CVI-SiC, but considerably lower than the UTS produced for the Hi-Nicalon™/SiC-B_4C.

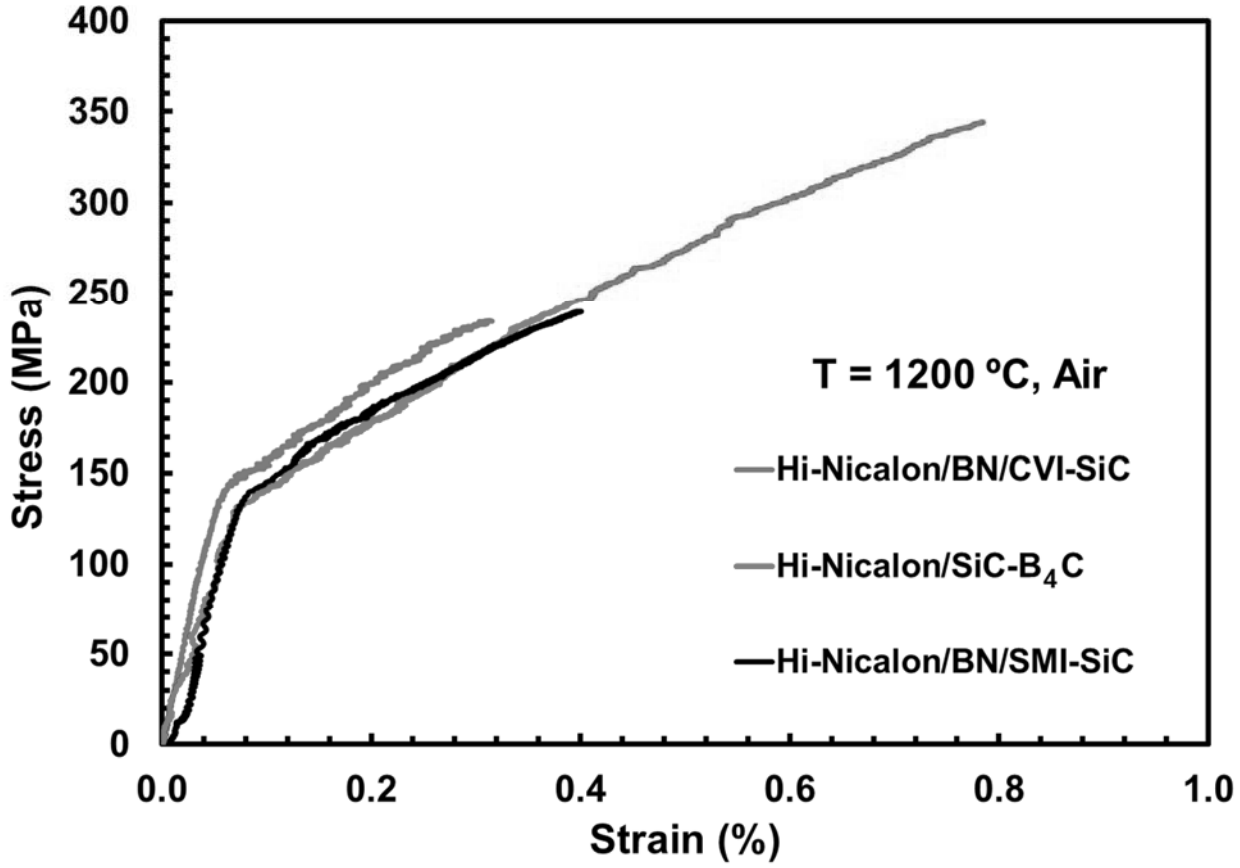

Figure 19: Tensile stress-strain test result of Hi-Nicalon^{TM}/BN/SMI-SiC compared to CVI materials studied by Christensen and Delepasse [31,32]

To give an idea of the possible variance in tensile properties of the SMI-SiC/SiC composites, we look to other studies that had access to more test specimens. Murthy et al. [42] performed a study of twenty SMI-SiC/SiC tensile specimens at 1200°C in air, and found a mean elastic modulus of 180.6 GPa with a standard deviation of 15.8 GPa, and a mean proportional limit of 166.8 MPa with a standard deviation of 26.9 MPa. Since only one test specimen was available for tensile testing in the present study, we are unable to make any statistical claims of our own. Yet, the data from Murthy gives an idea of how much variance there could be in the tensile strength of the Hi-Nicalon^{TM}/BN/SMI-SiC composite material.

5.4 Tension-Tension Fatigue

Tension-tension fatigue tests were conducted at a frequency of 1.0 Hz with a sinusoidal wave form at 1200°C in air and in steam. The ratio of minimum to maximum stress was R = 0.05. The maximum stress levels ranged from 120 to 160 MPa in air, and from 100 to 140 MPa in steam. Fatigue run-out was defined as $2x10^5$ cycles. This run-out condition approximates the number of loading cycles expected in aerospace applications at 1200°C [43]. Results of tension-tension fatigue tests are summarized in Table 9. Results of the tension-tension fatigue tests are also shown in Figure 20 as maximum stress vs. cycles to failure (S-N) curves.

Table 9: Summary of fatigue results obtained for the Hi-Nicalon™/BN/SMI-SiC composite at 1200 ^{0}C in laboratory air and in steam.

Specimen	Test Environment	Maximum Stress (MPa)	Elastic Modulus (GPa)[b]	Cycles to Failure (N)	Time to Failure (h)	Failure Strain (%)
16-031	Laboratory Air	120	226.8	200000[a]	55.6	0.392
16-044	Laboratory Air	130	202.6	4506	1.30	0.110
16-045	Laboratory Air	140	228.5	2200	0.60	0.067
16-057	Laboratory Air	160	145.4	1220	0.30	0.015
16-033	Steam	100	252.3	200000[a]	55.6	0.402
16-046	Steam	110	110.7	200000[a]	55.6	0.403
16-032	Steam	120	234.3	5311	1.50	0.113
16-058	Steam	130	229.6	3201	0.90	0.132

a. Run-out, failure of specimen did not occur when the test was terminated.
b. For fatigue specimens, modulus is determined from the first cycle.

As expected, the results in Figure 20 show that fatigue life decreases with increasing maximum stress. However, the sharp decrease in cyclic life observed when the maximum stress exceeds fatigue run-out stress is surprising. At 1200°C in air, the fatigue run-out of $2x10^5$ cycles was achieved at 120 MPa. As the maximum stress is increased from 120 MPa to 130 MPa, the cyclic life is reduced by nearly two orders of magnitude. In contrast, further increasing the maximum stress from 130 MPa to 140 MPa and then to 160 MPa does not cause orders of

magnitude reductions in cyclic life. The microstructural investigation of the as-processed material (see Section 5.6.1) revealed the presence of numerous voids of considerable size. It is recognized that such voids or flaws serve as fracture origins. For example, during fatigue loading, the stress concentration at a sharp corner of these voids may be sufficient to produce a crack. A well-known relationship between the crack growth rate da/dN and stress intensity range ΔK [44] demonstrates that there often appears to be a threshold value ΔK_{th} of the stress intensity range below which fatigue crack growth does not ordinarily occur. Recall that ΔK depends on the remotely applied stress range and on the size of the flaw present in the material. Apparently the processing flaws present in the Hi-Nicalon™/BN/SMI-SiC composite are sufficiently large to trigger crack growth for maximum stress levels above 120 MPa, but not for maximum stress levels of 120 MPa and below. Once the ΔK_{th} of the stress intensity range exceeds the threshold value ΔK_{th}, cracks begin to grow, sharply reducing the fatigue life of the composite. The effect of processing on the composite microstructure and consequently on the composite mechanical response cannot be overstated. A better fatigue performance could be expected if it were possible to modify the composite processing to reduce the number and size of the flaws.

The presence of steam at 1200°C degrades the fatigue performance of the composite. However, the degradation is not dramatic. The presence of steam reduced the fatigue run-out stress by some 7%. At 1200°C, the fatigue run-out was achieved at 120 MPa in air and at 110 MPa in steam. Note that the results obtained in air and in steam are well-correlated by σ_{max}; the two S-N curves have nearly the same slope. It is noteworthy that in steam we also observe the sharp decrease in the cyclic life as maximum stress increases by ~10% from the fatigue run-out stress. These observations support a conclusion that the substantial population of the processing flaws is behind the reduced cyclic life at stress levels above the fatigue run-out stress.

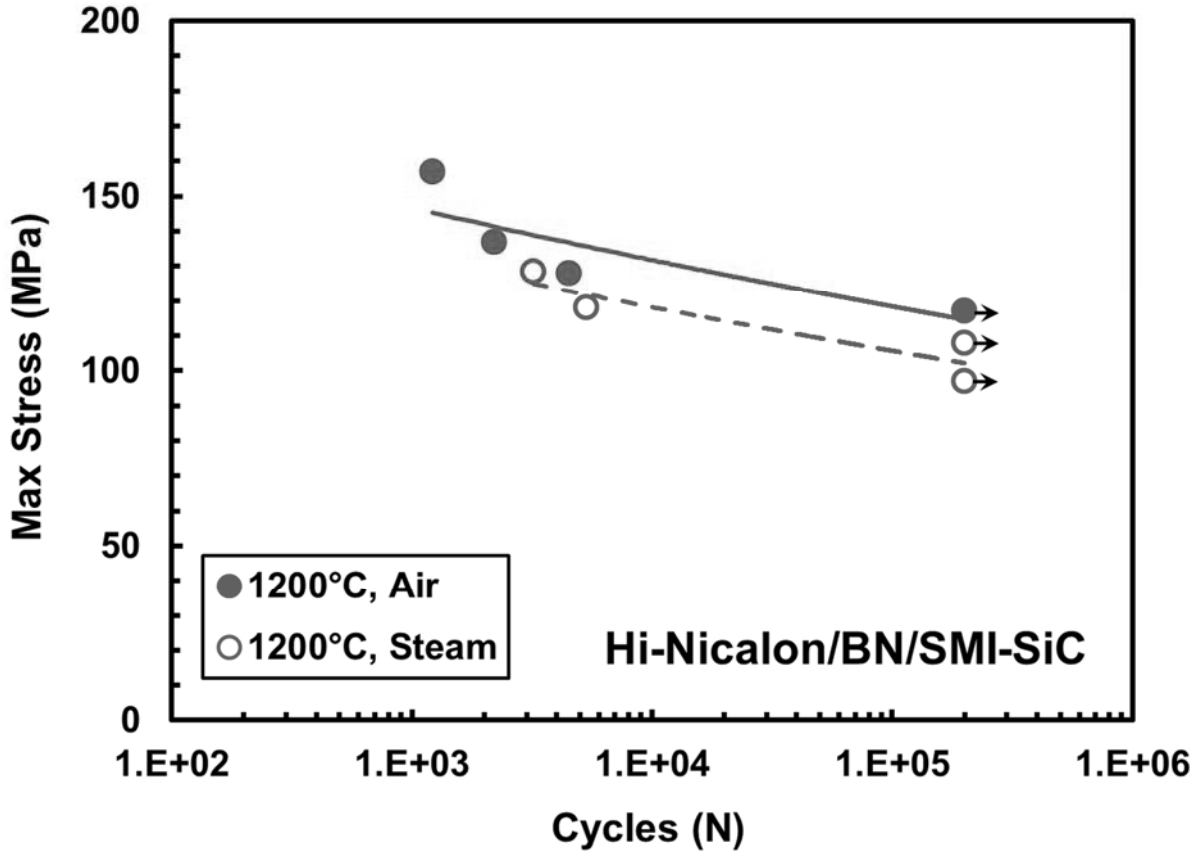

Figure 20: Stress vs. cycles to failure for dogbone specimens of Hi-Nicalon™/BN/SMI-SiC at 1200°C in air and in steam. The arrows indicate that the specimen survived up to $2x10^5$ cycles.

It is instructive to compare the tension-tension fatigue results obtained in this work for the Hi-Nicalon™/BN/SMI-SiC composite with those obtained for Hi-Nicalon™/BN/CVI-SiC [33] and Hi-Nicalon™/SiC-B_4C [34] composites. Results are summarized in Table 10. As evidenced in Figure 21, the Hi-Nicalon™/SiC-B_4C composite significantly outperforms the Nicalon™/BN/SMI-SiC and Hi-Nicalon™/BN/CVI-SiC composites in tension-tension fatigue at 1200°C in both air and steam. Furthermore, at 1200°C steam causes a considerable reduction in cyclic life for both the Hi-Nicalon™/BN/SMI-SiC and the Hi-Nicalon™/BN/CVI-SiC, while little affecting the fatigue performance of the Hi-Nicalon™/SiC-B_4C composite. The multilayered oxidation inhibited matrix of the Hi-Nicalon™/SiC-B_4C composite is likely

responsible for improved fatigue performance at 1200°C in air and in steam. The Hi-Nicalon™/BN/CVI-SiC composite studied by Christensen [33] did not have the benefit of the oxidation inhibited matrix. Hence the damage and failure of the Hi-Nicalon™/BN/CVI-SiC composite in both air and steam environments developed through the growth of oxidation-assisted matrix cracks. Damage development and failure were further accelerated in the presence of steam. If the Hi-Nicalon™/BN/SMI-SiC composite studied in this work contains oxidation-inhibiting compounds in the matrix, they do not greatly benefit fatigue performance. Fatigue life at 1200°C in air is rather poor and further degraded by the presence of steam. We believe that the presence of numerous processing flaws of substantial size is behind the Hi-Nicalon™/BN/SMI-SiC composite having shorter cyclic life than the Hi-Nicalon™/SiC-B_4C when tested at stresses above their respective fatigue limit stresses.

Table 10: Summary of fatigue life results in air and steam conducted at comparable maximum stress levels

Maximum Stress (MPa)	Cycles to Failure (N)		Change in life in steam (%)
	Air	**Steam**	
Hi-Nicalon™/BN/SMI-SiC			
120	200000	5311	-97%
130	4506	3201	-29%
Hi-Nicalon™/BN/CVI-SiC			
80	200000	200000	0.00%
100	200000	4741[a]	-98%
110	59641	5620	-91%
Hi-Nicalon™/SiC-B_4C			
100	200000	200000	0.00%
120	105999[a]	127221[a]	20%
130	95712	98462	2.9%
140	63458	36679	-42%

a. Average value if multiple tests at specified stress level

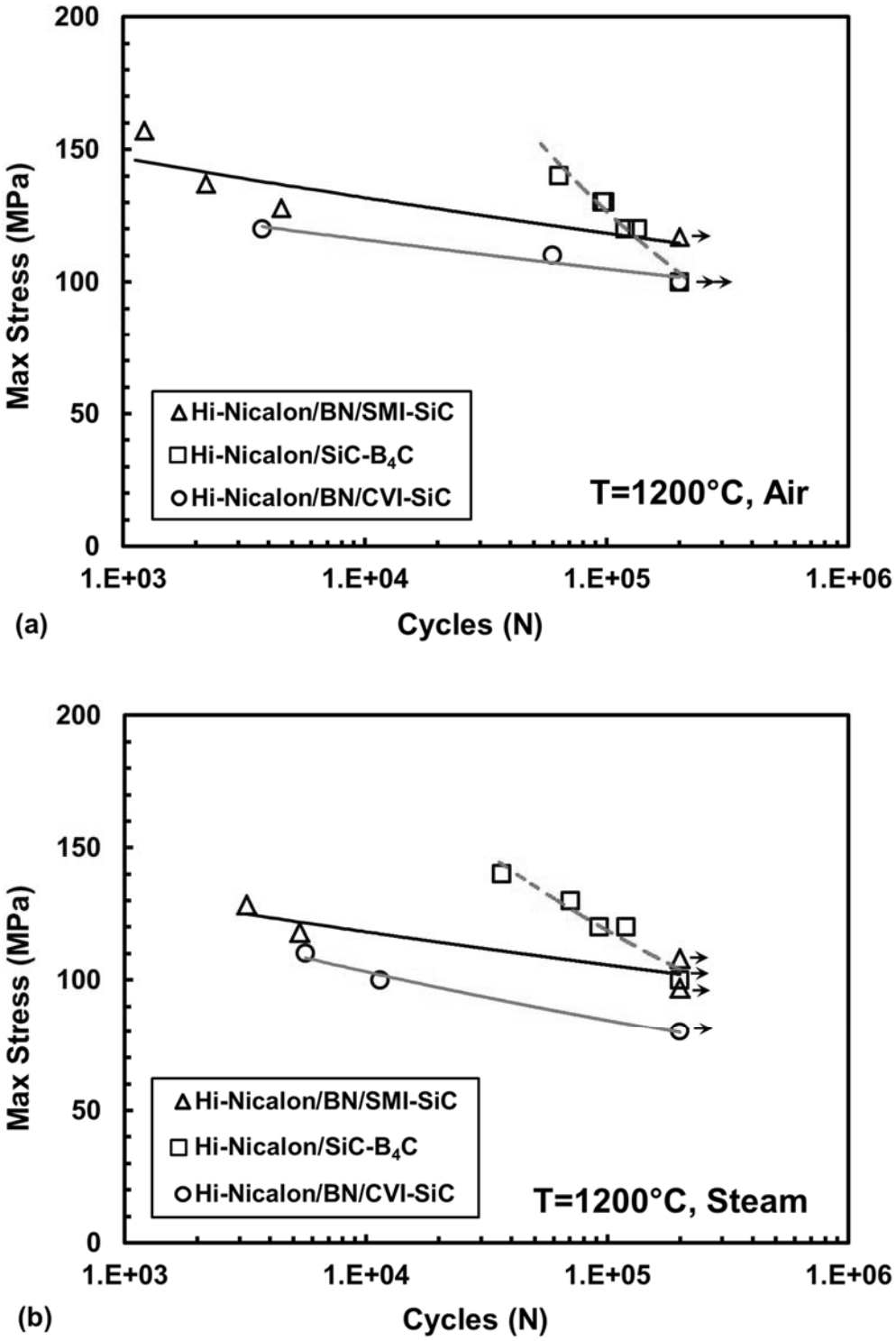

Figure 21: Fatigue stress vs. cycles to failure (S-N) curves obtained for Hi-Nicalon™/BN/SMI-SiC, Hi-Nicalon™/BN/CVI-SiC and Hi-Nicalon™/SiC-B_4C composites at 1200°C in (a) laboratory air and (b) steam. Data for Hi-Nicalon™/BN/CVI-SiC from Christensen [33]. Data for Hi-Nicalon™/SiC-B_4C is from Delapasse [34]. Arrow indicates that failure of specimen did not occur when the test was terminated.

The change in the composite modulus is also important in cyclic fatigue. The hysteresis modulus is determined from the maximum and minimum stress-strain data points during a load cycle, and reflects damage development during fatigue cycling [45]. The change in normalized modulus (i.e. hysteresis modulus normalized by the modulus obtained on the first cycle) at 1200°C in air and in steam is presented in Figures 22 and 23, respectively. It is noteworthy that little change in normalized modulus with cycles is observed in all tests performed in air. The cyclic softening of the specimens tested in steam suggests that once matrix cracking initiated, crack arrest occurred followed by more rapid crack growth and ultimately failure.

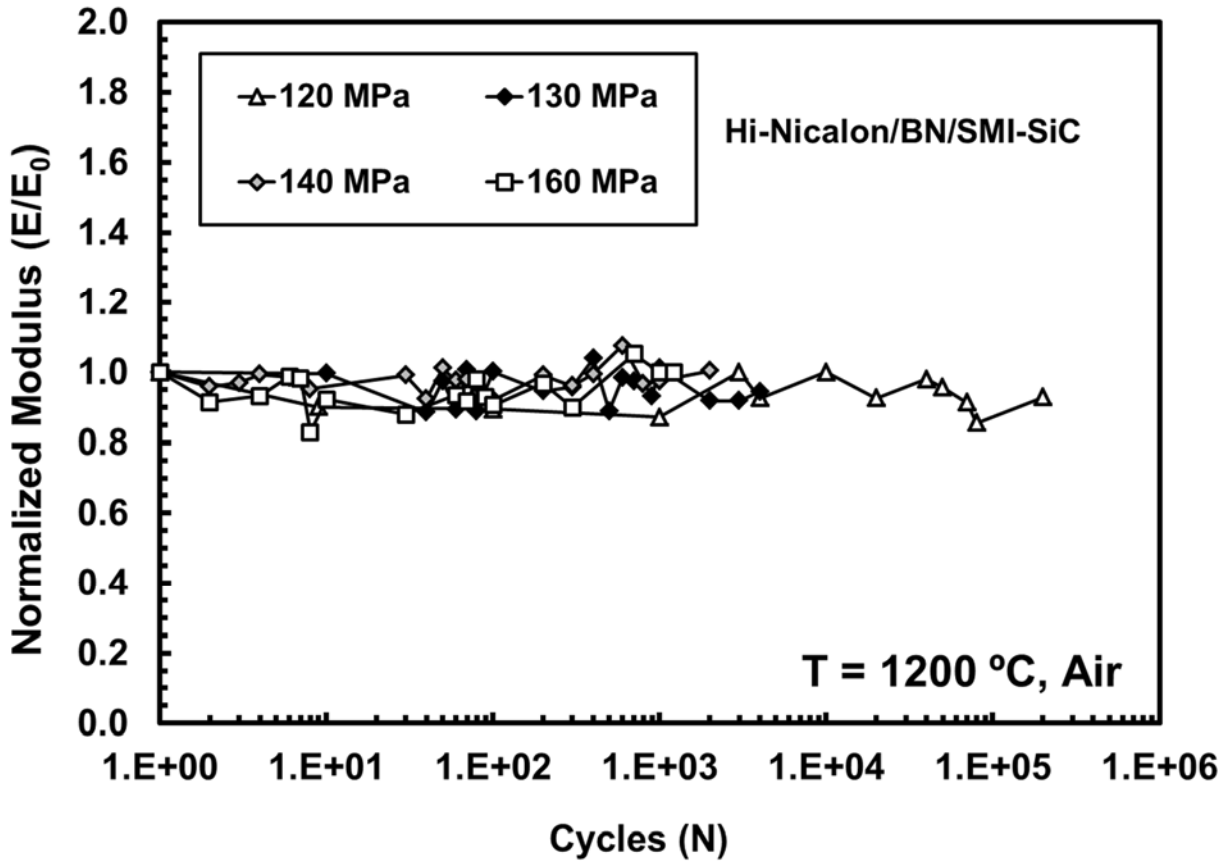

Figure 22: Normalized modulus vs. fatigue cycles for Hi-Nicalon™/BN/SMI-SiC at 1200°C in air

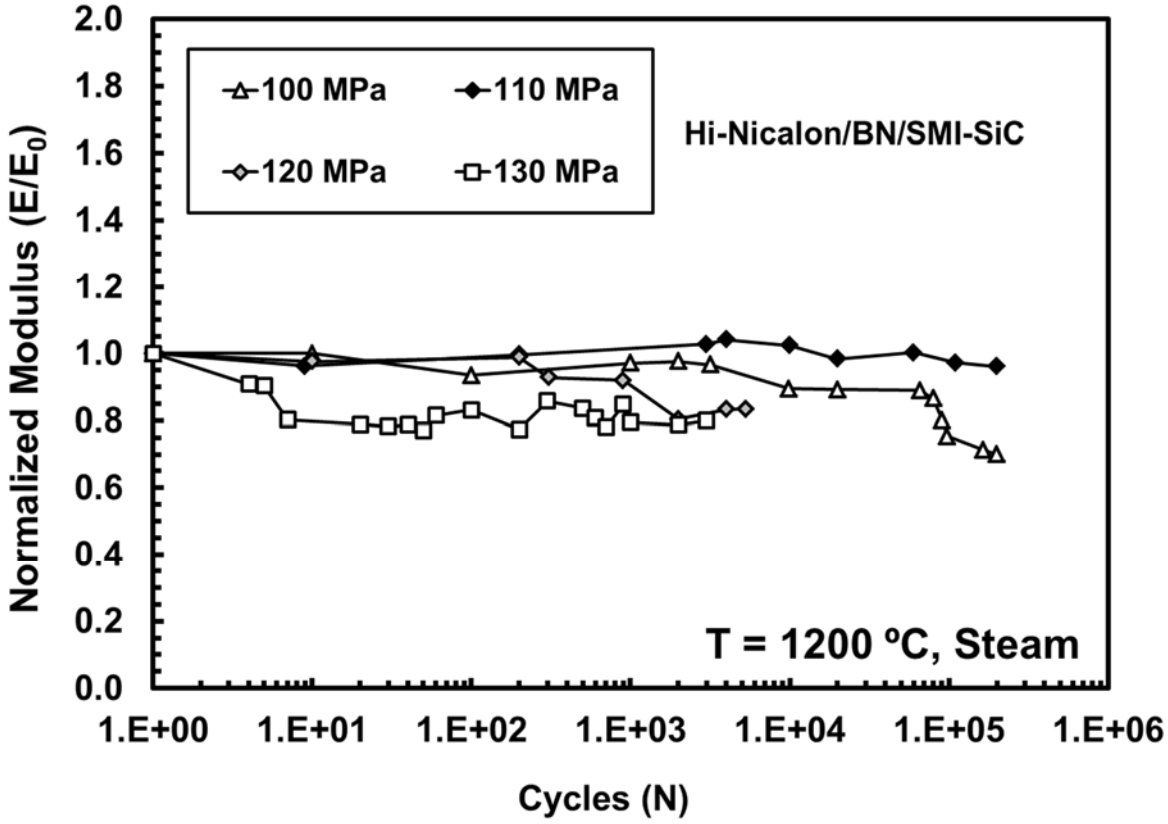

Figure 23: Normalized modulus vs. cycle for Hi-Nicalon™/BN/SMI-SiC at 1200°C in steam.

The change in composite modulus with fatigue cycles at 1200°C obtained for Hi-Nicalon™/BN/SMI-SiC composite in this work is compared to the results obtained for Hi-Nicalon™/BN/CVI-SiC [33] and Hi-Nicalon™/SiC-B_4C [34] composites in Figures 24 and 25. At 1200°C in air the Hi-Nicalon™/BN/SMI-SiC composite exhibits modulus behavior similar to that observed for the Hi-Nicalon™/BN/CVI-SiC composite. We note little modulus change with fatigue cycles for both CMCs. However, at 1200°C in steam, the modulus behavior of the Hi-Nicalon™/BN/SMI-SiC exhibits a trend similar to that observed for the Hi-Nicalon™/SiC-B_4C composite with the oxidation-inhibited multilayered matrix, though not quite to the same extent.

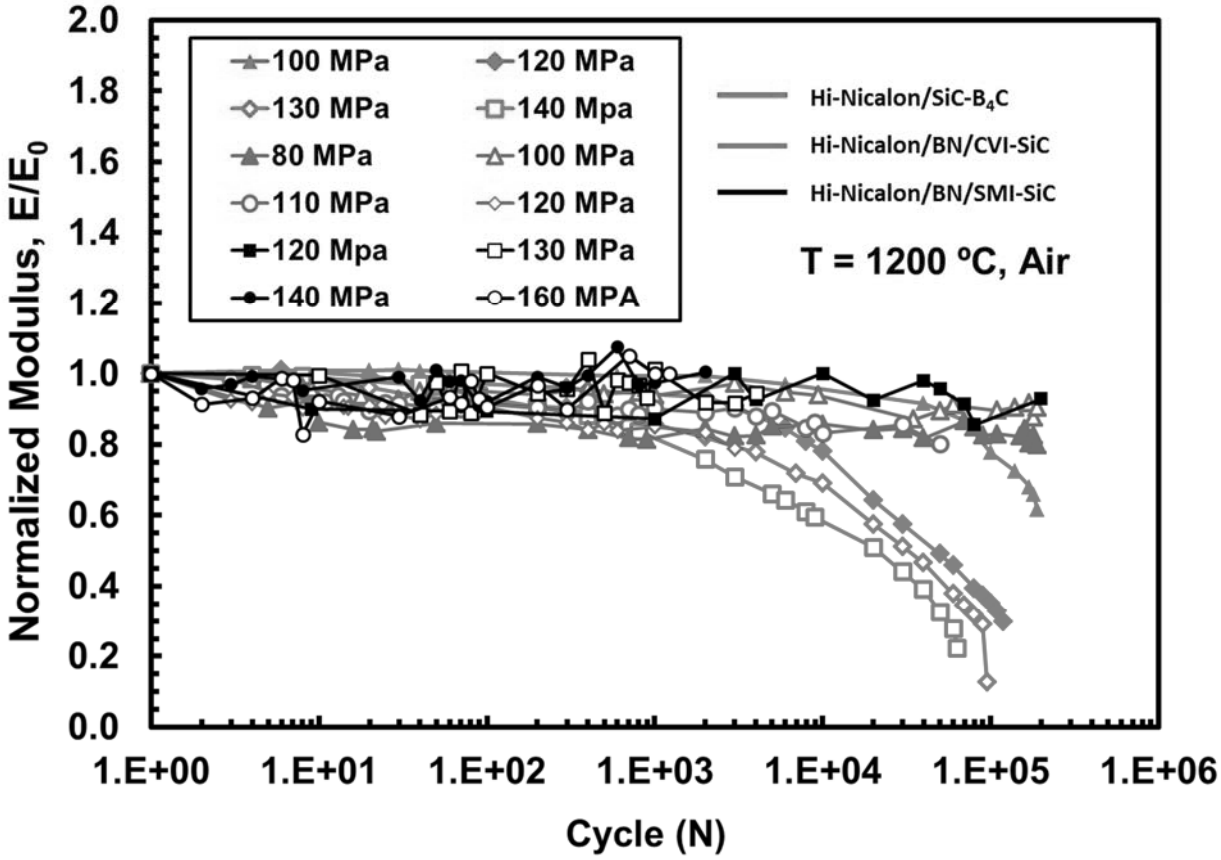

Figure 24: Normalized modulus vs. fatigue cycles for Hi-Nicalon™/BN/SMI-SiC, Hi-Nicalon™/BN/CVI-SiC and Hi-Nicalon™/SiC-B_4C composites at 1200 ^{0}C in laboratory air. Data for Hi-Nicalon™/BN/SiC from Christensen [33]. Data for Hi-Nicalon™/SiC-B_4C from Delapasse [34].

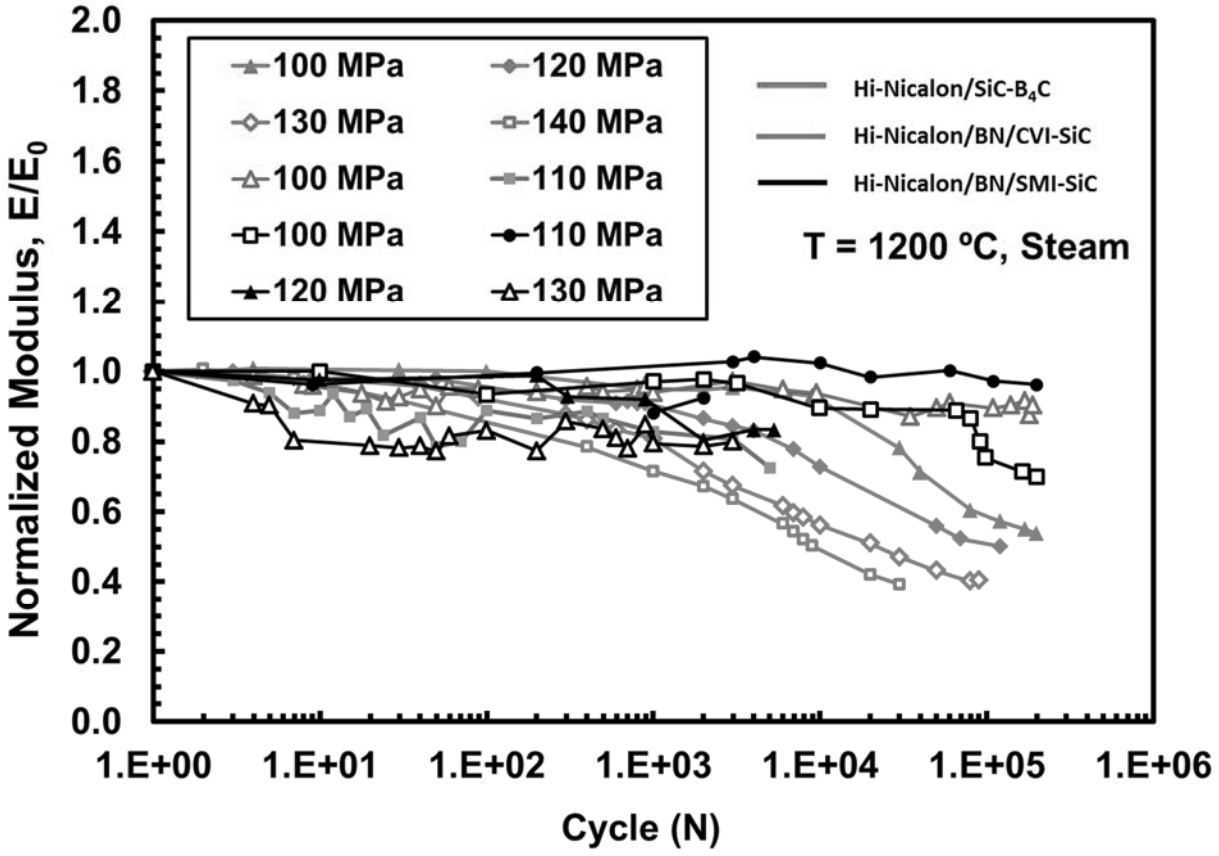

Figure 25: Normalized modulus vs. fatigue cycles for Hi-Nicalon™/BN/SMI-SiC, Hi-Nicalon™/BN/CVI-SiC and Hi-Nicalon™/SiC-B_4C composites at 1200°C in steam. Data for Hi-Nicalon™/BN/CVI-SiC from Christensen [33]. Data for Hi-Nicalon™/SiC-B_4C from Delapasse [34].

Strain accumulation was measured at the minimum stress level of each cycle during testing as another way to measure damage accumulation [46]. Cyclic strains as functions of fatigue cycles for fatigue tests conducted at 1200°C in air and in steam are shown in Figs. 26 and 27, respectively.

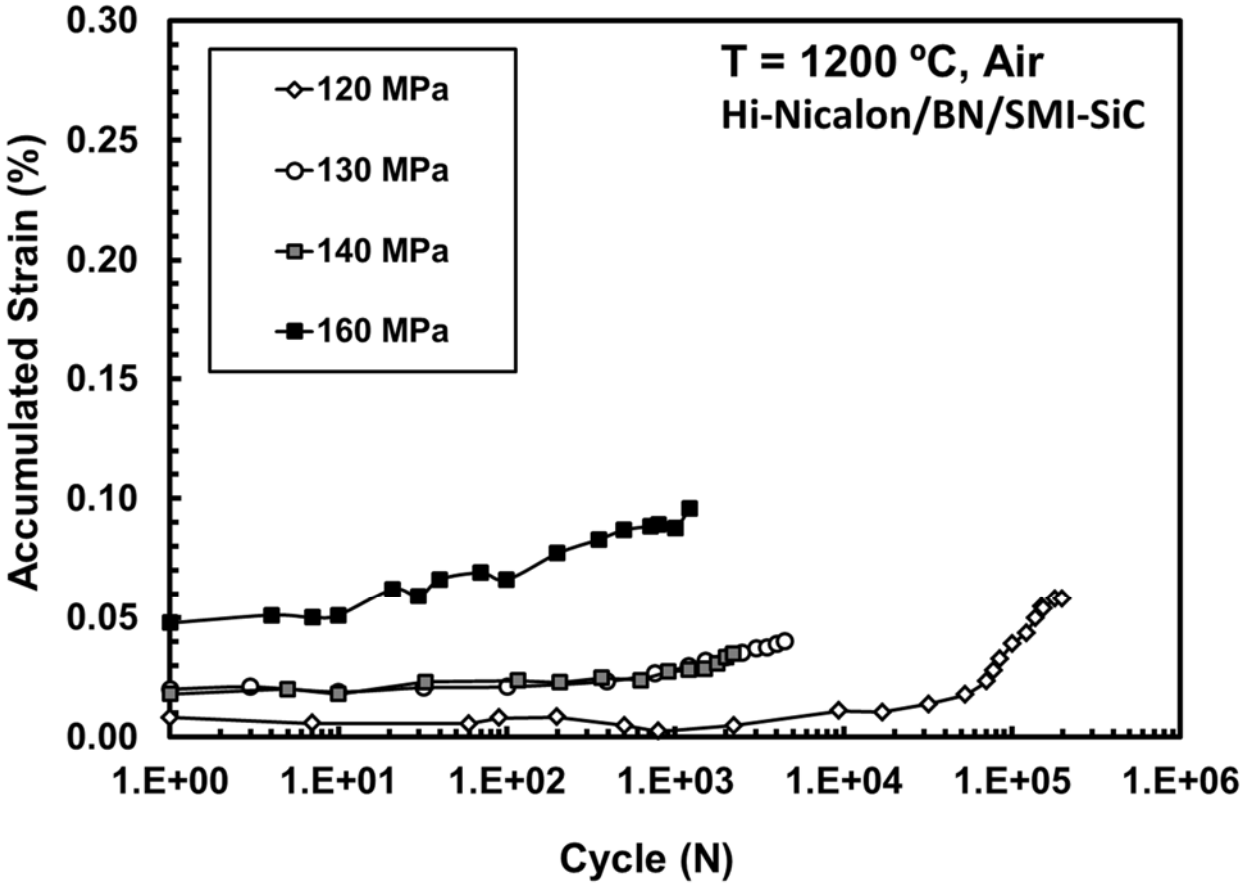

Figure 26: Strain accumulation over fatigue cycles for Hi-Nicalon™/BN/SMI-SiC ceramic composite at 1200°C in air.

Results in Figures 26 and 27 show little strain accumulation with cycles. Yet some strain ratchetting (progressive strain accumulation with cycles) is seen in tests performed with higher levels of maximum stress (see for example the 160 MPa test in air and the 130 MPa test in steam). The specimen tested in fatigue at 120 MPa in air reached run-out but still showed strain accumulation after 10^5 cycles. In the case of the specimen tested in fatigue with a maximum stress level of 160 MPa, the material acquires a relatively large permanent strain in the first cycle, and shows smaller accumulation in the subsequent cycles before failure.

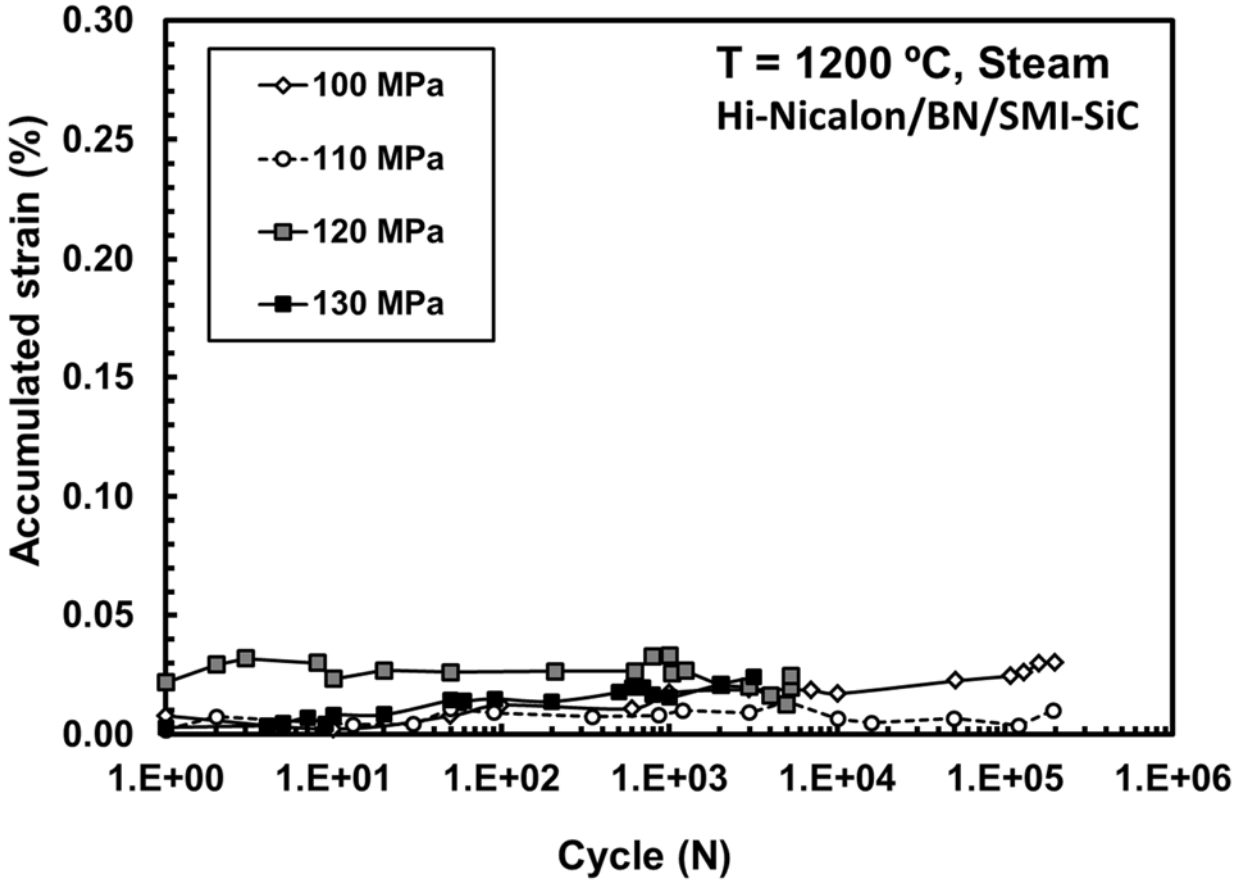

Figure 27: Strain accumulation with fatigue cycles for Hi-Nicalon/BN/SMI-SiC ceramic composite at 1200°C in steam.

Strain accumulation with fatigue cycles at 1200°C obtained for Hi-Nicalon™/BN/SMI-SiC composite in this work is compared to the results obtained for Hi-Nicalon™/BN/CVI-SiC [33] and Hi-Nicalon™/SiC-B_4C [34] composites in Figures 28 and 29. The largest strains are accumulated by the Hi-Nicalon™/SiC-B_4C composite with the oxidation inhibited matrix. The strains accumulated by the Hi-Nicalon™/BN/SMI-SiC composite in this work are comparable to those reported by Christensen for the Hi-Nicalon™/BN/CVI-SiC composite.

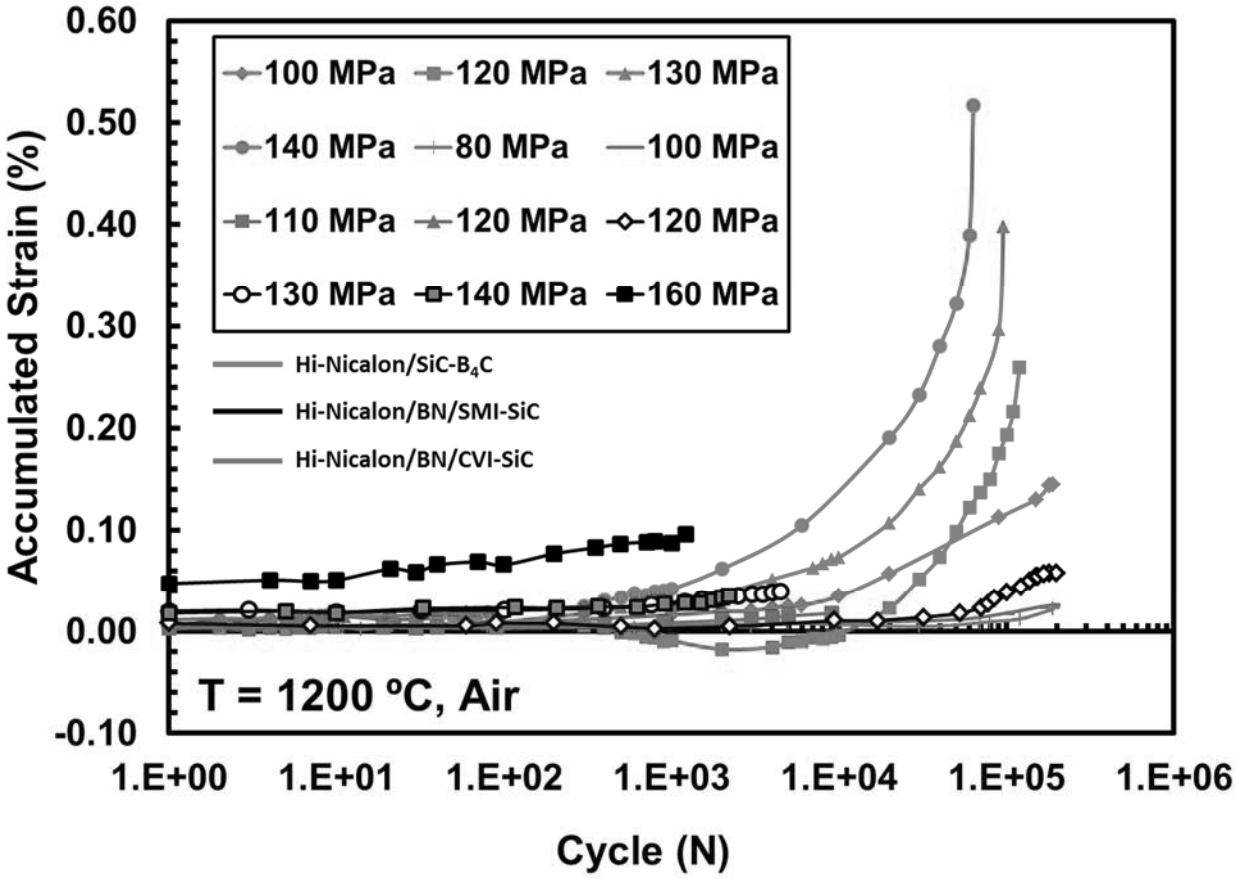

Figure 28: Strain accumulation with fatigue cycles for Hi-Nicalon™/BN/SMI-SiC, Hi-Nicalon™/BN/CVI-SiC and Hi-Nicalon™/SiC-B_4C composites at 1200 ^{0}C in air. Data for Hi-Nicalon/BN/SiC from Christensen [33]. Data for Hi-Nicalon™/SiC-B_4C from Delapasse [34].

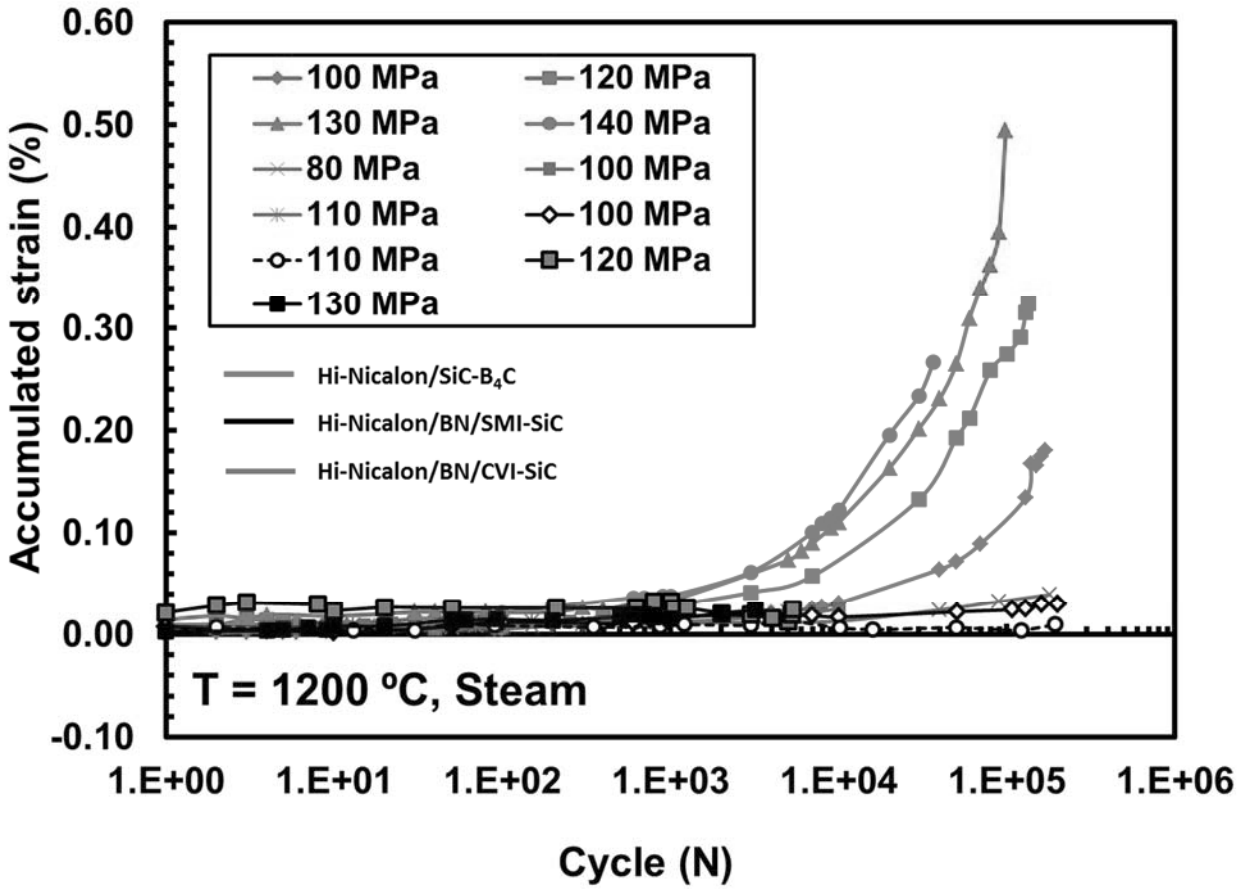

Figure 29: Strain accumulation with fatigue cycles for Hi-Nicalon™/BN/SMI-SiC, Hi-Nicalon™/BN/CVI-SiC and Hi-Nicalon™/SiC-B_4C composites at 1200°C in steam. Data for Hi-Nicalon/BN/CVI-SiC from Christensen [33]. Data for Hi-Nicalon™/SiC-B_4C from Delapasse [34].

5.5 Effects of Prior Fatigue on Tensile Properties

All specimens that achieved fatigue run-out of $2x10^5$ cycles were tested in tension to failure at 1200°C to assess the retained tensile properties. In this work, one specimen achieved fatigue run-out in air, and two specimens achieved fatigue run-out in steam. Once 200,000 cycles was reached, the specimens went through a tensile test to evaluate the retained tensile properties. The retained tensile properties are summarized in Table 11. The stress-strain curves obtained from these tensile tests showed nearly bi-linear behavior akin to that exhibited by the as-processed specimen (see Section 5.3).

Table 11: Retained tensile properties of Hi-Nicalon™/BN/SMI-SiC specimens subjected to $2x10^5$ fatigue cycles at 1200°C.

Fatigue Stress (MPa)	Test Environment	Retained Strength (MPa)	Strength Retention (%)	Retained Modulus (GPa)	Modulus Retention (%)	Failure Strain (%)
120	Air	231	96.7	140	64.6	0.395
100	Steam	216	90.4	83.0	38.2	0.402
110	Steam	198	82.8	195	89.8	0.350

Each of the run-out specimens retained a high percentage of ultimate strength regardless of test environment, as Figure 30 illustrates. In contrast, Delapasse observed that the oxidation-inhibited material retained only 40%-60% of its tensile strength. The full comparison of materials is listed in Table 12. The melt-infiltrated material is again comparable to the CVI-SiC/SiC material, though the CVI material showed better strength retention (100% in each test) and better modulus retention.

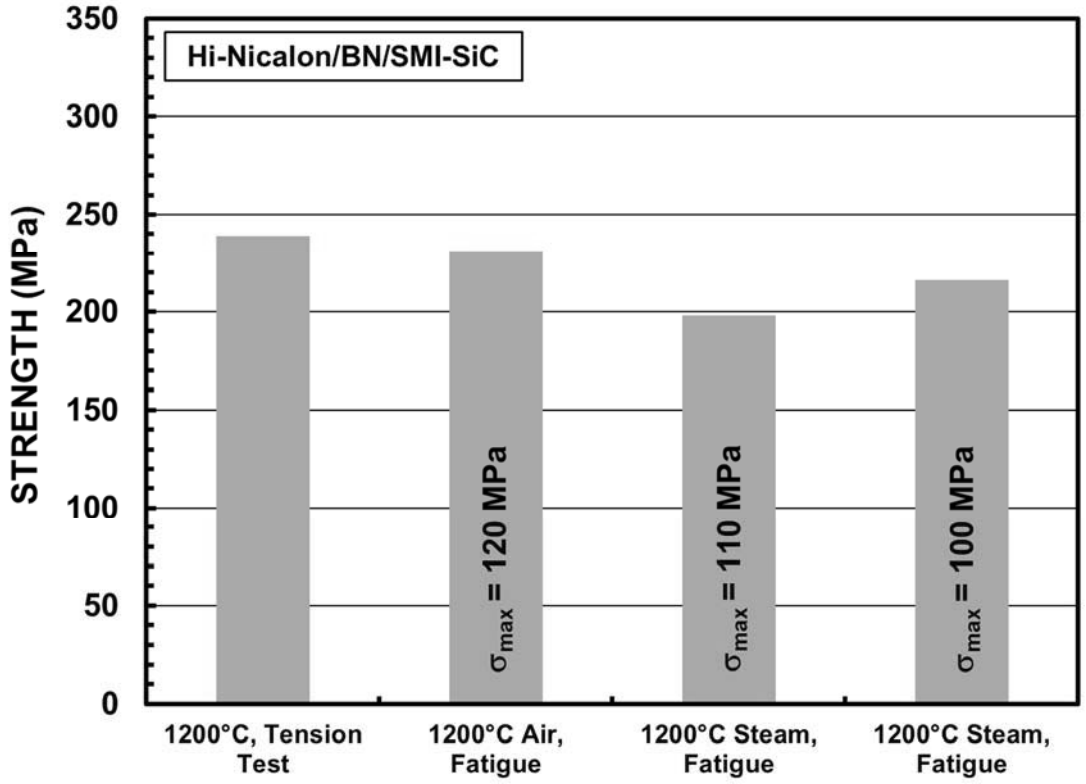

Figure 30: Retained tensile strength of the Hi-Nicalon™/BN/SMI-SiC specimens subjected to prior fatigue in air and in steam at 1200°C.

Table 12: Retained tensile properties of Hi-Nicalon™/BN/SMI-SiC, Hi-Nicalon™/BN/CVI-SiC and Hi-Nicalon™/SiC-B_4C specimens subjected to $2x10^5$ fatigue cycles at 1200°C. Data for Hi-Nicalon/BN/CVI-SiC from Christensen [33]. Data for Hi-Nicalon™/SiC-B_4C from Delapasse [34].

Maximum Stress (MPa)	Test Environment	Retained Strength (MPa)	Strength Retention (%)	Retained Modulus (GPa)	Modulus Retention (%)	Failure Strain (%)
Hi-Nicalon™/BN/SMI-SiC						
120	Air	231	96.7	140	64.6	0.395
100	Steam	216	90.4	83.0	38.2	0.402
110	Steam	198	82.8	195	89.8	0.350
Hi-Nicalon™/BN/SiC-B_4C[b]						
100	Air	130	42.4	171	83.1	0.196
100	Steam	183	59.7	141	68.6	0.345
Hi-Nicalon™/BN/CVI-SiC[a]						
100	Air	248	100	208	88.2	0.496
80	Air	267	100	224	94.9	0.503
80	Steam	229	100	221	93.6	0.395

a. Data from Christensen [31]
b. Data from Delapasse [32]

5.6 Composite Microstructure

5.6.1 Microstructural Characterization of As-Processed Material

Samples of as-processed material were cut, mounted and polished to show the typical microstructure of the composite. Figure 31 shows which views were shown once the specimens were mounted.

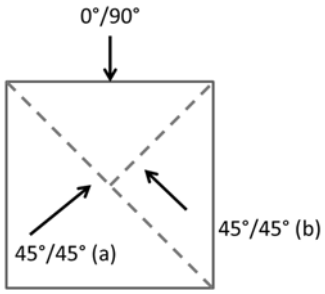

Figure 31: Section views of as-processed material sample

The overview micrograph of the as-processed material in Figure 32 clearly shows the fiber pattern as well as numerous voids in the composite. Large voids seen in the matrix material were unevenly distributed. Different phases of the matrix material were unevenly distributed.

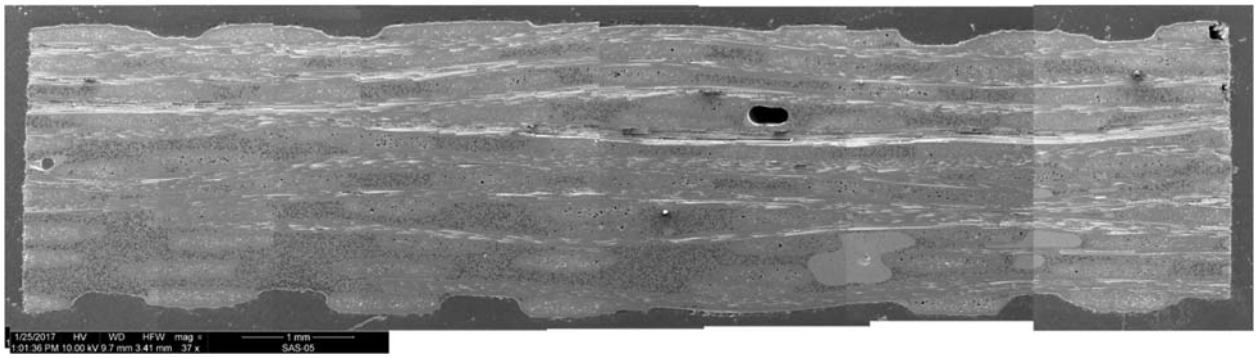

Figure 32: Overview of composite microstructure. Matrix phase distribution is irregular, large amounts of free silicon are seen as light regions in the bottom right corner.

Figure 33 shows various typical microstructural features observed in this work: Figure 33(a) shows voids starting at the surface and penetrating ~1 mm into the specimen. Image 33(b) shows a large matrix void, presumably formed in the course of melt infiltration. Image 33(c) shows that the cross sectional area of a void is on the same order or magnitude as the cross sectional area of a fiber bundle. Presence of such large voids is bound to reduce the load bearing capacity of the material. Image 33(d) shows a Si-rich zone in the matrix.

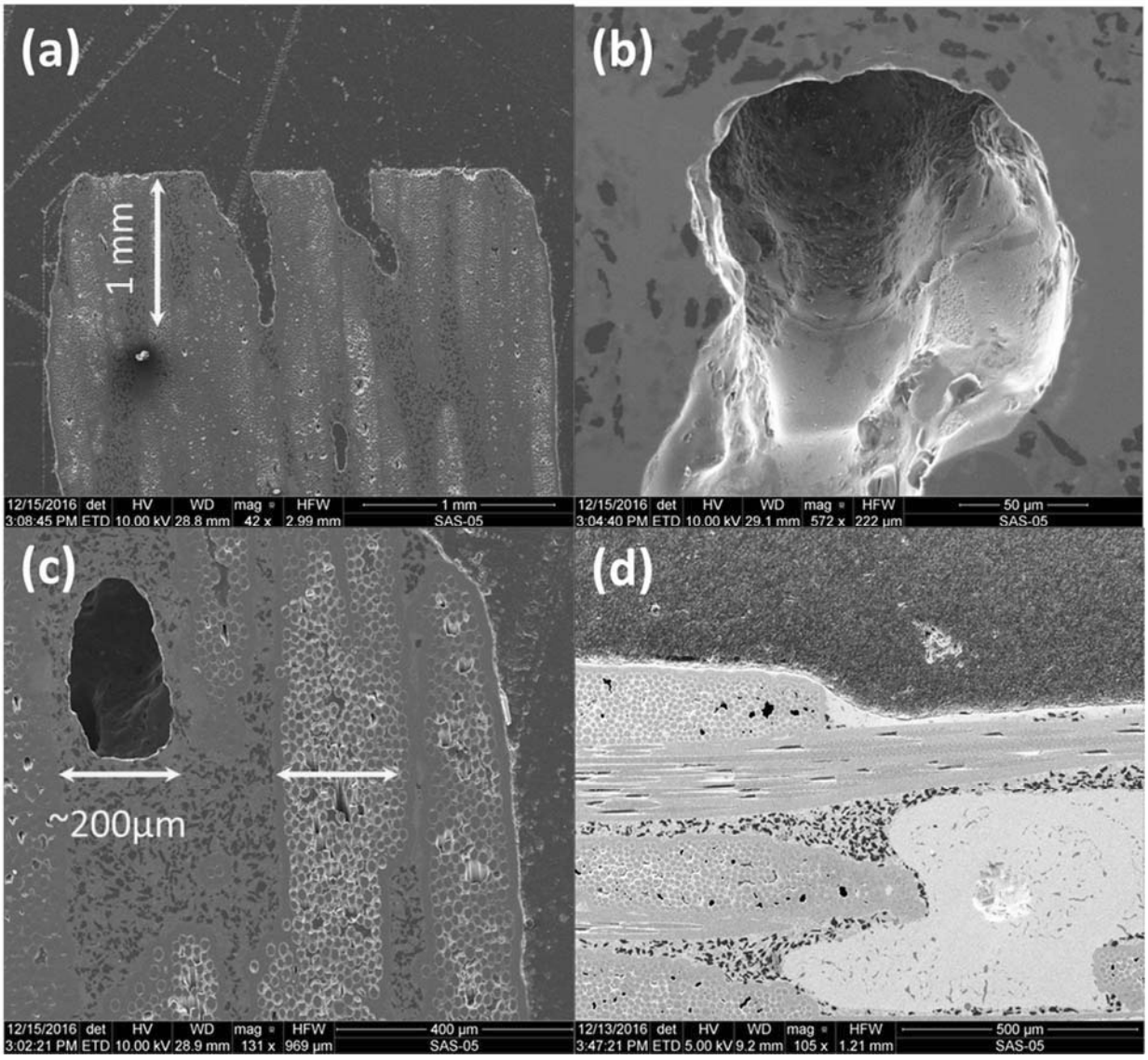

Figure 33: SEM micrographs of the as-processed composite showing (a) surface defects penetrating deep into the composite interior; (b) a large matrix void; (c) void cross sectional area being close in size to that of the fiber bundle; (d) Uneven distribution of different matrix phases

Figure 34 also shows typical microstructure of the composites. Both 0° and 90° fiber bundles are clearly visible as is a CVI SiC layer around the 0° fibers. Figure 35 shows the typical distribution of voids within a fiber bundle. Such voids are caused by poor infiltration of the matrix material into the 90° fiber bundle.

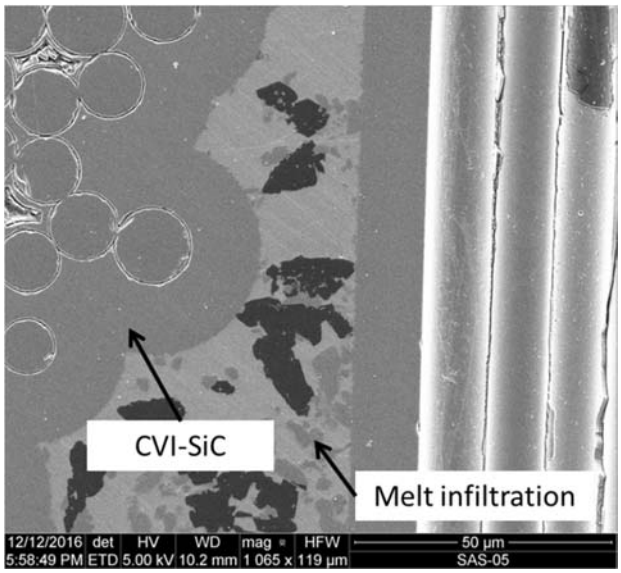

Figure 34: Typical microstructure of as-processed Hi-Nicalon™/BN/SMI-SiC

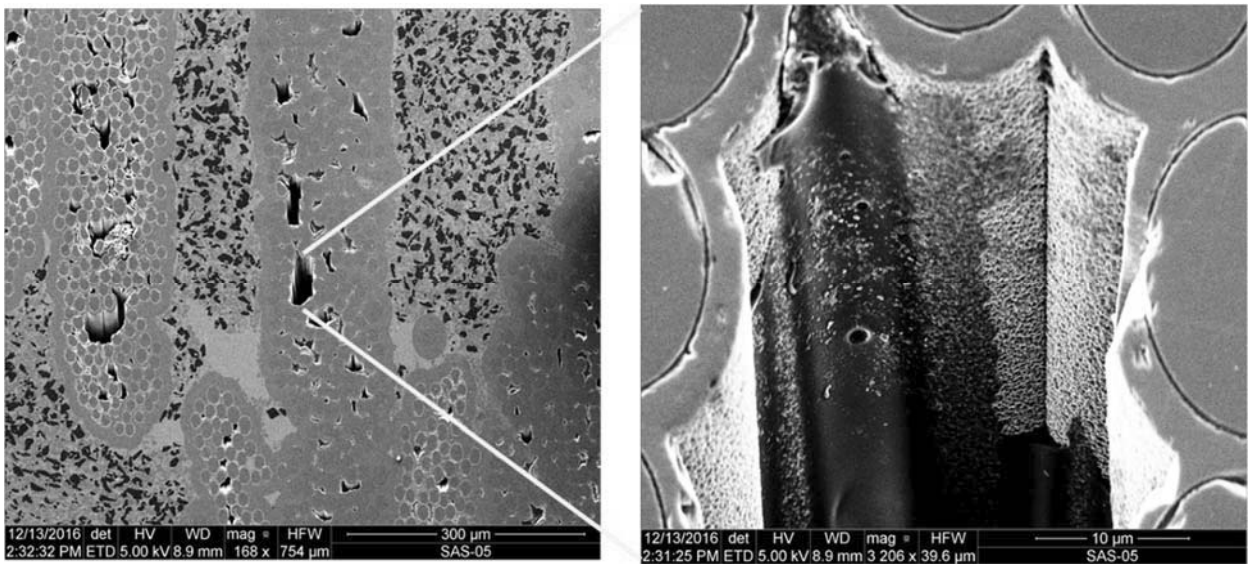

Figure 35: Voids within fiber bundles due to initial CVI densification of SiC

5.6.2 Microstructural Characterization of the Specimen Failed in Tensile Test

Optical micrographs of the specimen tested in tension to failure at 1200°C in air are shown in Figures 36 and 37. Individual fiber pull-out is observed in the interior region of the fracture surface, while whole fiber tows have pulled out near the exterior faces of the specimen.

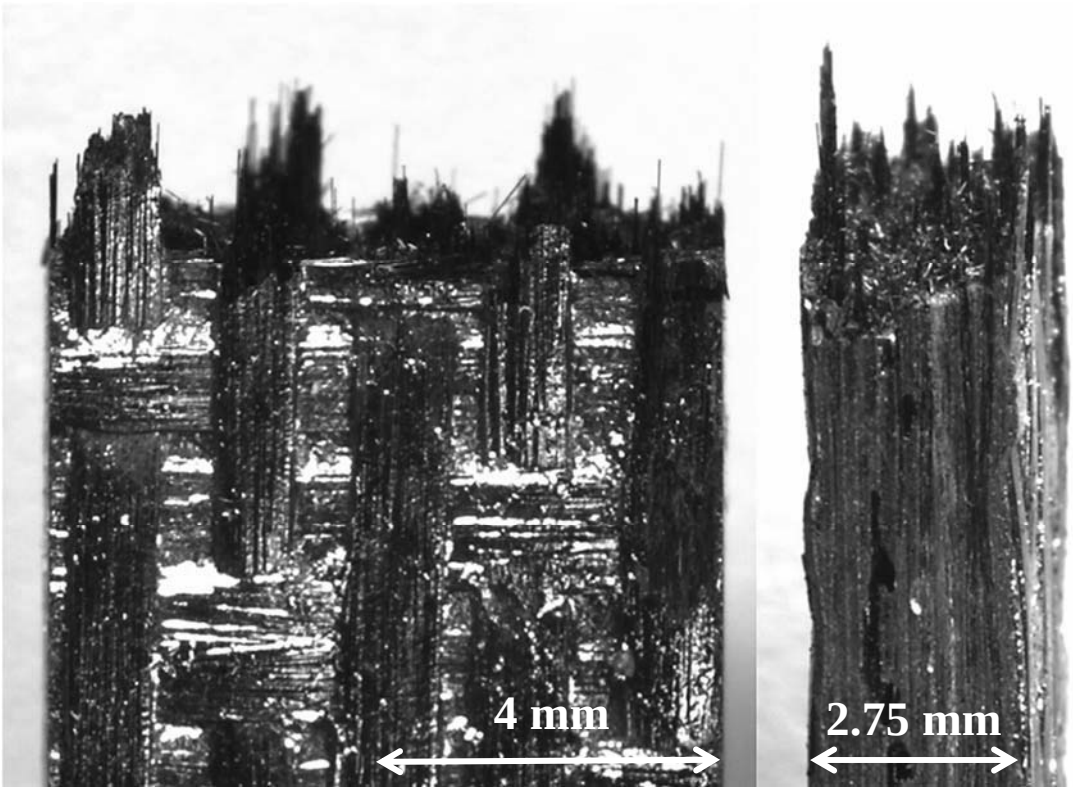

Figure 36: Tensile specimen fracture surface

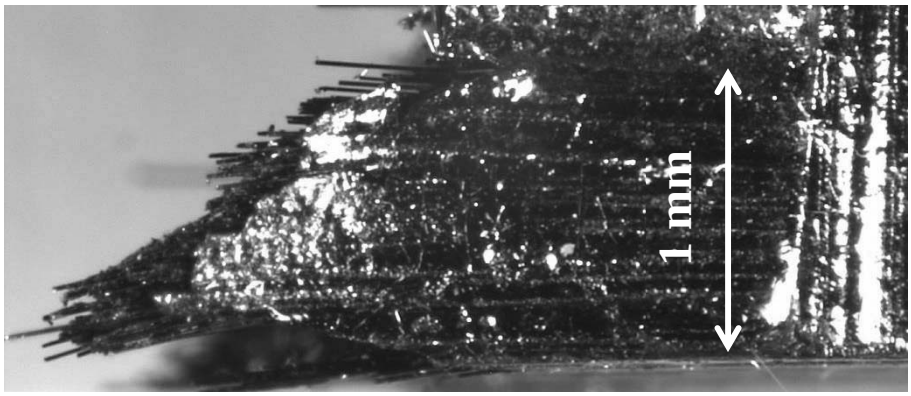

Figure 37: Optical micrograph of the specimen tested in tension to failure at 1200° C in air showing exterior tow pull-out

Figure 38 shows the fracture surface of the specimen tested in tension to failure at 1200°C in air. The fracture surface is predominantly not oxidized. Most of the fracture surface exhibits fiber pull-out and shows no typical signs of oxidation. Such a result is not surprising considering the very short duration (< 10 s) of the tensile test. Higher magnification SEM images in Figure 39 show fiber pull-out typical in the not oxidized regions as well as "outside" debonding of the individual fibers, i.e. debonding between the BN-interphase and the CVI-SiC portion of the matrix [47].

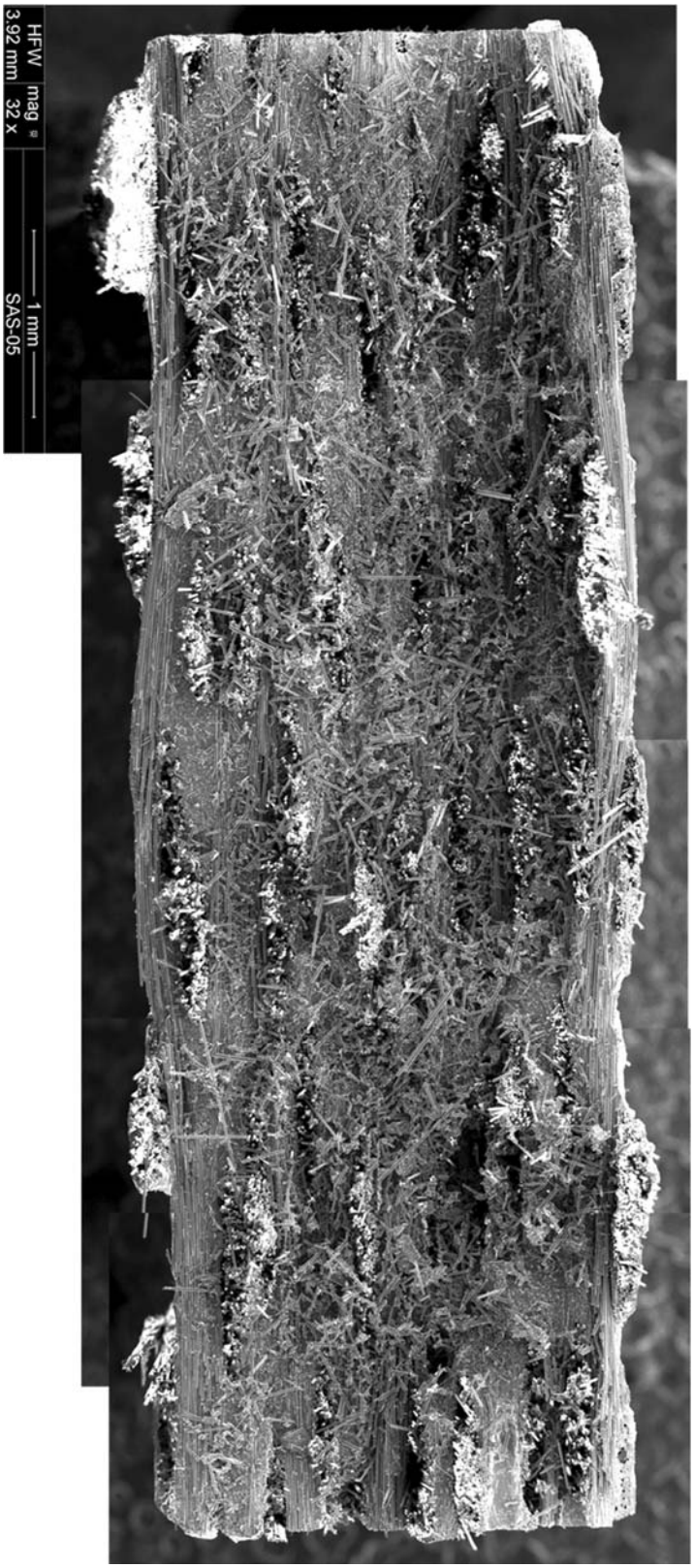

Figure 38: Fracture surface of the specimen tested in tension to failure at 1200°C in air. Fracture surface is predominantly not oxidized.

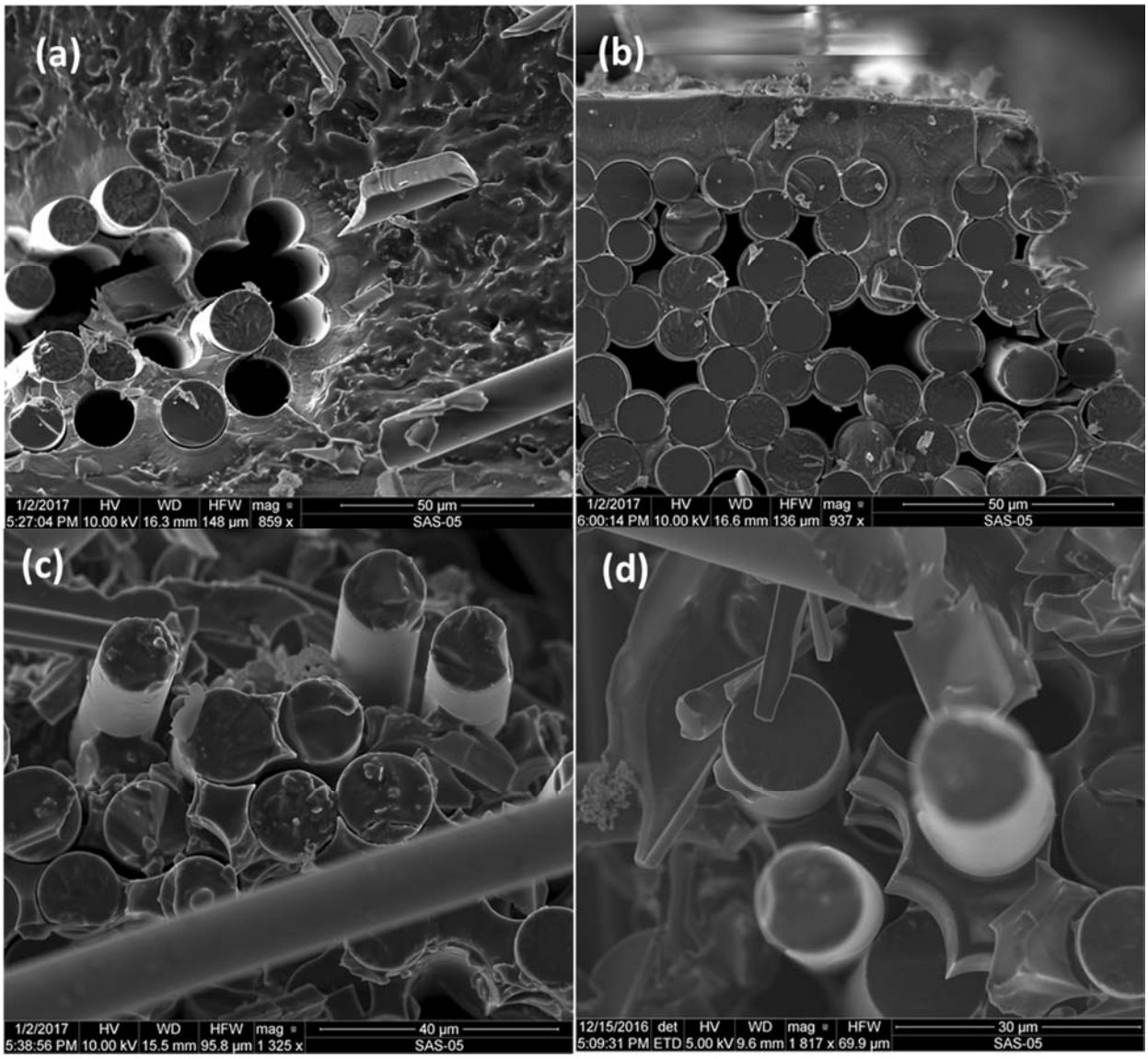

Figure 39: Higher magnification SEM images showing fiber pull-out typical in the non-oxidized regions as well as debonding between the BN-interphase and the CVI SiC portion of the matrix.

5.6.2 Microstructural Characterization of Specimens Tested in Fatigue

When a specimen failed the testing system was immediately shut off and the bottom portion of the failed specimen was removed from the furnace. Thus the interior of the fracture surface of that portion of the failed specimen was exposed to significant temperatures and prolonged oxidation at most for a few minutes as it cooled. These are the fracture surfaces that were examined under the microscope.

Optical and SEM micrographs of the fracture surfaces of specimens tested in air are presented in Figures 40-43. The specimen tested in fatigue in air at 1200°C with a maximum stress level of 120 MPa is shown in Figure 40. The specimen survived for 200,000 cycles. The fracture surface is brushy across the entire surface.

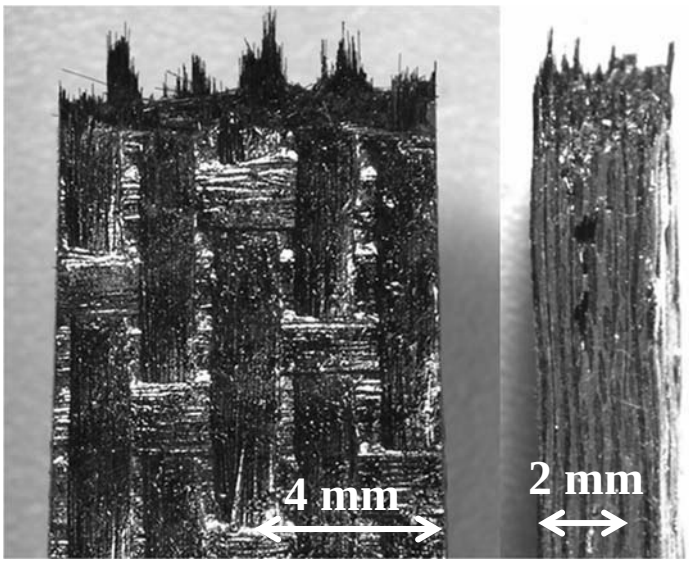

Figure 40: Optical micrograph of specimen 16-031 tested in tension-tension fatigue at 1200°C in air. σ_{max} = 120 MPa, N_f >200,000

An overview SEM micrograph of the fracture surface is shown in Figure 41. Features indicating oxidation such as flat fracture surfaces, fused fibers, and smooth, glassy regions [43], are not apparent or confined to the extreme outside edge of the surface. Thus it is unlikely that

oxidation embrittlement was a failure mechanism in this specimen and we conclude that the threshold stress level [48] for subcritical crack growth was not crossed for this specimen.

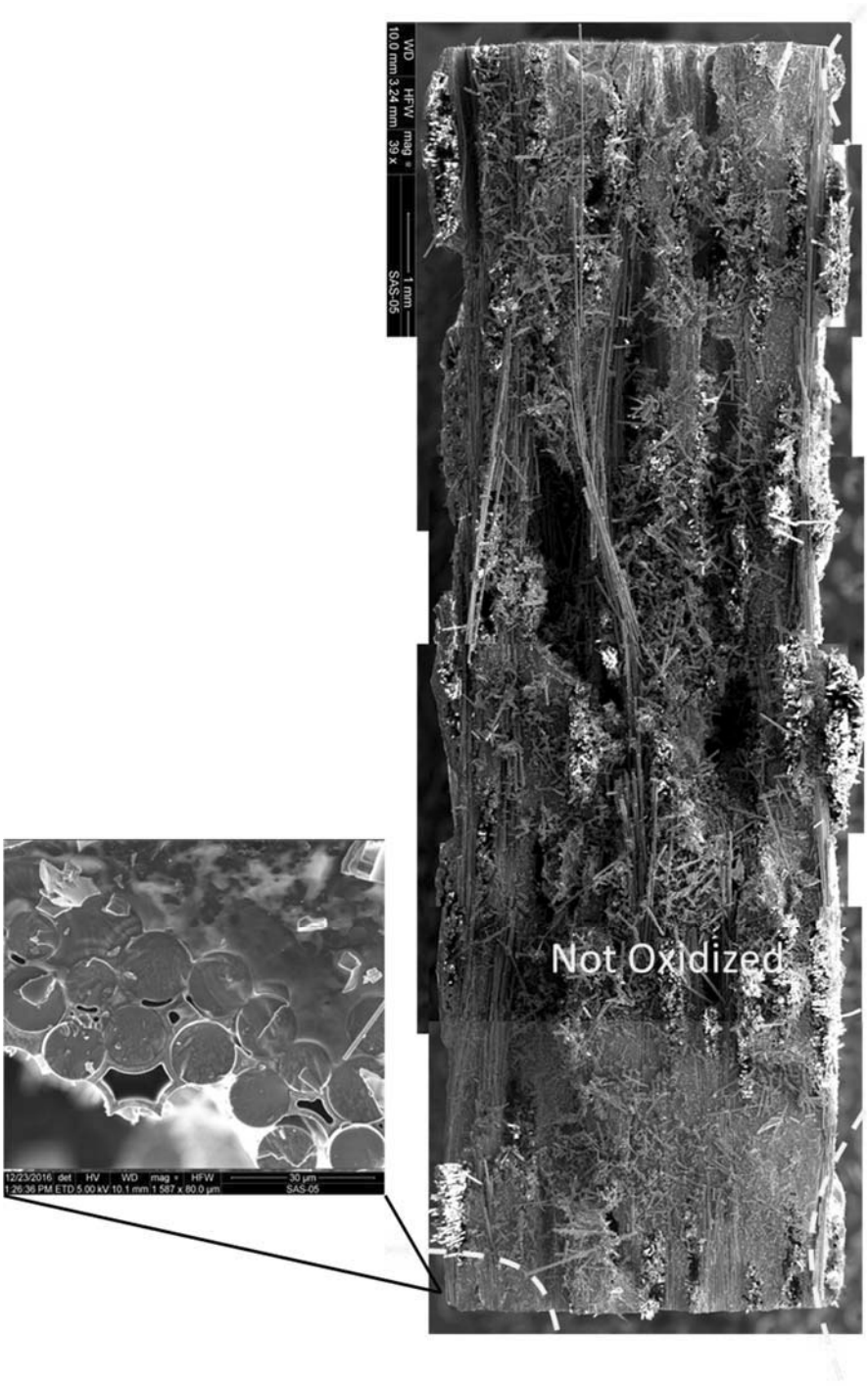

Figure 41: SEM overview of the fracture surface of the specimen tested in tension-tension fatigue at 1200°C in air. σ_{max} = 120 MPa, N_f >200,000. Some fiber-to-fiber bonding indicating oxidation was observed on the exterior of the fracture surface (inset).

Figure 42 shows the specimen tested in fatigue in air at 1200°C with a higher maximum stress level of 140 MPa. The specimen survived for only 2,200 cycles, indicating that the stress level was above the threshold for causing crack growth. The fracture surface exhibits more fiber pull-out on one side than the other, indicating that oxidation-assisted unbridged crack growth may have initiated from the edge of the specimen with less pull-out. This is similar to fracture surface characteristics observed in prior work on melt-infiltrated CMCs [49].

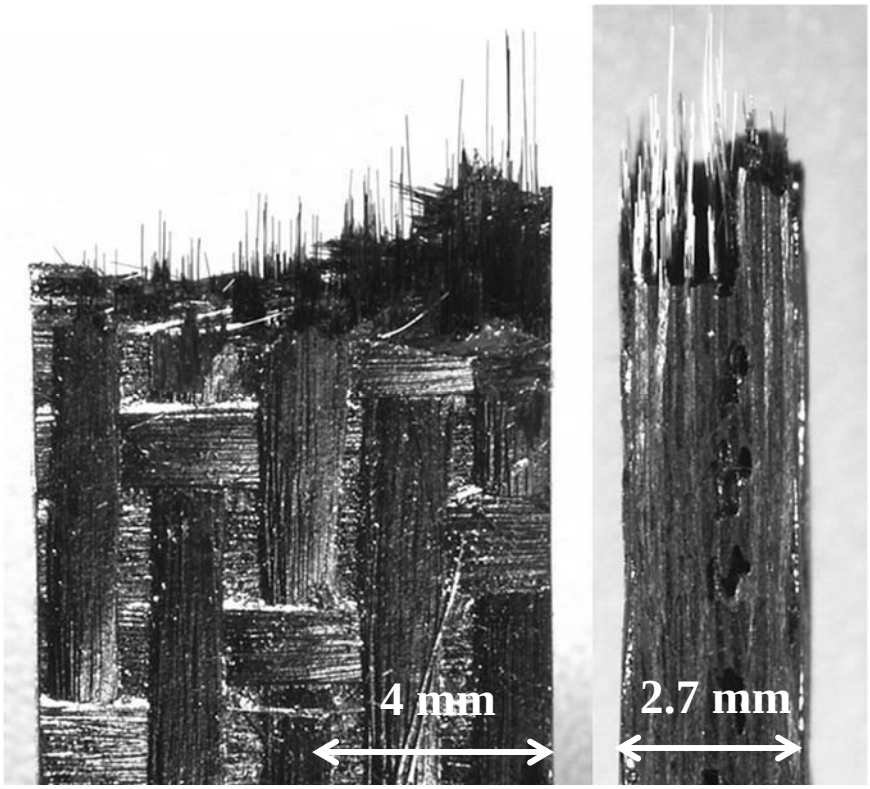

Figure 42: Optical micrograph of specimen 16-045 tested in tension-tension fatigue at 1200°C in air. σ_{max} = 140 MPa, N_f =2,200

Figure 43 shows the SEM overview of the surface. The specimen has a glassy phase and fused fibers present in one region of the surface, indicating oxidation. Additionally, the distribution of large voids characteristic of the material is evident. Unbridged oxidation-assisted crack growth appears to have occurred until the flaw reached the internal voids. At this point the remaining ligament could not withstand the applied stress and failed.

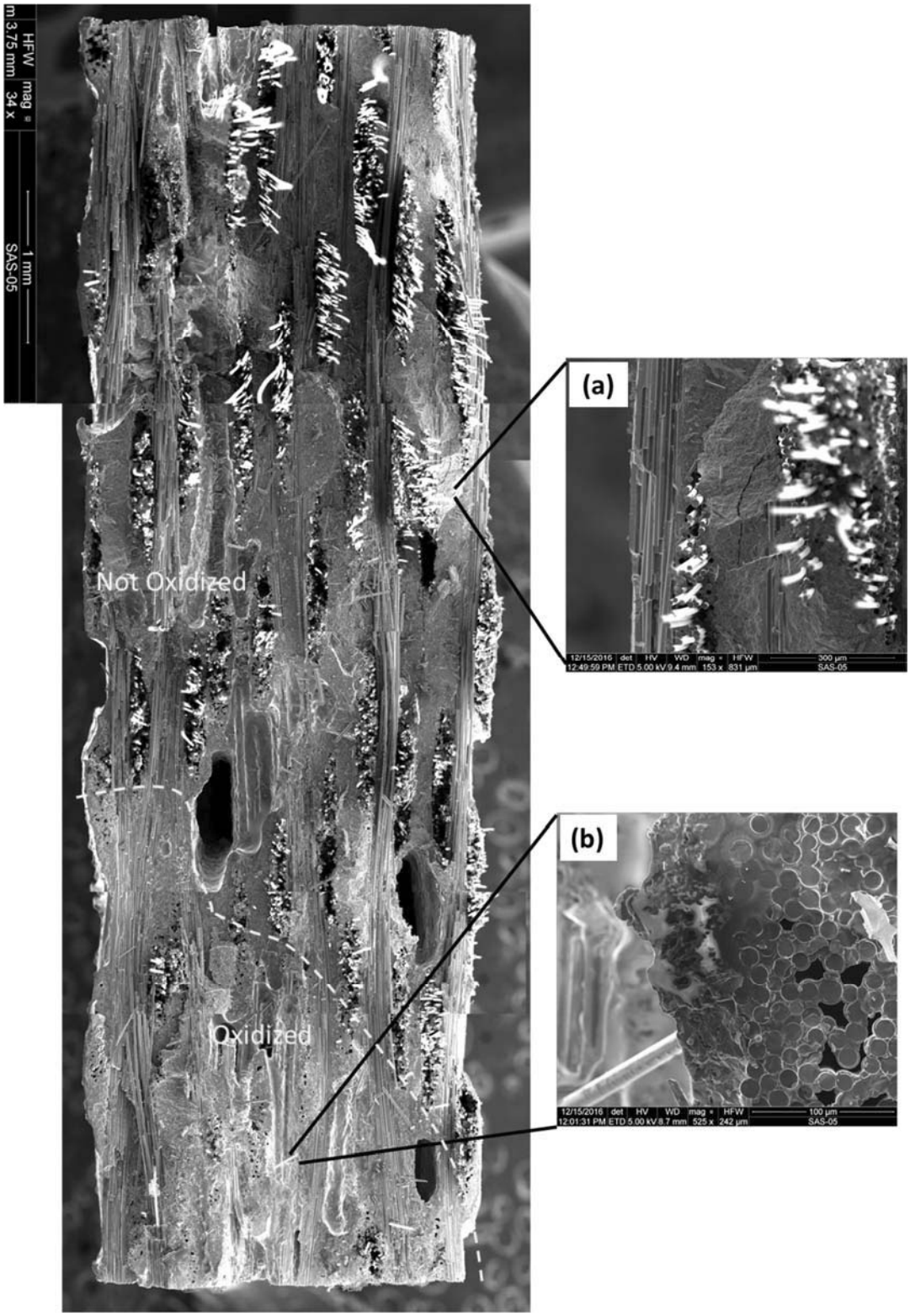

Figure 43: SEM micrographs of the specimen tested in fatigue at 1200°C in air. σ_{max} = 140 MPa, N_f =2,200. (a) Fiber pull-out and matrix cracking in non-oxidized region; (b) fused fibers with single fracture plane alongside glassy features in oxide region

Similar threshold crack growth behavior was observed in the specimens fatigue tested at 1200°C in steam. The specimen that was fatigue tested with a maximum stress of 100 MPa achieved a run-out. The specimen that was fatigue tested with a maximum stress of 120 MPa failed in 5,311 cycles. Optical micrographs of the specimens are shown in Figures 44 and 45, respectively. The fracture surface of the specimen that reached run-out is more uniformly brushy while the fracture surface of the specimen with the shorter life has one side that shows more pull-out than the other.

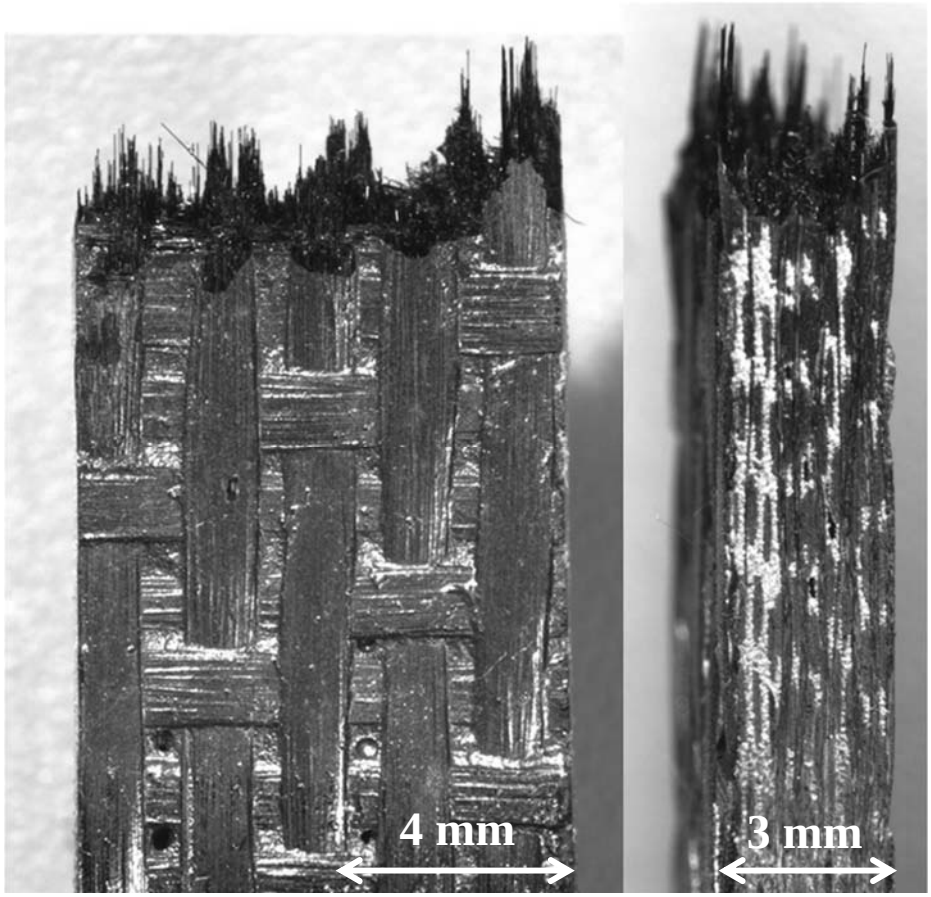

Figure 44: Optical micrograph of specimen 16-033 tested in tension-tension fatigue at 1200°C in steam. σ_{max} = 100 MPa, N_f >200,000

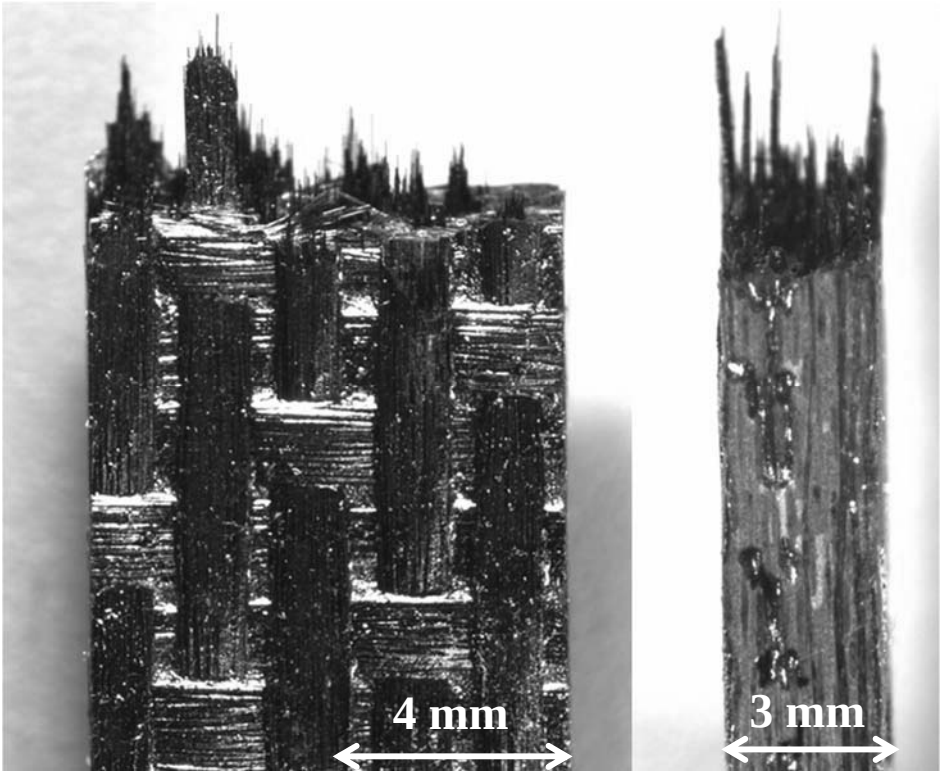

Figure 45: Optical micrograph of specimen 16-032 tested in tension-tension fatigue at 1200°C in steam. σ_{max} = 120 MPa, N_f =5,311. The left side shows more fiber pull-out

The SEM overview micrographs of both fracture surfaces are compared side-by-side in Figure 46. The specimen that reached run-out (Figure 46a) shows no oxidation, indicating that there was no oxidation-assisted crack growth during fatigue testing and the maximum stress level was below the threshold for initiating a flaw. In contrast, the specimen that failed at 5,311 cycles (Figure 46b) exhibits signs of oxidation embrittlement. The short cyclic life of the specimen indicates that the maximum fatigue stress was above the threshold crack growth stress for this material. The fracture surface shows a glassy layer on one edge of the specimen, as well as fiber-to-fiber bonding, indicating that unbridged oxidation-assisted crack growth occurred in that region. Large voids are concentrated on the boundary between the oxidized and non-oxidized regions of the fracture surface. This indicates that the crack grew until reaching the void, at which point the specimen failed.

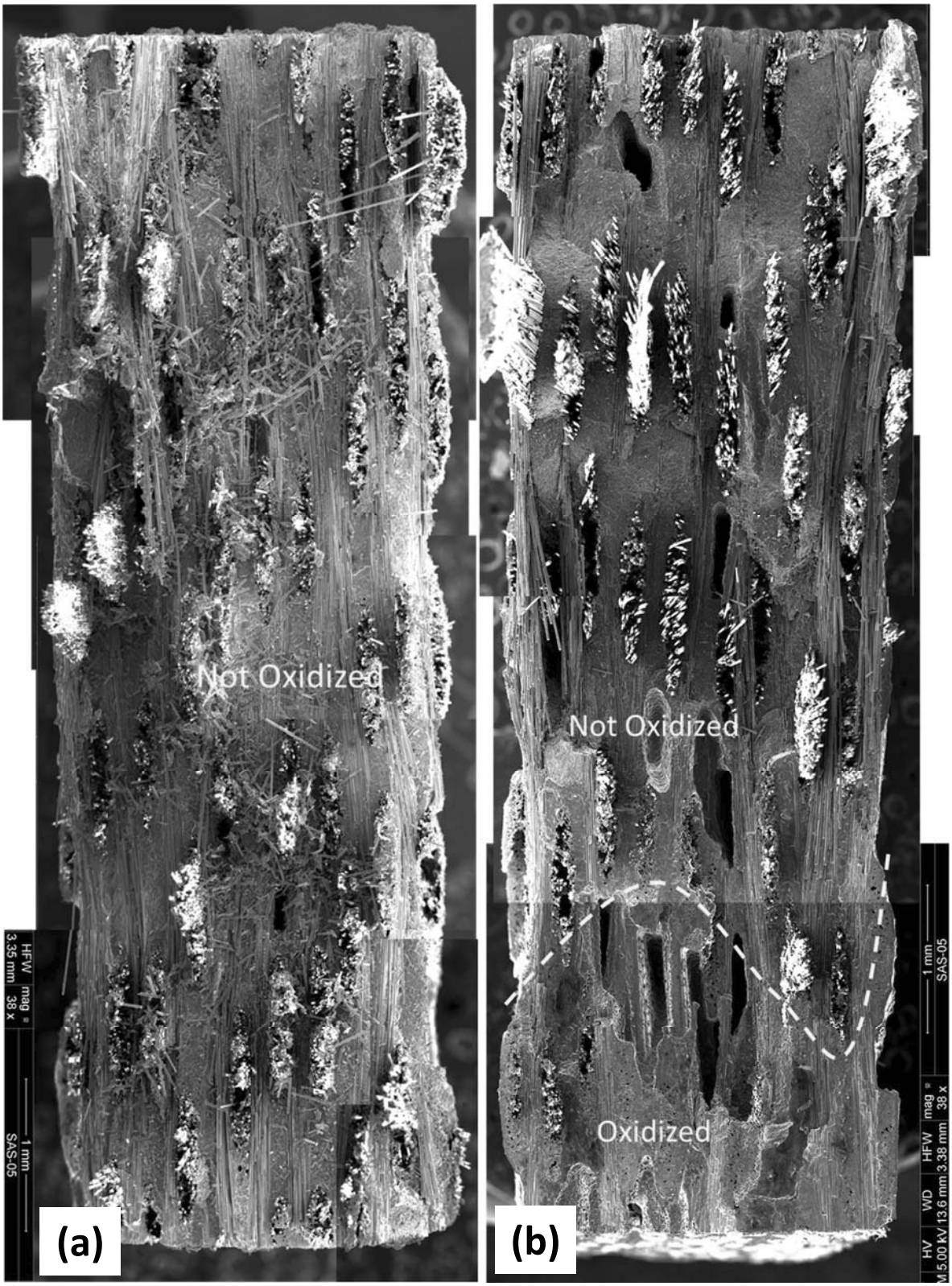

Figure 46: SEM Overviews of (a) 16-033 tested in tension-tension fatigue at 1200°C in steam. σ_{max} = 100 MPa, N_f >200,000 and (b) specimen 16-032 tested in tension-tension fatigue at 1200°C in steam. σ_{max} = 120 MPa, N_f =5,311.

Figure 47 shows higher magnification micrographs of features delineating oxidized from non-oxidized regions of the fracture surfaces of specimens tested at 1200°C in steam. Interphase bubbling and glassy whisker features were more prominent on fracture surfaces of specimens tested in steam than on the fracture surfaces of the specimens tested in air. If present, the oxidized regions of the fracture surfaces are roughly the same size regardless of whether the specimen was tested in steam or air. However, the specimens tested in steam failed at lower stresses, confirming that the oxidation-assisted crack growth failure mechanism occurs more rapidly in the presence of water vapor. Additional SEM micrographs for all specimens examined in this work are provided in Appendix B.

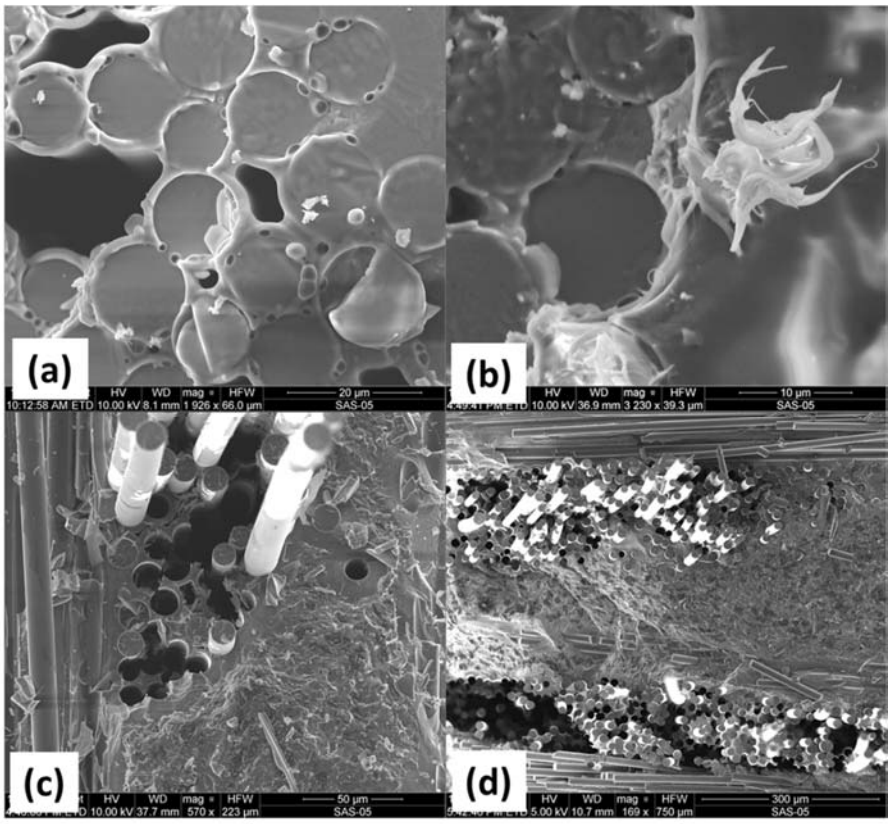

Figure 47: Higher magnification images of features from fracture surfaces of specimens fatigue tested in steam at 1200°C. (a) Oxidation indicated by smooth appearance, fiber-to-fiber bonding and bubbles from gas evolution; (b) oxidation indicated by glassy layer; (c) non-oxide region indicated by fiber pull out and rough appearance of matrix; (d) non-oxide region indicated by non-planar failure surface around fiber bundle pull-out.

5.6.3 Comparison of Microstructure to CVI-SiC/SiC Material

A comparison was made between a typical fracture surface of Hi-Nicalon^{TM}/BN/SMI-SiC tested in fatigue at 1200°C to micrographs of fracture surfaces of CVI-fabricated materials to see the different void distributions in the materials. Figure 48 illustrates how the voids influence crack propagation. This image was taken of dye-impregnated Hi-Nicalon^{TM}/BN/SMI-SiC subjected to tensile loading [50]. Figure 49 shows the comparison between Hi-Nicalon^{TM}/BN/CVI-SiC, Hi-Nicalon^{TM}/SiC-B_4C, and the present material. The CVI-fabricated specimens have small voids at the boundaries between fiber tows uniformly distributed across the surface. The voids in the MI-fabricated composite are much larger and more randomly distributed, likely due to how the matrix infiltration wicks into the fibers during fabrication. These large openings subtract a significant area from the stress-bearing cross section and can be flaw initiation sites.

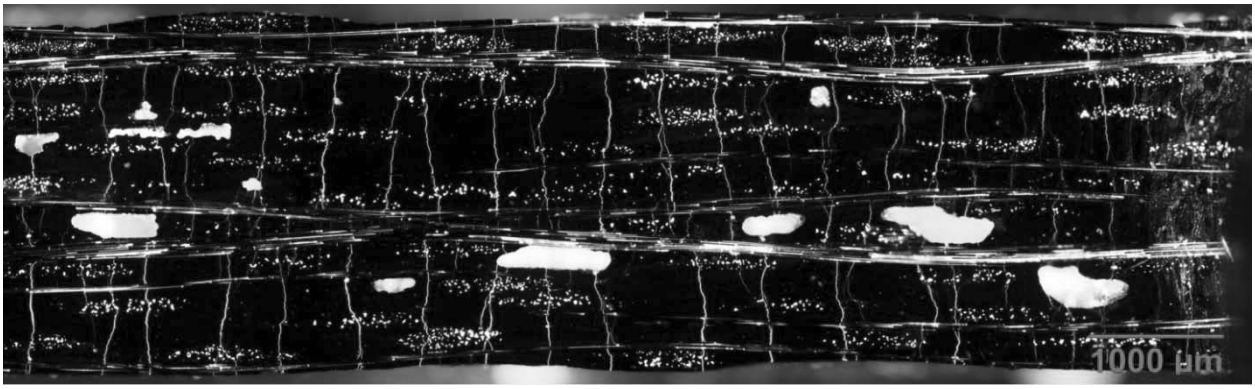

Figure 48: Image of Hi-Nicalon^{TM}/BN/SMI-SiC with UV-dye penetrant under load [50]

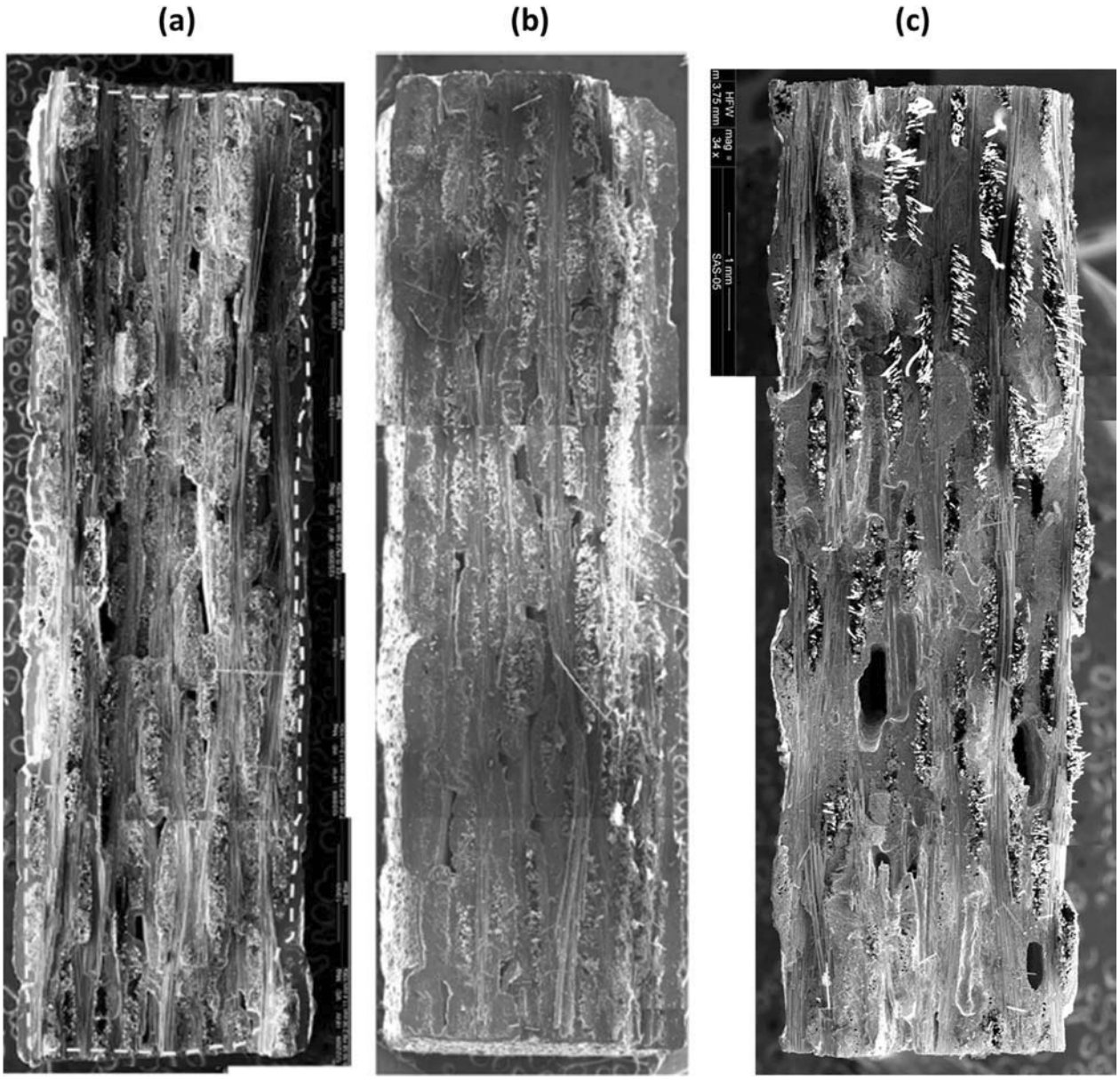

Figure 49: Comparison of specimens tested at 1200°C in air at 1.0 Hz. (a) CVI material tested by Christensen; (b) CVI material with oxidation inhibited matrix tested by Delapasse; (c) current SMI-SiC material with larger voids than those in the previously tested materials

VI. Conclusions and Recommendation

6.1 Conclusions

The tensile stress-strain behavior of Hi-Nicalon™/BN/SMI-SiC composite was investigated and the tensile properties measured at 1200°C. The UTS was 239 MPa, the elastic modulus, 217 GPa, and the failure strain, 0.41%. The proportional limit was 135 MPa (~56% UTS).

Tension-tension fatigue behavior of the Hi-Nicalon™/BN/SMI-SiC composite was studied at a loading frequency of 1.0 Hz at 1200°C in air and in steam. Fatigue stress levels ranged from 100 to 160 MPa. Fatigue run-out was achieved at 120 MPa (~50% UTS) in air and at 110 MPa (~46% UTS) in steam. The presence of steam was slightly detrimental to fatigue performance at this temperature. At stresses above the fatigue limit, the specimens exhibited subcritical crack growth behavior due to the observed distribution of large voids within the composite matrix. As the maximum stress was increased from 120 MPa to 130 MPa in air, the cyclic life was reduced by nearly two orders of magnitude. In contrast, further increasing the maximum stress from 130 MPa to 140 MPa and then to 160 MPa does not cause orders of magnitude reductions in cyclic life. In air, the cyclic crack growth threshold stress was determined to be 120 and 130 MPa. In steam, the threshold fatigue stress was determined to be between 110 and 120 MPa. Above the threshold stress level, the void concentration controls the fatigue life of the material. Compared to prior testing performed under the same environmental conditions, the fatigue life of the Hi-Nicalon™/BN/SMI-SiC composite specimens was generally longer than the Hi-Nicalon™/BN/CVI-SiC composite, but underperformed the Hi-Nicalon™/SiC-B_4C material.

Prior fatigue in air reduced the retained tensile strength of the composite by ~3%. The retained stiffness was reduced by ~35%. In contrast, prior fatigue in steam had a more marked

effect on retained properties. Prior fatigue in steam reduced the tensile strength by ~10-18% and the stiffness, by ~10-60%. The specimens tested in air showed more strain accumulation than the specimens tested in steam.

For specimens that achieved run-out (N_f > 200,000 cycles), micrographs of the fracture surfaces showed little to no signs of oxidation on the interior of the specimen. For specimens that failed before reaching run-out, micrographs of the specimen fracture surfaces revealed distinct oxidized and non-oxidized regions. The signs of oxidation were more pronounced on the fracture surfaces of specimens tested in steam. The results indicate that above a threshold stress for crack initiation, an oxidation-assisted unbridged crack grew through the specimen until the remaining ligament of material failed under the applied stress. Below the threshold stress, a crack did not grow, and the resulting fracture surface was exposed to the furnace environment only after specimen failure in the post-fatigue tension test. In steam, the oxidation progressed more aggressively, contributing to the shorter fatigue life of the specimens tested in steam.

6.2 Recommendations

Very few specimens were available for testing. In order to obtain greater confidence in the data and better define the crack growth stress threshold, more specimens should be tested in tension to failure and in tension-tension fatigue under the same temperature and environmental conditions. Additionally, tests evaluating the rate of oxidation and crack growth rate should be conducted to better understand the oxidation-assisted unbridged crack growth phenomenon in this particular composite.

Appendix A – Optical Micrographs of Specimen Fracture Surfaces.

The figures below are optical micrographs of specimens tested during the present study. Images are included here if they were not shown in the manuscript. The specimens tested in air are shown first, followed by the specimens tested in steam. Specimen width is 8mm, and thickness is 2.7mm.

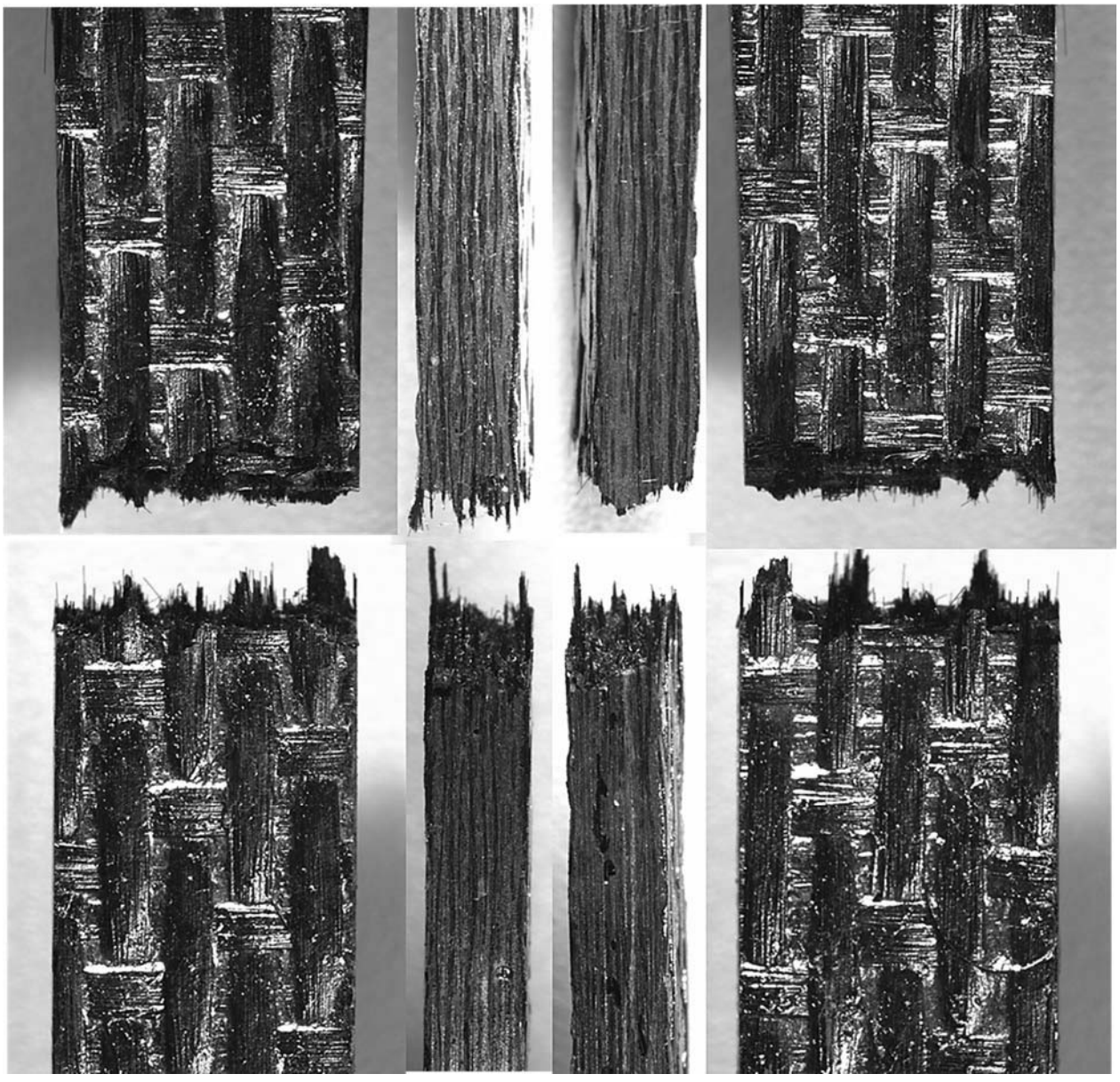

Figure A1: Top and bottom fracture surfaces of specimen 16-059, tested in tension to failure at 1200°C in air.

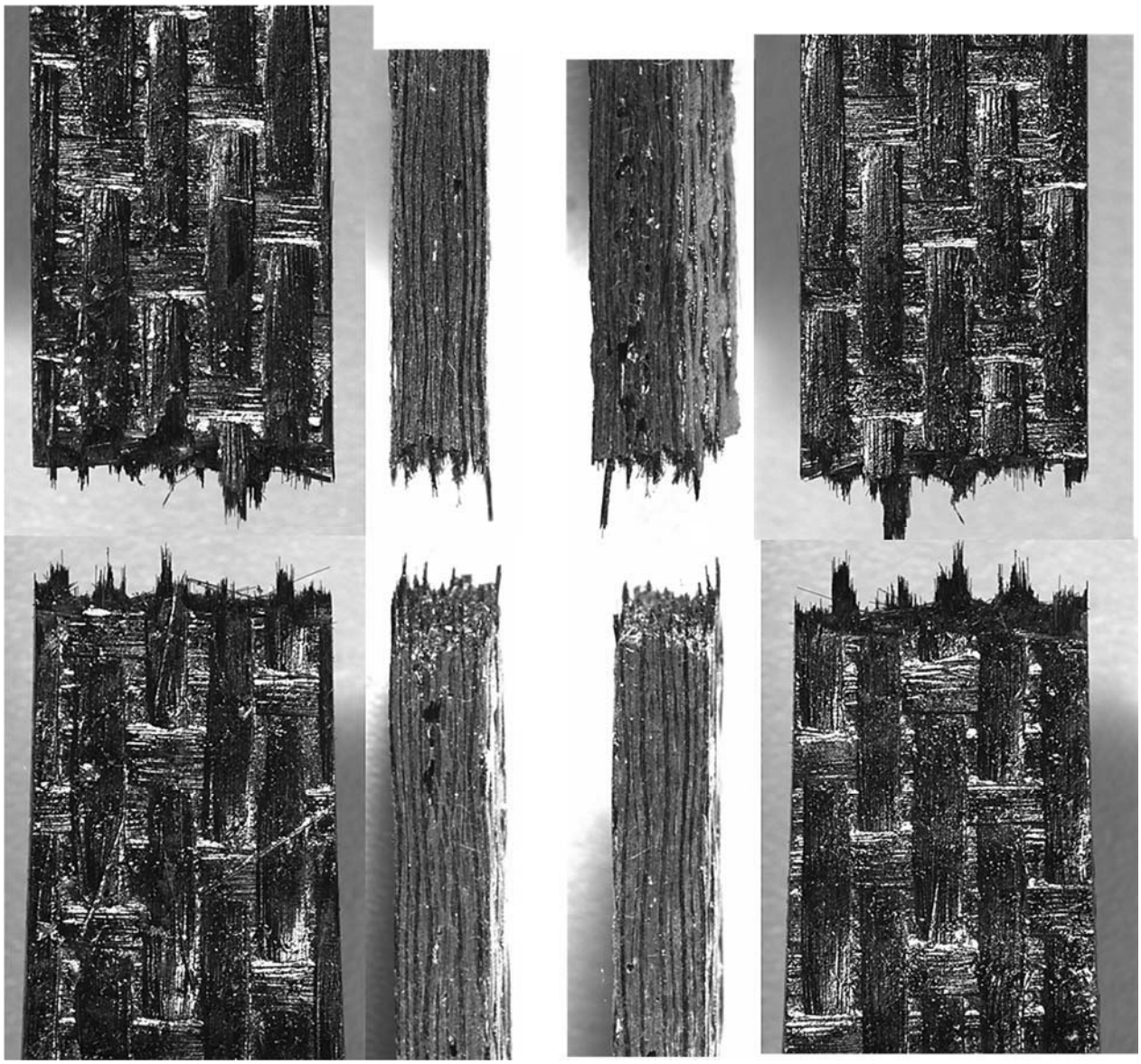

Figure A2: Top and bottom fracture surfaces of specimen 16-031, tested in fatigue at 1200°C in air. σ_{max} = 120 MPa, N_f>200,000

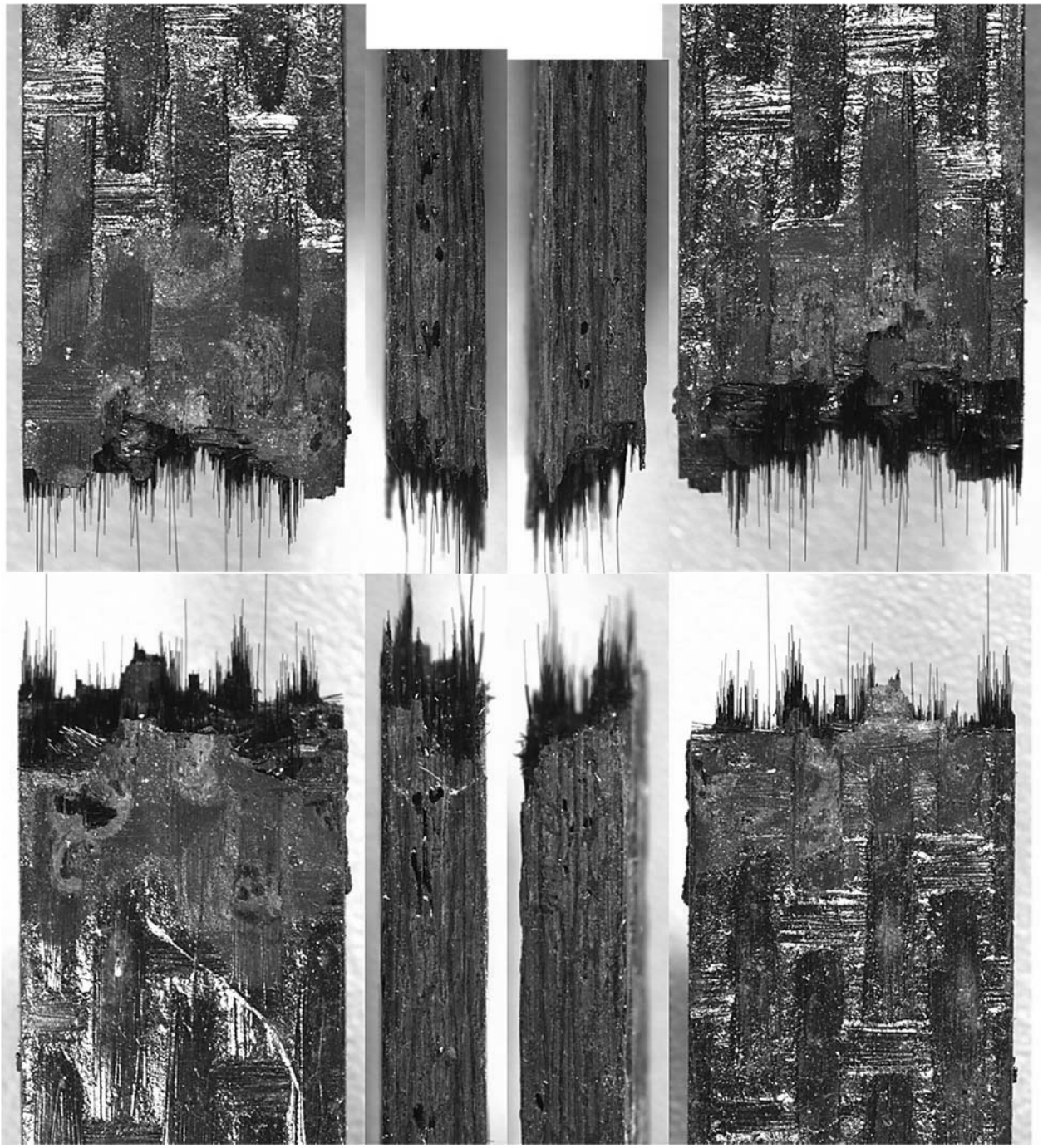

Figure A3: Top and bottom fracture surfaces of specimen 16-044, tested in fatigue to failure at 1200°C in air. σmax = 130 MPa, Nf=4,506. Specimen was used as the temperature calibrator prior to fatigue testing

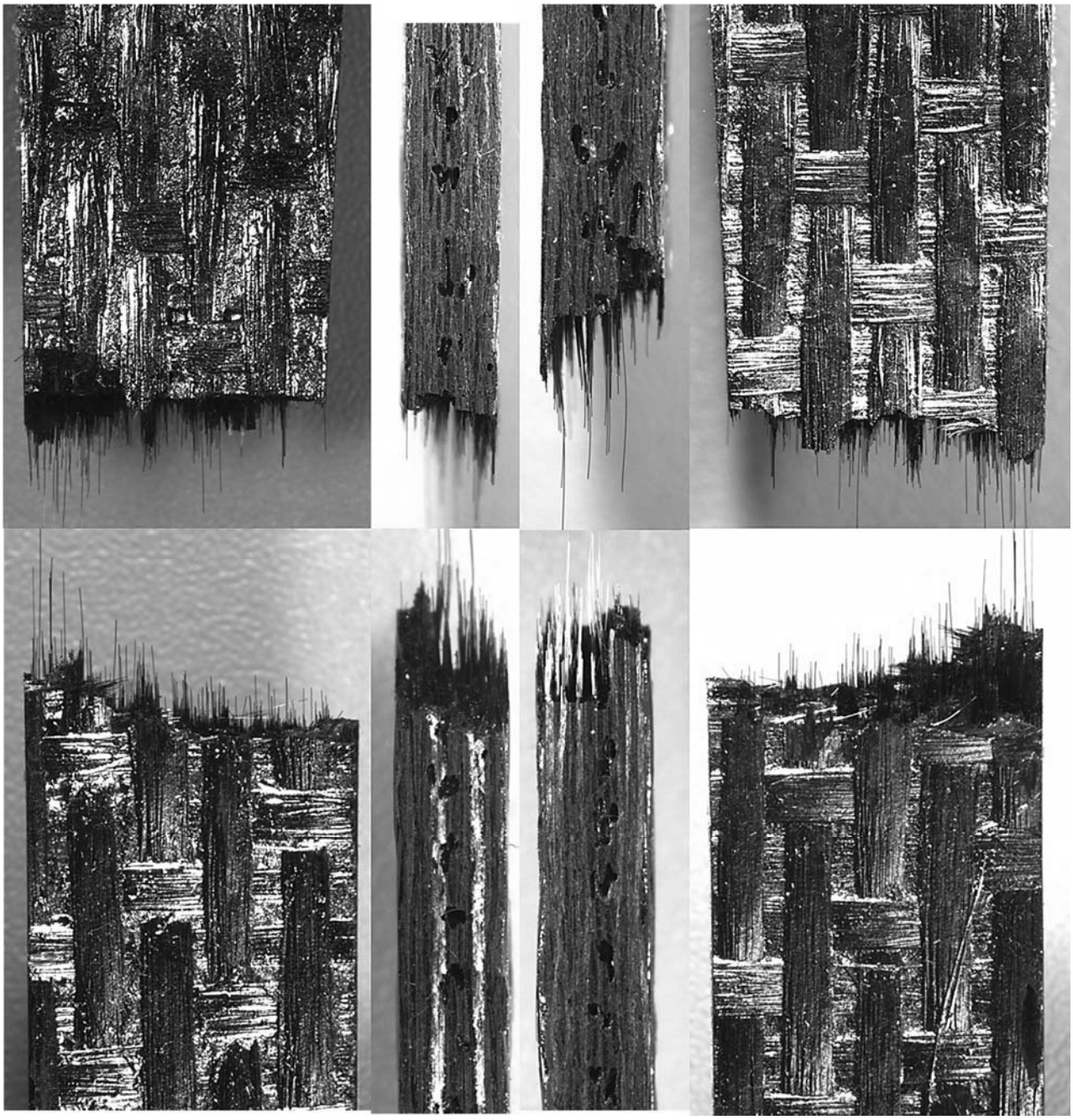

Figure A4: Top and bottom fracture surfaces of specimen 16-045, tested in fatigue to failure at 1200°C in air. σ_{max} = 140 MPa, N_f=2,200

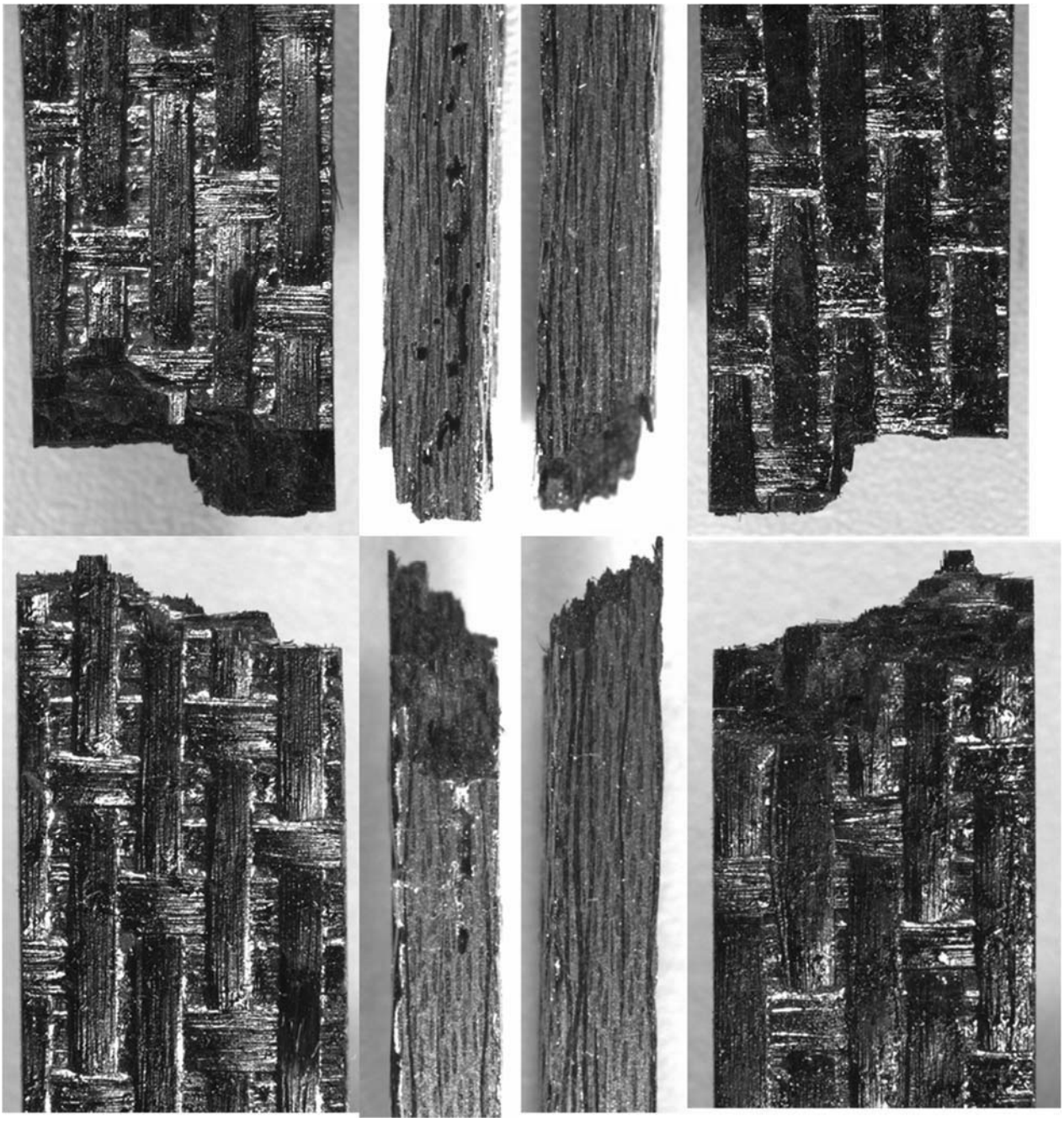

Figure A5: Top and bottom fracture surfaces of specimen 16-057, tested in fatigue to failure at 1200°C in air. σ_{max} = 160 MPa, N_f=1,220.

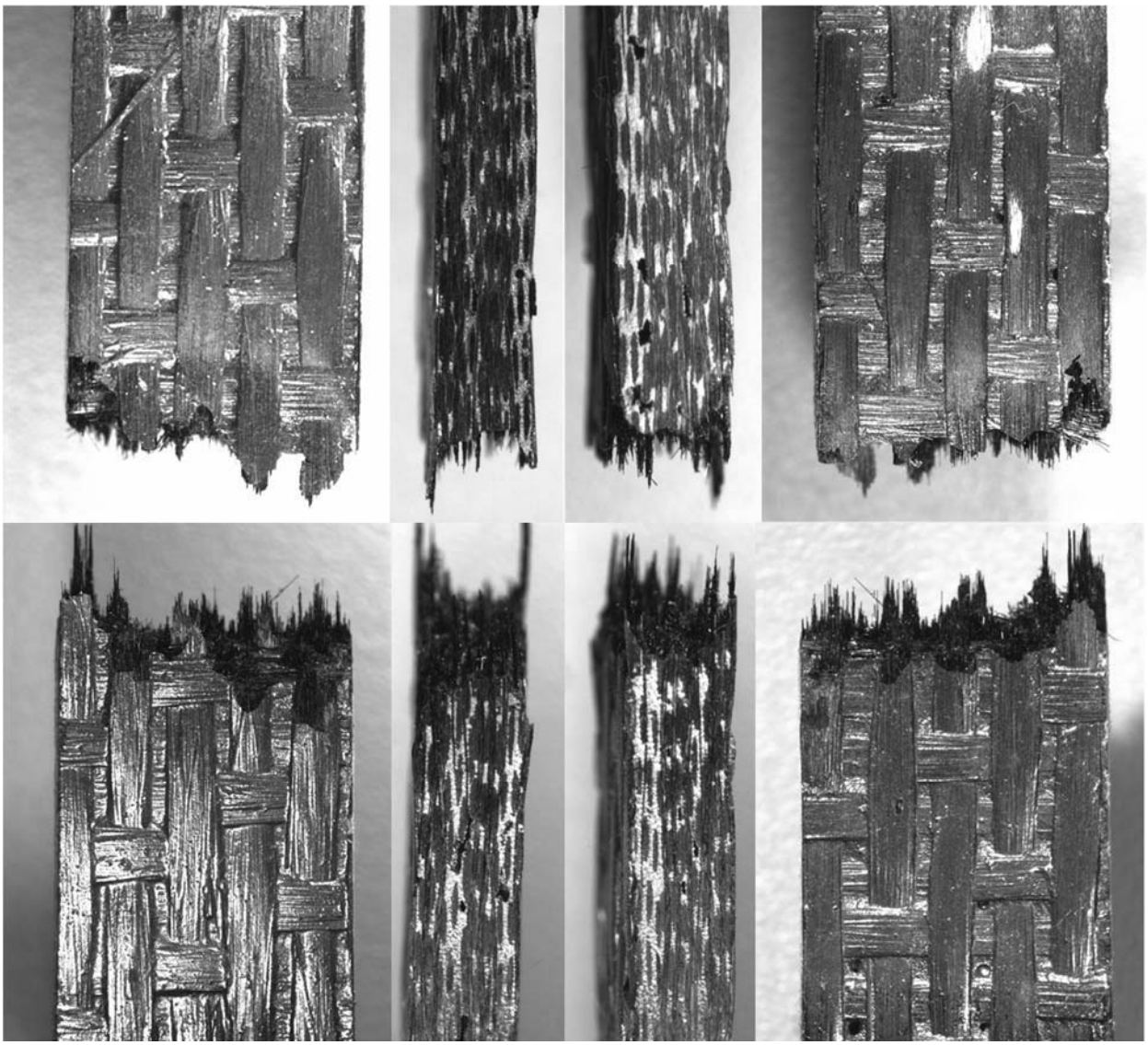

Figure A6: Top and bottom fracture surfaces of specimen 16-033, tested in fatigue at 1200°C in steam. σ_{max} = 100 MPa, N_f>200,000.

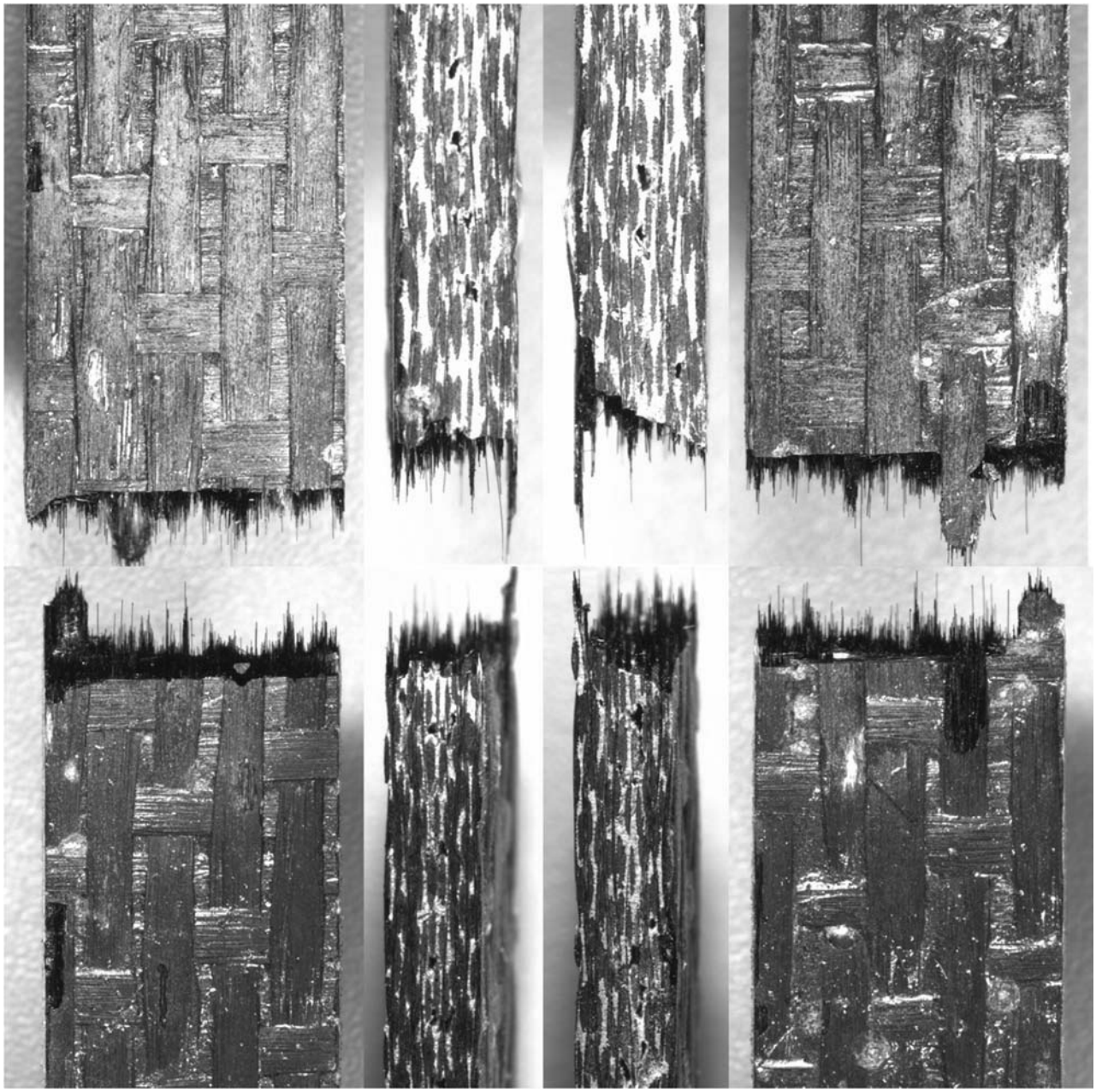

Figure A7: Top and bottom fracture surfaces of specimen 16-046, tested in fatigue at 1200°C in steam. σ_{max} = 110 MPa, N_f>200,000.

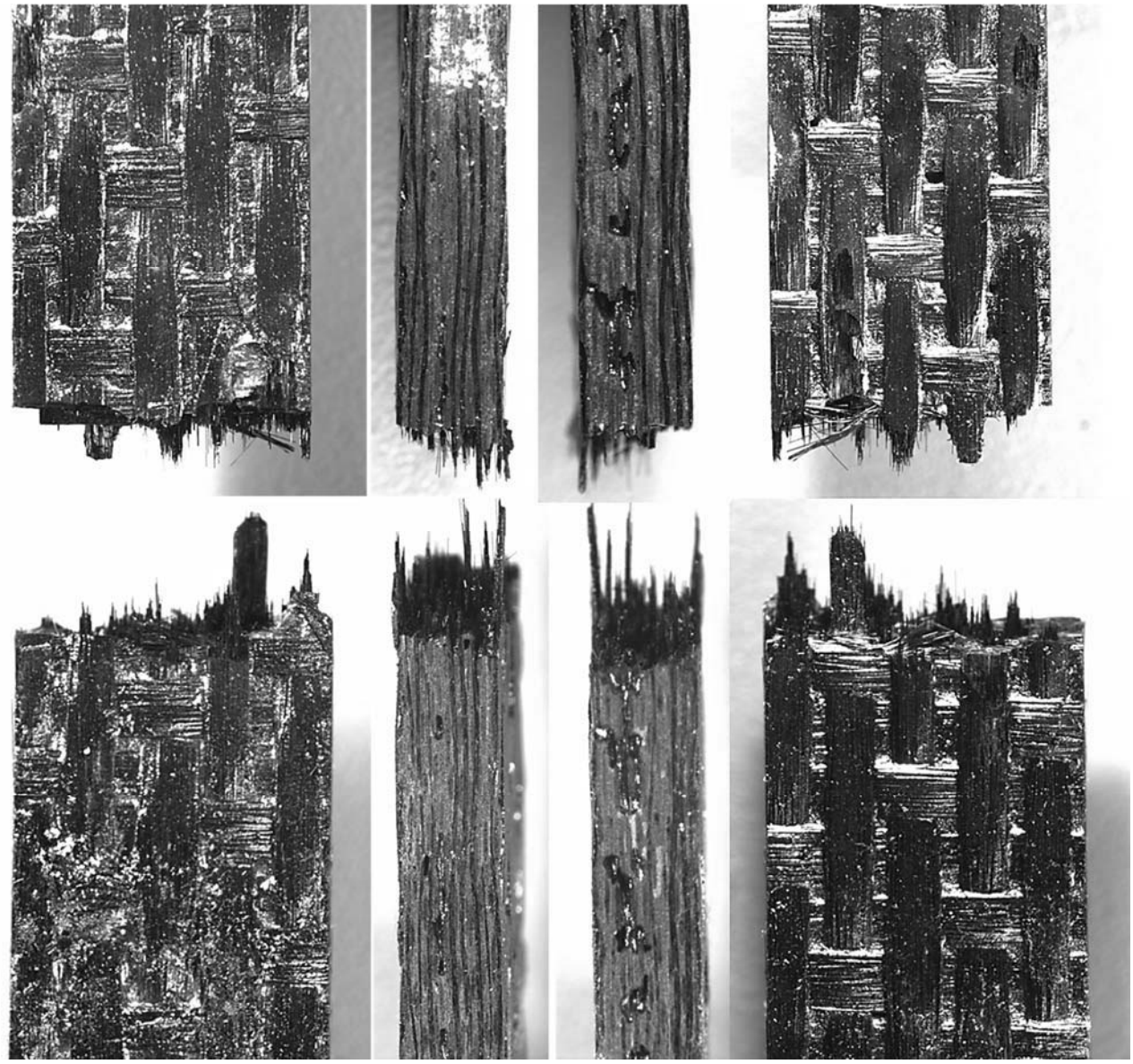

Figure A8: Top and bottom fracture surfaces of specimen 16-032 tested in fatigue to failure at 1200°C in steam. σ_{max} = 120 MPa, N_f=5,311.

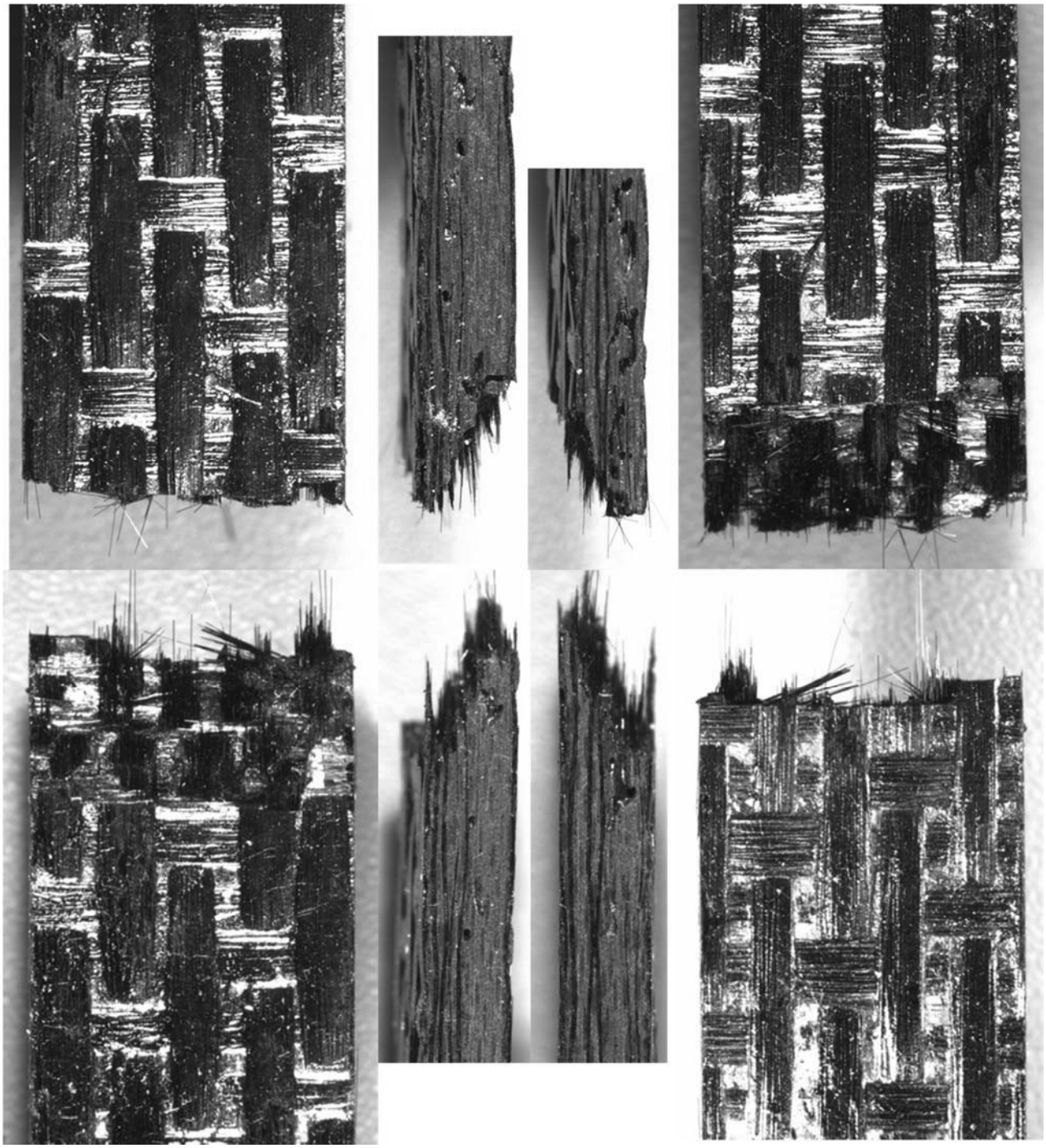

Figure A9: Top and bottom fracture surfaces of specimen 16-058, tested in fatigue to failure at 1200°C in steam. σ_{max} = 130 MPa, N_f=3,201.

Appendix B – SEM Micrographs of Specimen Fracture Surfaces

All SEM micrographs taken over the course of this study are included here if they did not appear in the manuscript. Micrographs of specimens tested in air are shown first, followed by micrographs of the specimens tested in steam.

Fracture surface of specimen 16-059, tested in tension to failure at 1200°C in air

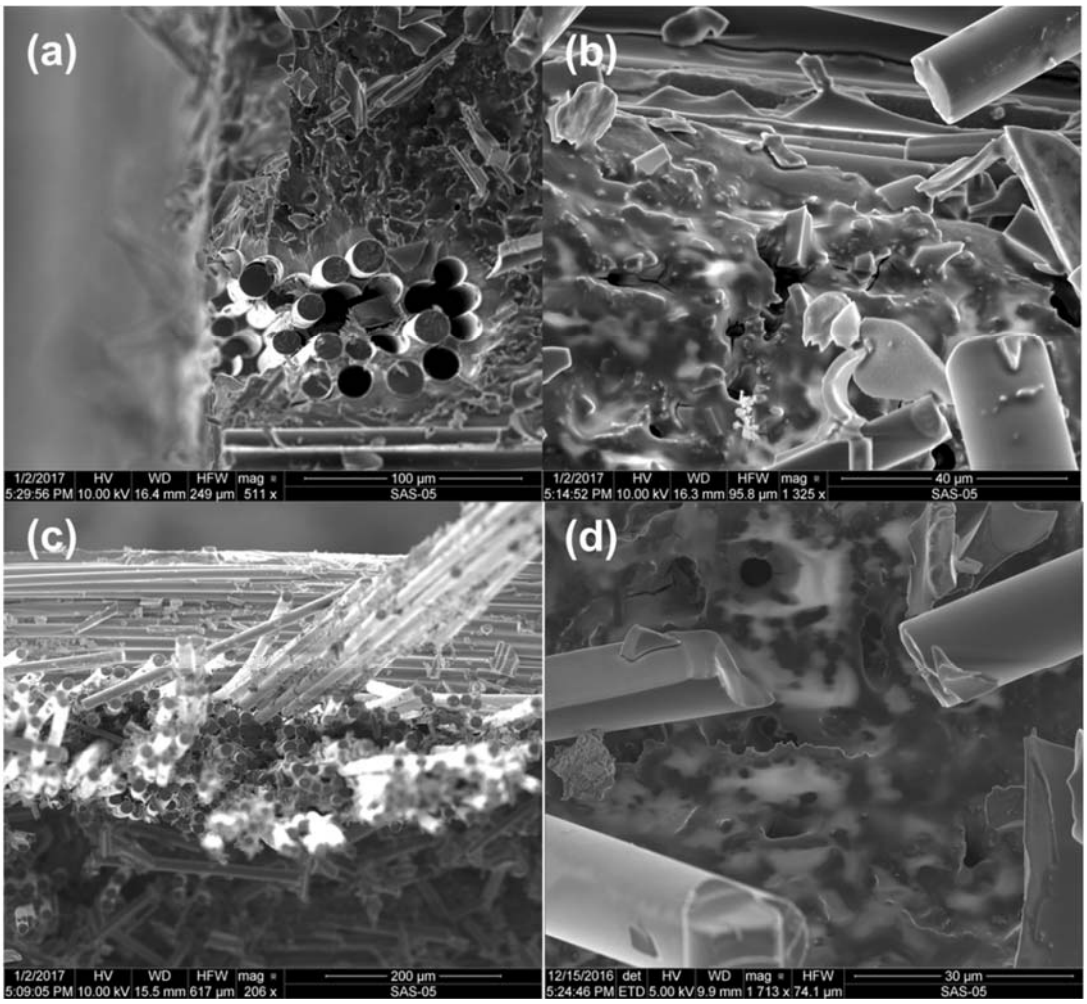

Figure A10: Higher-magnification images of the fracture surface of the specimen tested in tension to failure at 1200°C in air showing fiber pull-out (a,c) and non-oxidized matrix regions (b,d)

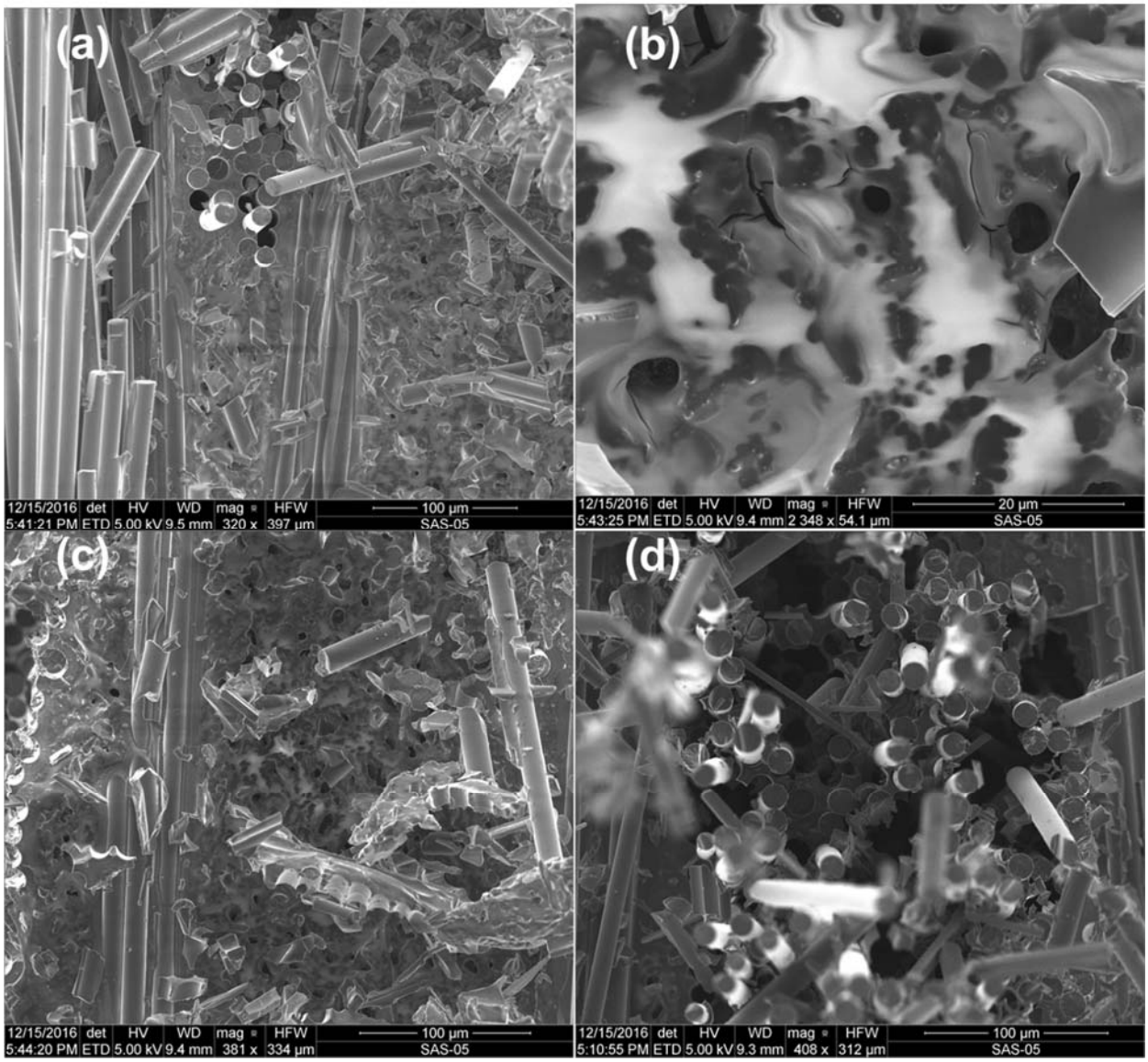

Figure A11: Higher-magnification images of the fracture surface of the specimen tested in tension to failure at 1200°C in air showing fiber pull-out (a,d) and non-oxidized matrix regions (b,c)

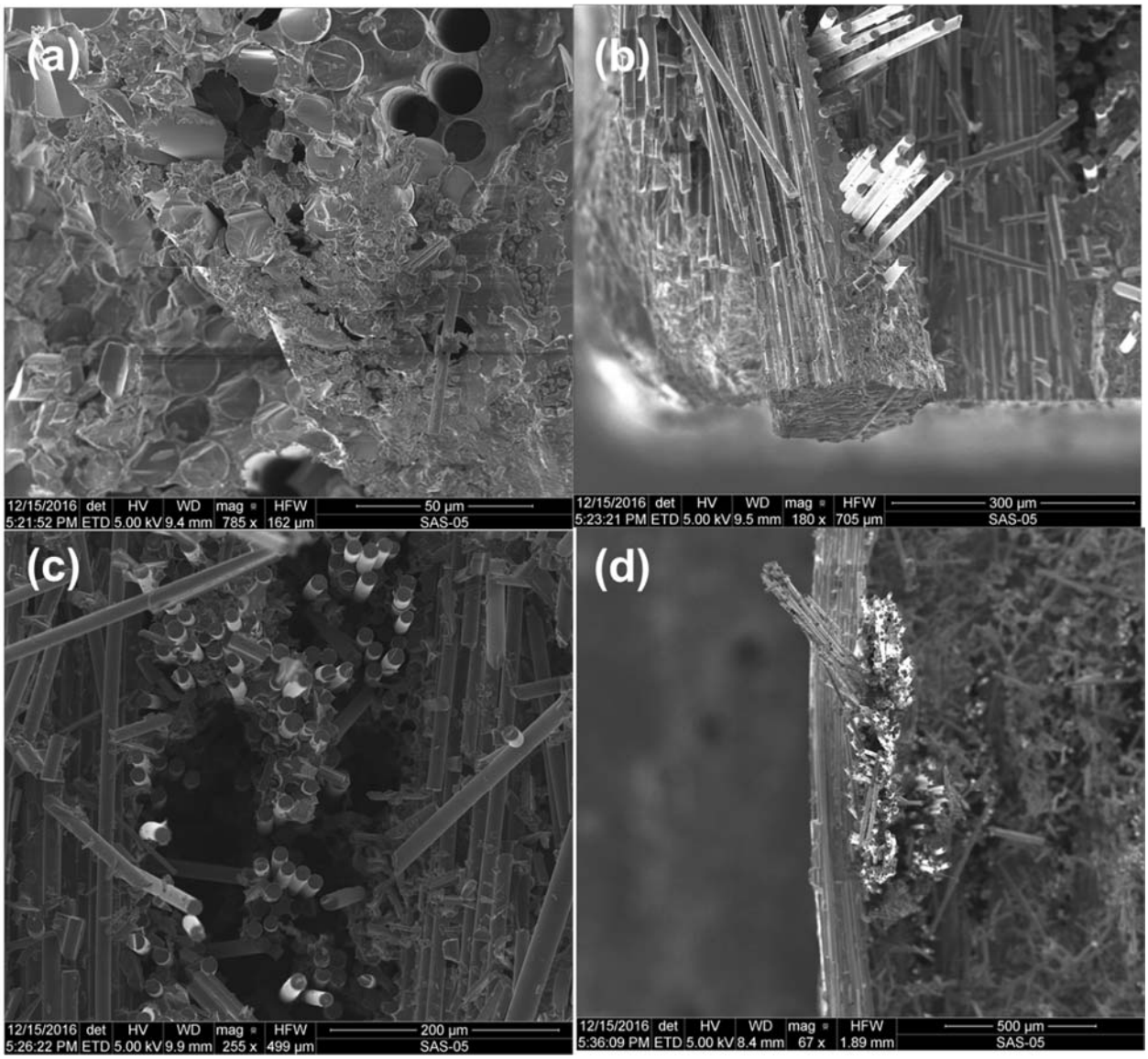

Figure A12: Higher-magnification images of the fracture surface of the specimen tested in tension to failure at 1200°C in air showing (a) fiber pull-out; (b) fused fiber bundle; (c) transverse fiber pull-out; (d) fiber tow pull-out

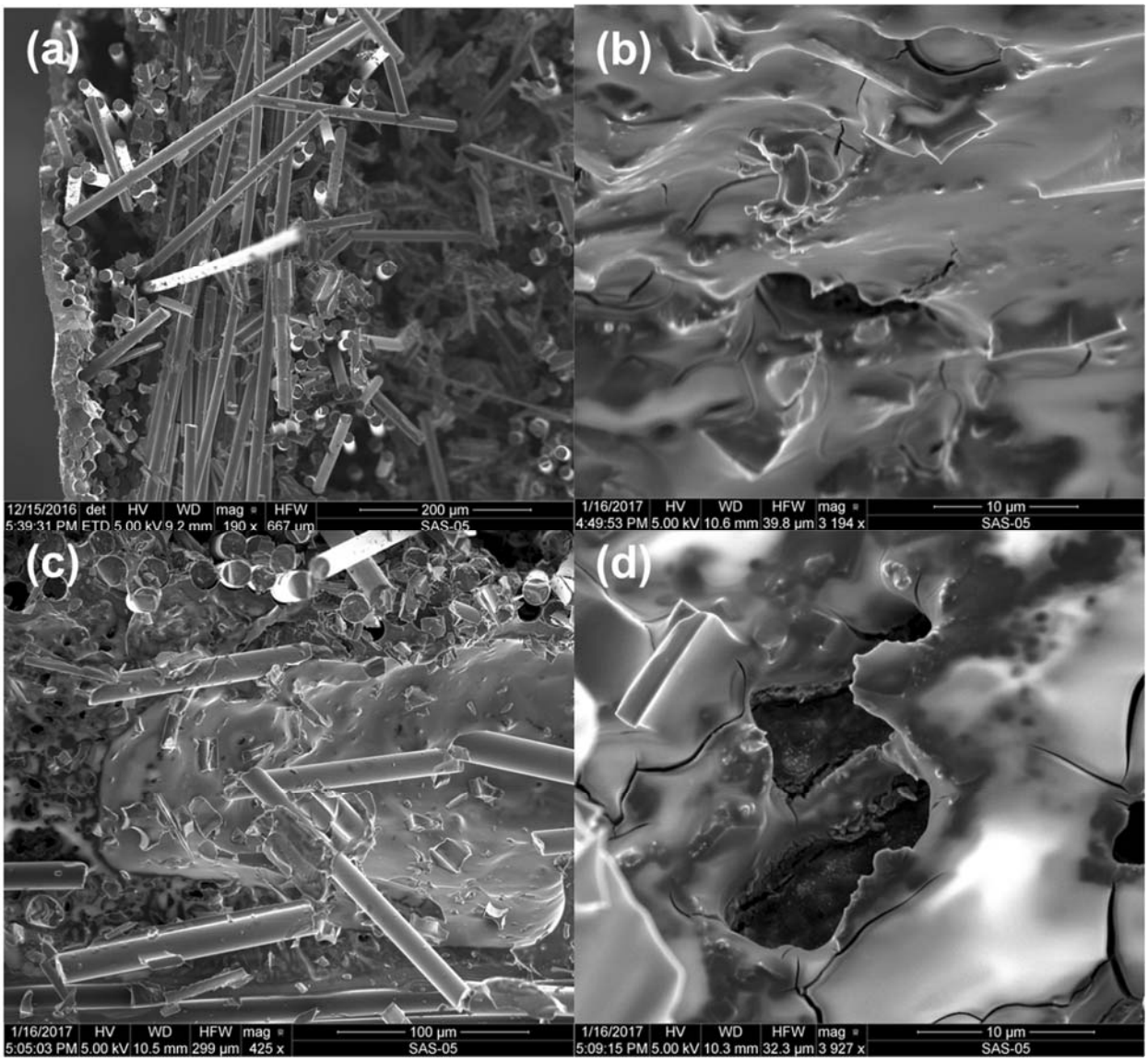

Figure A13: Higher-magnification images of the fracture surface of the specimen tested in tension to failure at 1200°C in air showing (a) fiber pull-out; (b) non-oxidized matrix appearance; (c) fiber pull-out surrounding a void surface; (d) non-oxidized matrix appearance

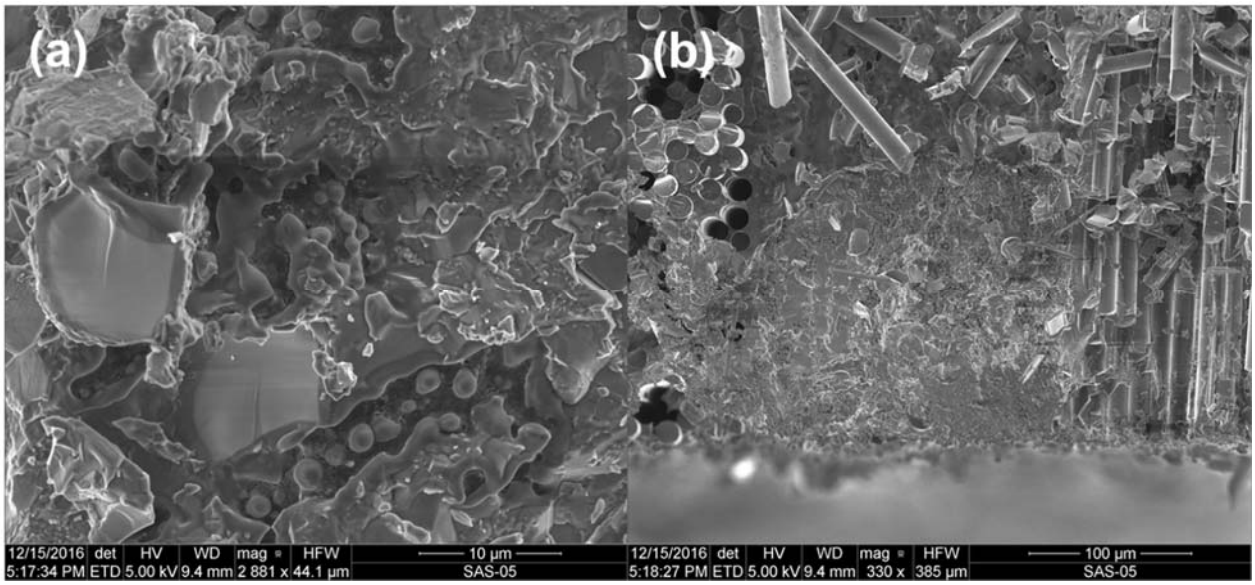

Figure A14: Higher-magnification images of the fracture surface of the specimen tested in tension to failure at 1200°C in air showing non-oxidized matrix regions on the edge of the fracture surface

SEM micrographs of Specimen 16-031, tested in tension-tension fatigue at 1200°C in air.

σ_{max} = 120 MPa, N_f > 200,000

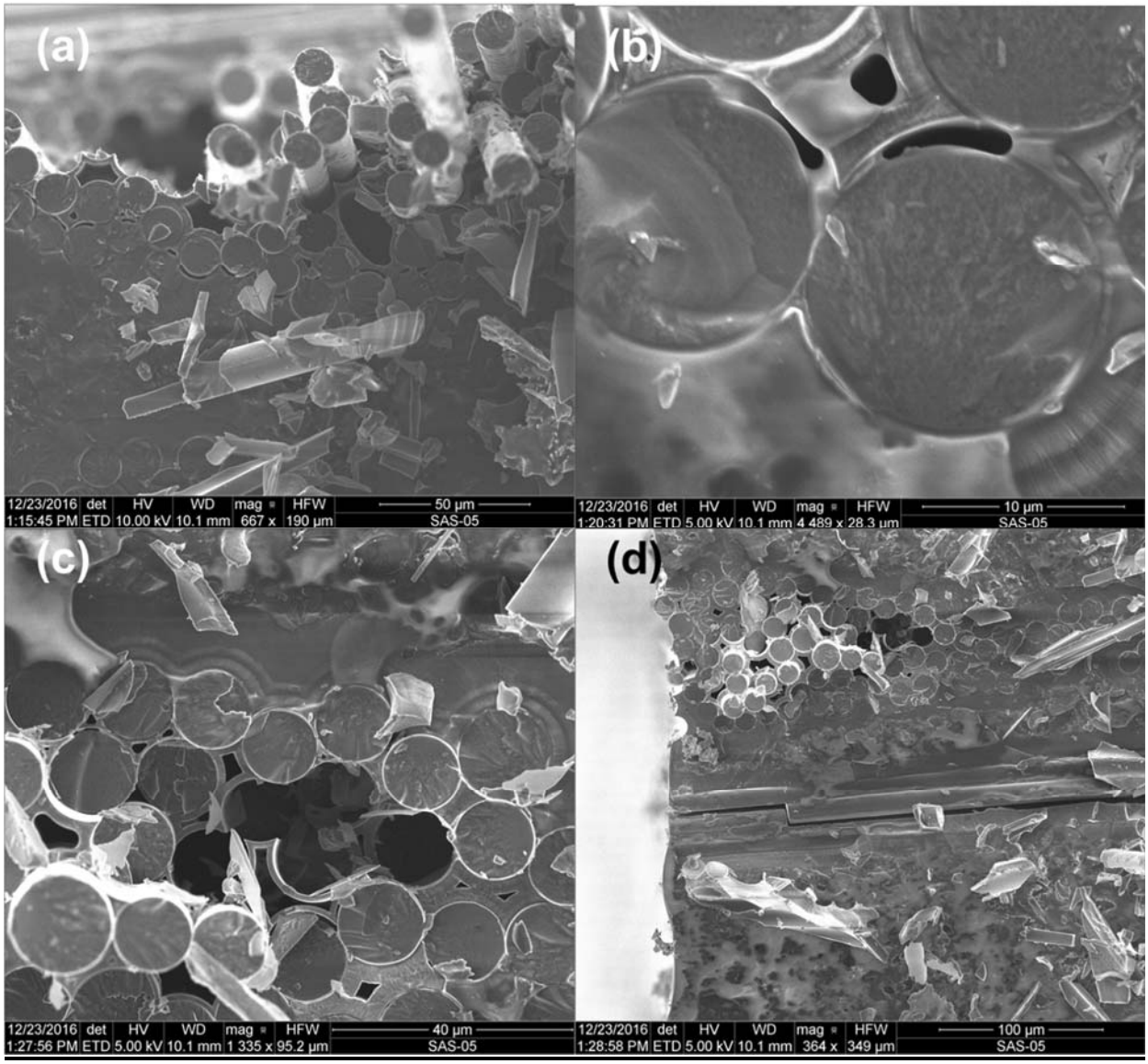

Figure A15: Higher-magnification images of the fracture surface of specimen 16-031 tested in fatigue at 1200°C in air showing (a) some evidence of oxidation despite evidence of pull-out; (b,c) fiber-to-fiber bonding; (d) planar fracture

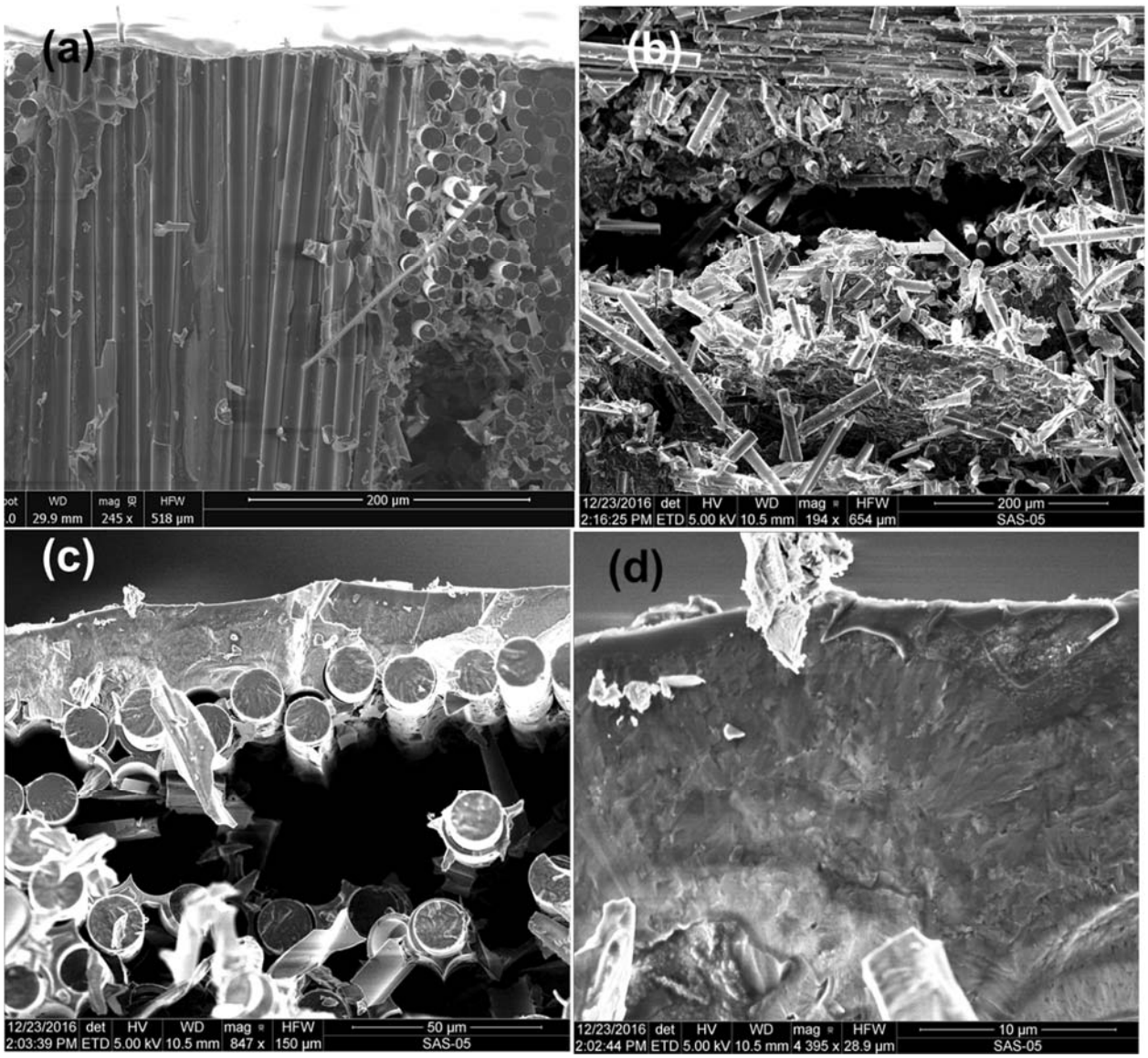

Figure A16: Higher-magnification images of the fracture surface of specimen 16-031 tested in fatigue at 1200°C in air showing (a,b,c) non-oxidized surface features; (d) fractograph of CVI-SiC layer on exterior of non-oxidized fiber region

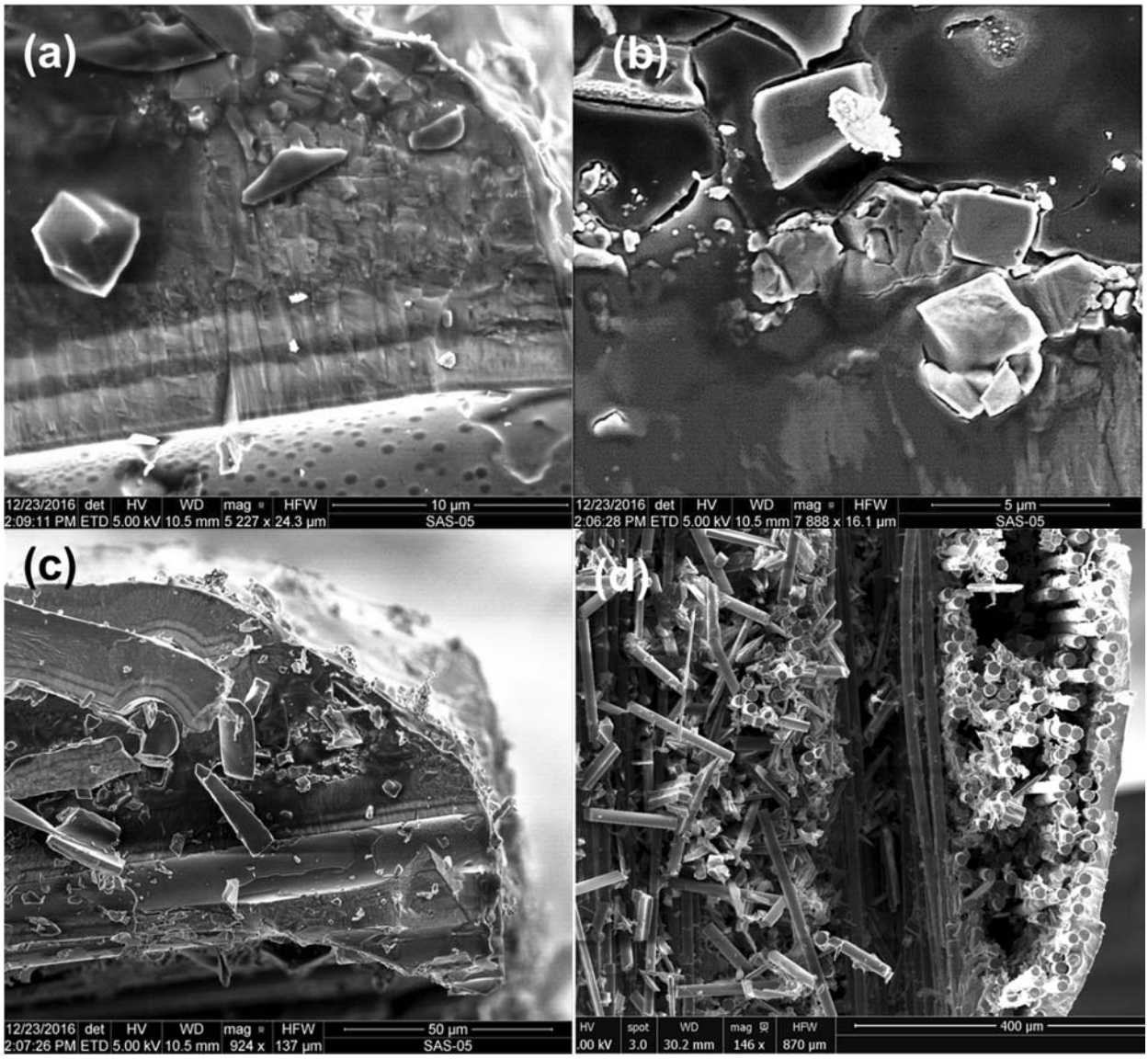

Figure A17: Higher-magnification images of the fracture surface of specimen 16-031 tested in fatigue at 1200°C in air showing (a) fractograph of CVI-SiC layer surrounding fiber; (b) fractograph of matrix in region between fiber tows; (c) failure of tow at edge of specimen; (d) transverse fibers adjacent to pull-out in exterior fiber tow

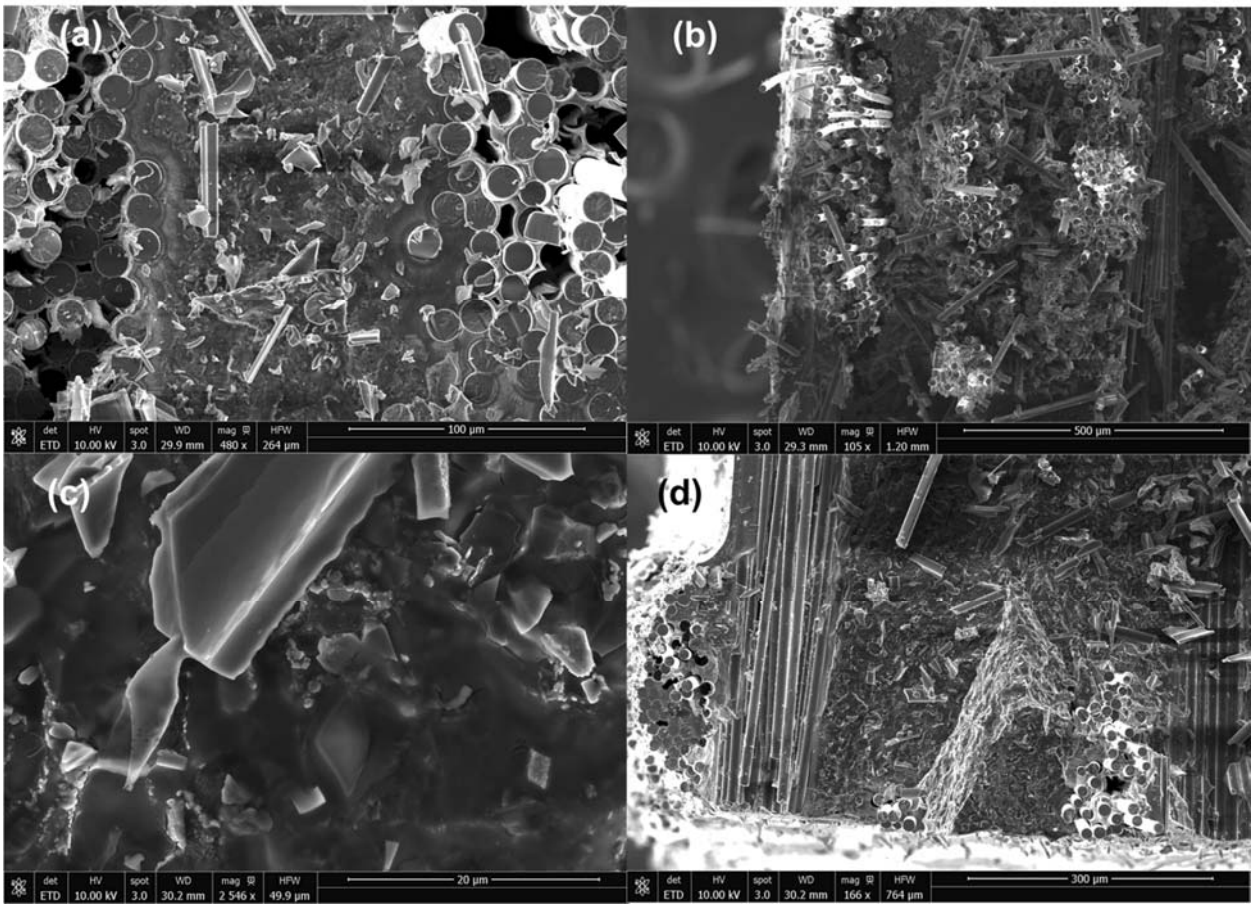

Figure A18: Higher-magnification images of the fracture surface of specimen 16-031 tested in fatigue at 1200°C in air showing (a) Signs of oxidation around fiber bundles; (b) fiber pull-out region; (c) non-oxidized matrix fractograph; (d) non-oxidized region

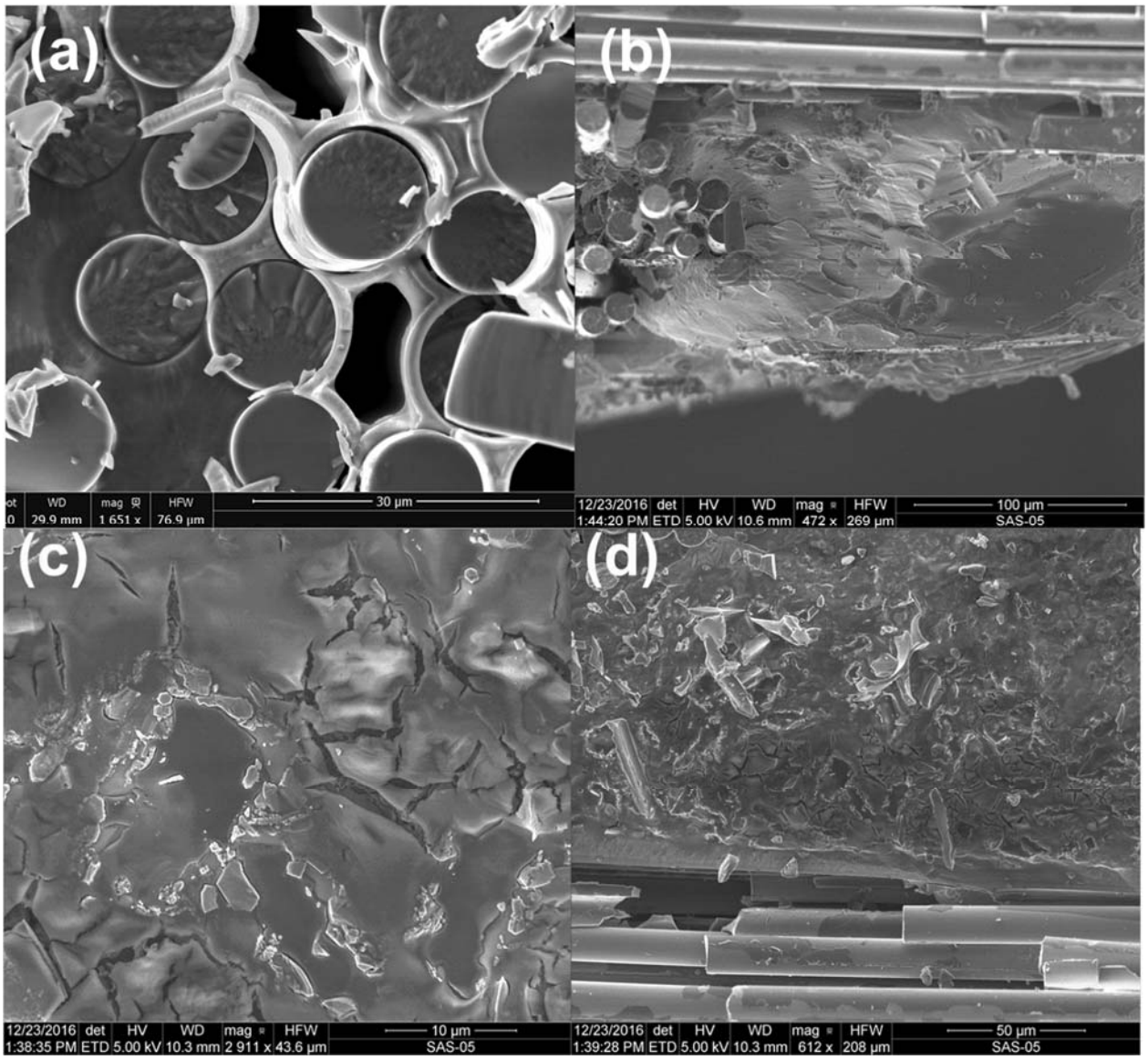

Figure A19: : Higher-magnification images of the fracture surface of specimen 16-031 tested in fatigue at 1200°C in air showing (a) non-oxidized fiber pull-out; (b) fracture surface of exterior oxidation buildup; (c) fractograph of matrix surface in non-oxidized region; (d) matrix material adjacent to transverse fiber bundle

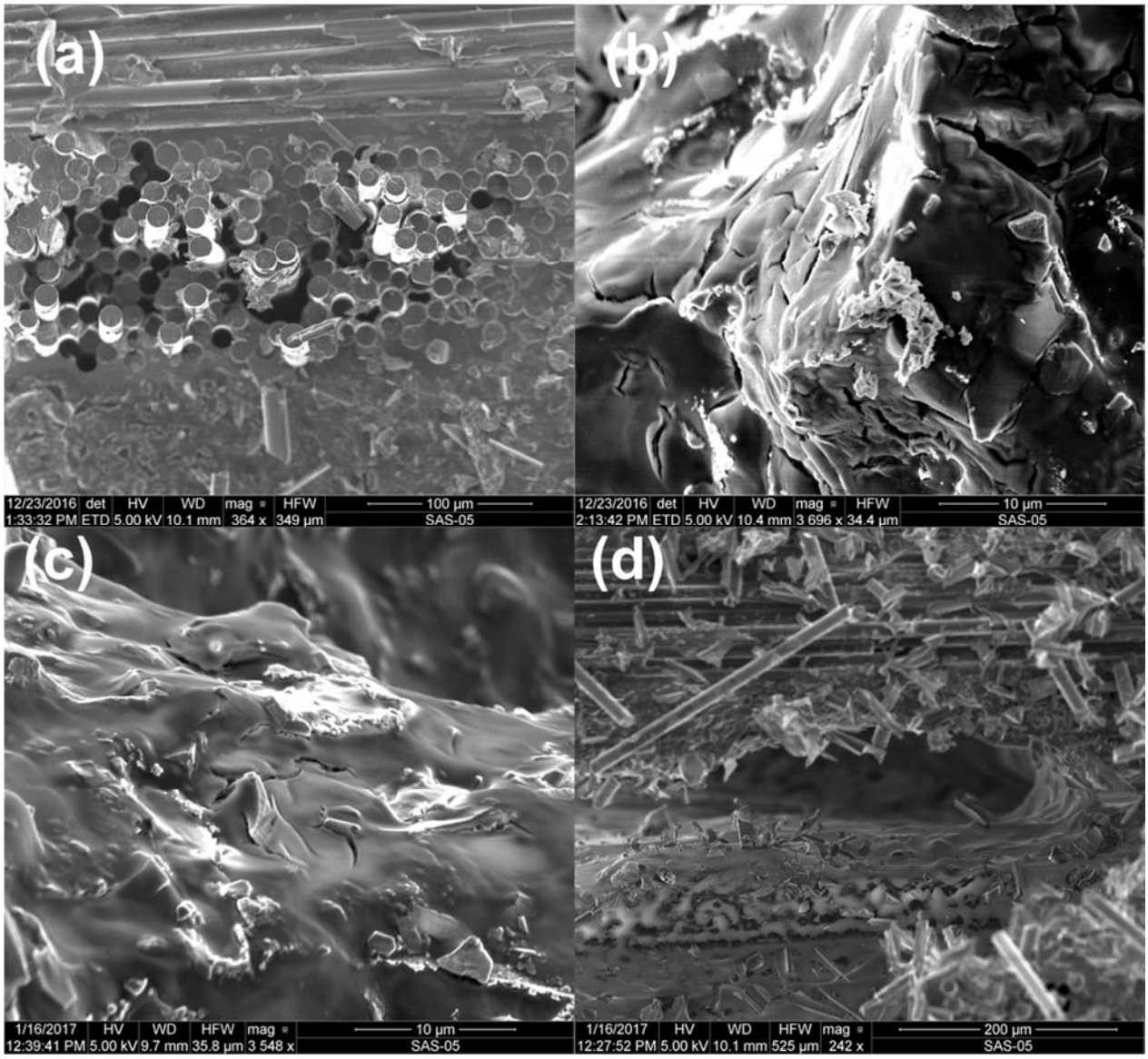

Figure A20: Higher-magnification images of the fracture surface of specimen 16-031 tested in fatigue at 1200°C in air showing (a) fiber pull-out with some oxidation surrounding the tow; (b,c) fractograph of matrix; (d) glassy phase surrounding void interior

Specimen 16-044, tested in tension-tension fatigue at 1200°C in air.

σ_{max} = 130 MPa, N_f=4,506

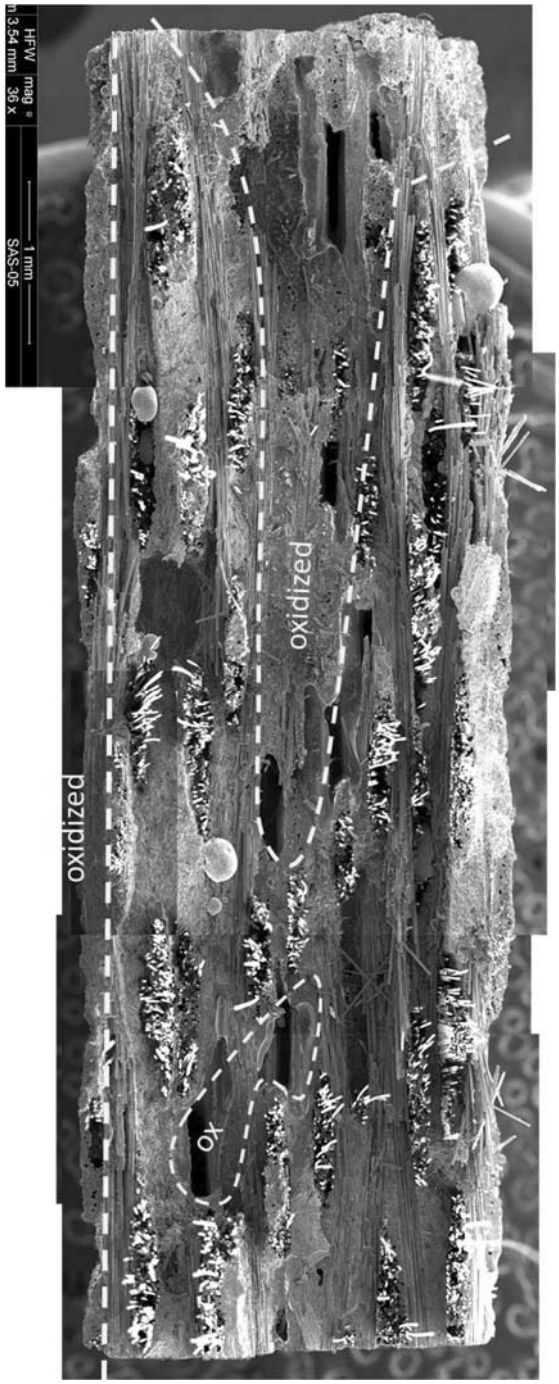

Figure A21: SEM micrograph of the fracture surface of the specimen tested in fatigue to failure at 1200°C in air. σ_{max} = 130 MPa, N_f=4,506

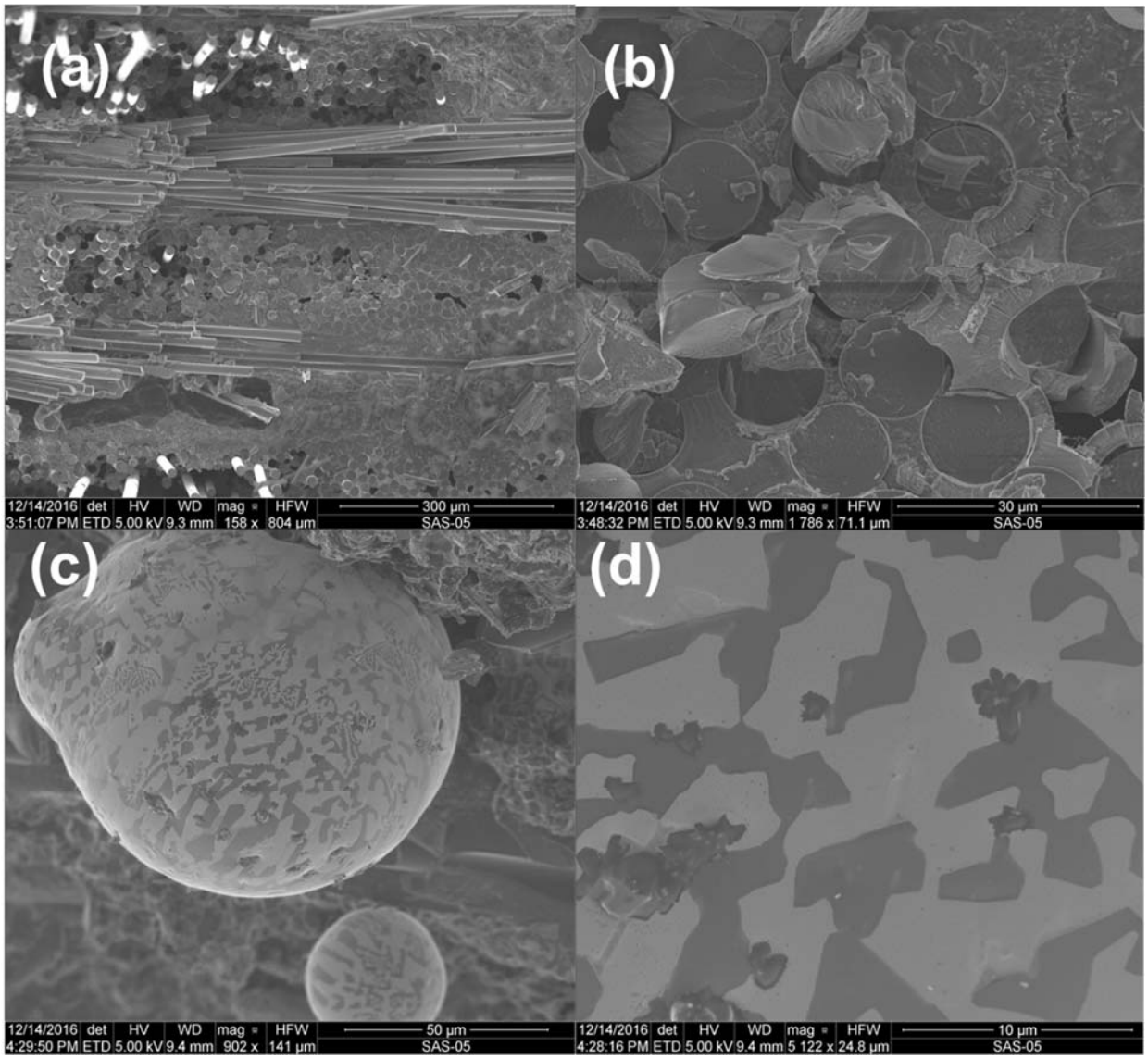

Figure A22: Higher-magnification images of the fracture surface of specimen 16-044 tested in fatigue at 1200°C in air showing (a) fracture plane through fiber bundle between transverse tows; (b) magnified view of fiber fracture in image (a); (c) eutectic mixture of platinum and silicon forming a spheroid; (d) magnified view of eutectic compound

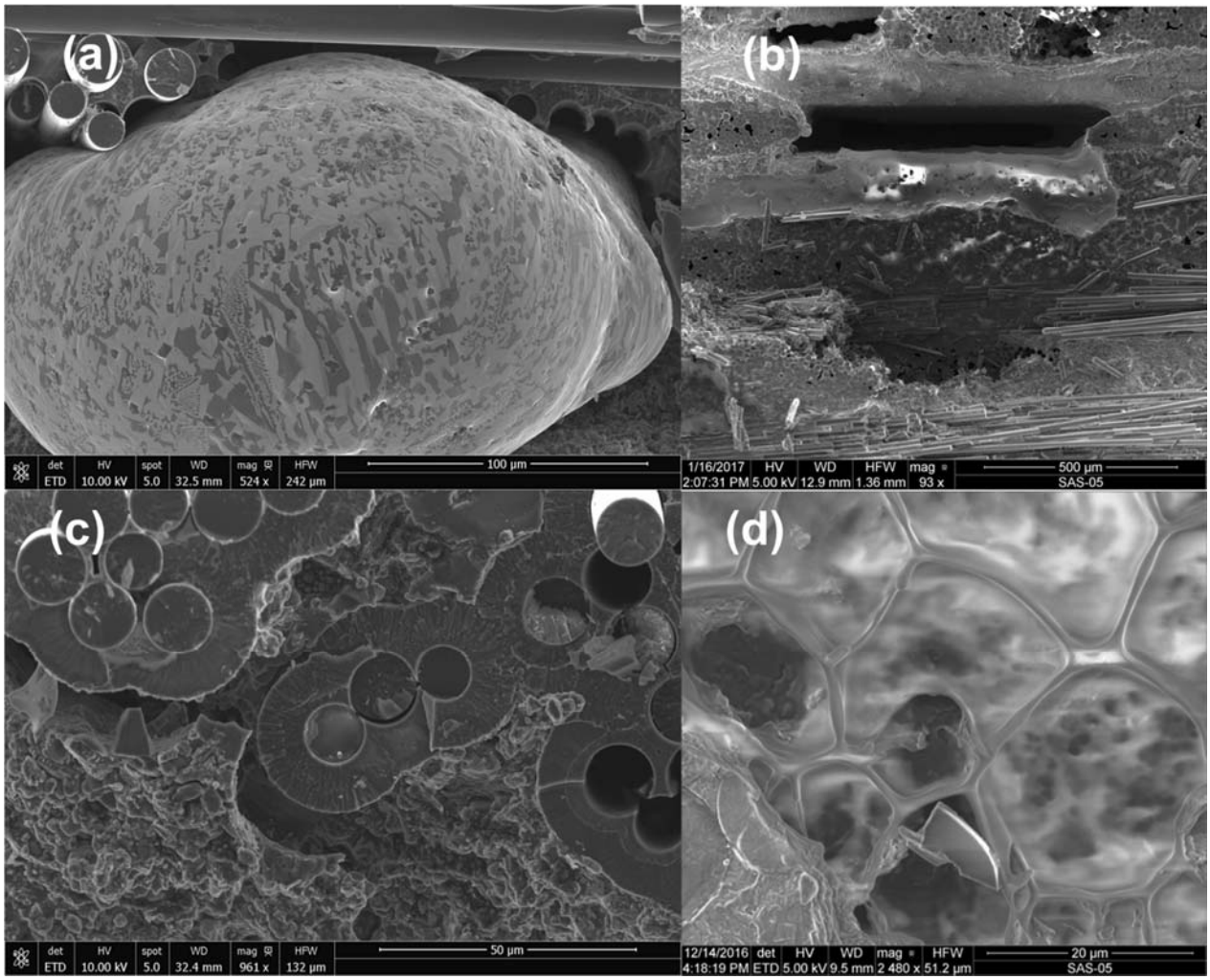

Figure A23: Higher-magnification images of the fracture surface of specimen 16-044 tested in fatigue at 1200°C in air showing (a) eutectic remnant of thermocouple bead; (b) void interior with surrounding glassy layer; (c) Possibly oxidized region; (d) glassy layer near void

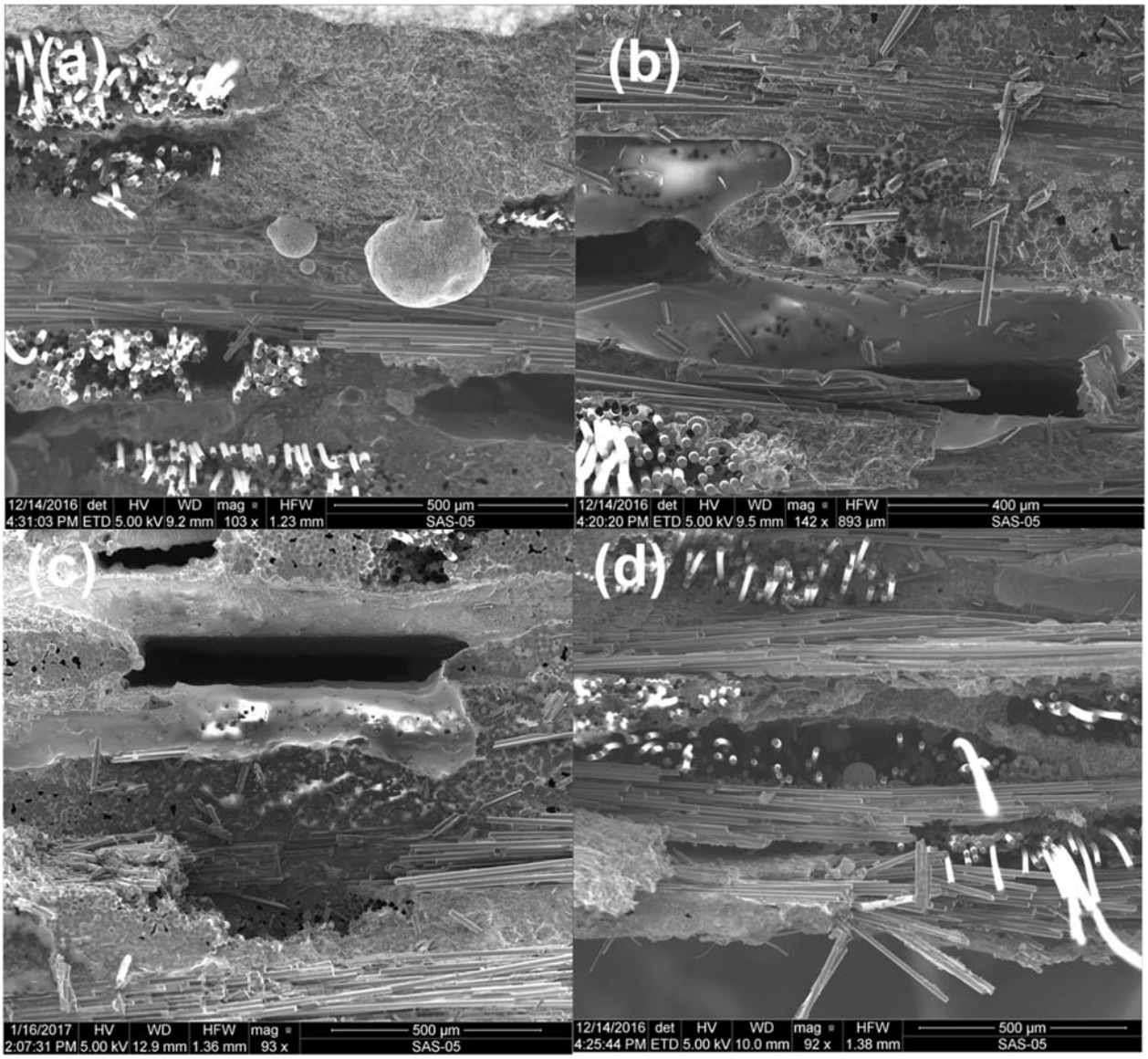

Figure A24: Higher-magnification images of the fracture surface of specimen 16-044 tested in fatigue at 1200°C in air showing (a) relative size of eutectic beads from thermocouple material; (b),(c) glassy layer near large void; (d) fiber pull-out region

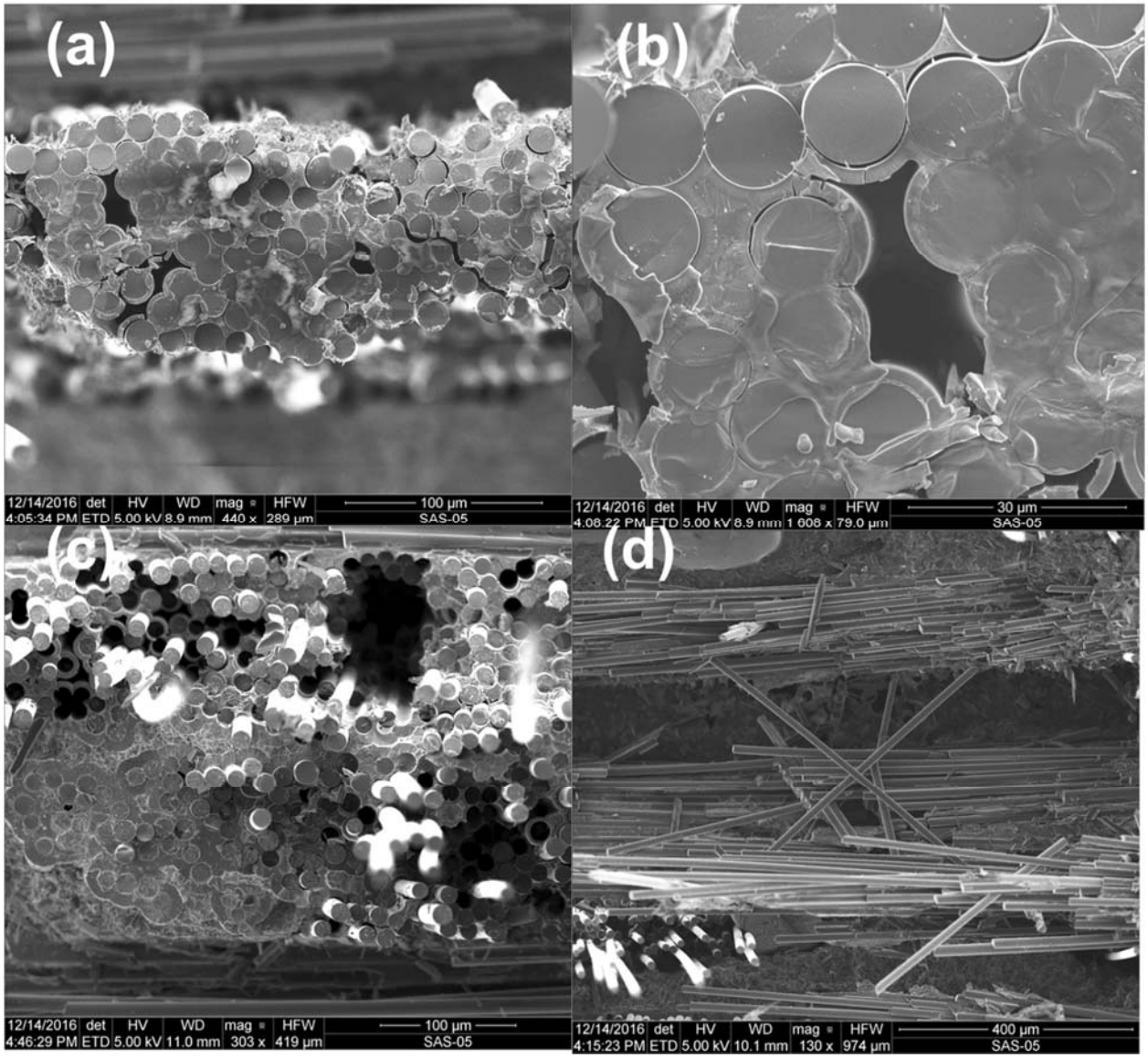

Figure A25: Higher-magnification images of the fracture surface of specimen 16-044 tested in fatigue at 1200°C in air showing (a) pulled-out fiber tow; (b) evidence of oxidation suggesting that fiber-to-fiber bonding can cause entire tows to pull-out; (c) fiber pull-out region; (d) transverse fiber pull-out

SEM micrographs of Specimen 16-045, tested in tension-tension fatigue at 1200°C in air.

σ_{max} = 140 MPa, N_f = 2,200

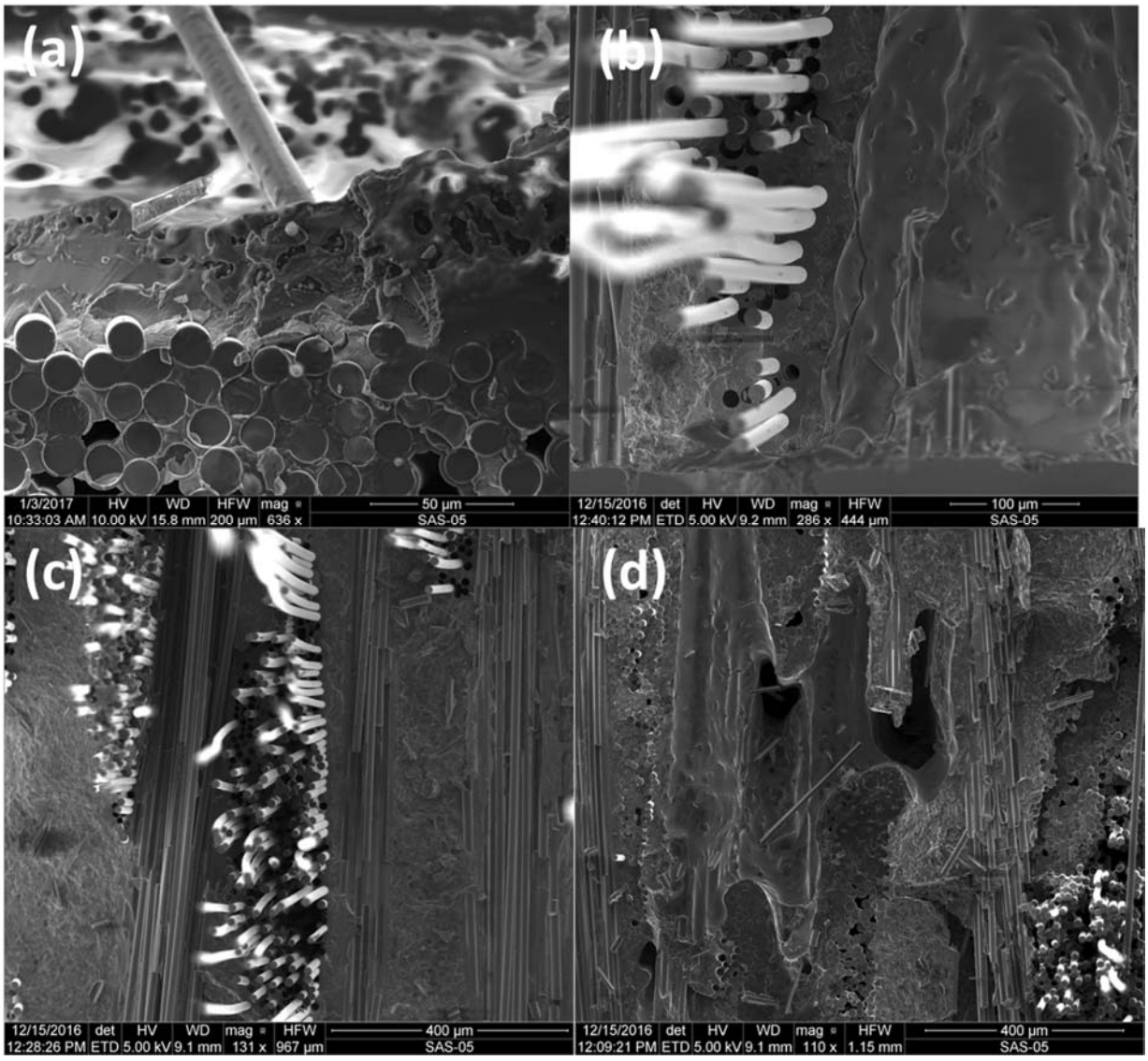

Figure A26: Higher-magnification images of the fracture surface of specimen 16-045 tested in fatigue at 1200°C in air showing (a) some evidence of oxidation of fibers next to a non-oxidized matrix region bordering a void; (b) fiber pull-out near a void; (c) fiber pull-out; (d) mixed oxide and non-oxide features surrounding large voids

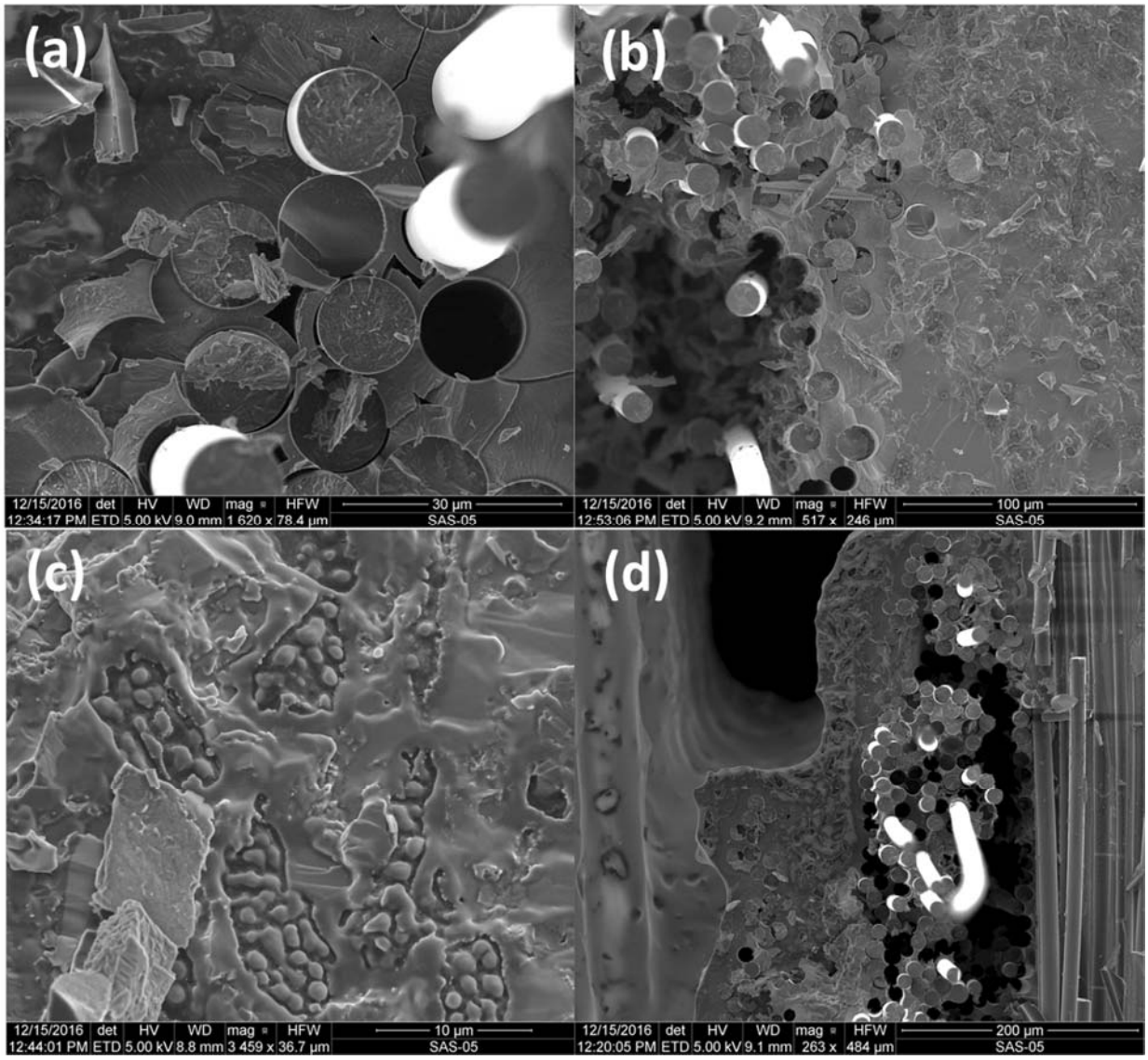

Figure A27: Higher-magnification images of the fracture surface of specimen 16-045 tested in fatigue at 1200°C in air showing (a) non-oxidized fiber breakage; (b) overview of non-oxidized fiber region; (c) non-oxidized matrix fractograph; (d) fiber pullout adjacent to glassy phase on edge of void

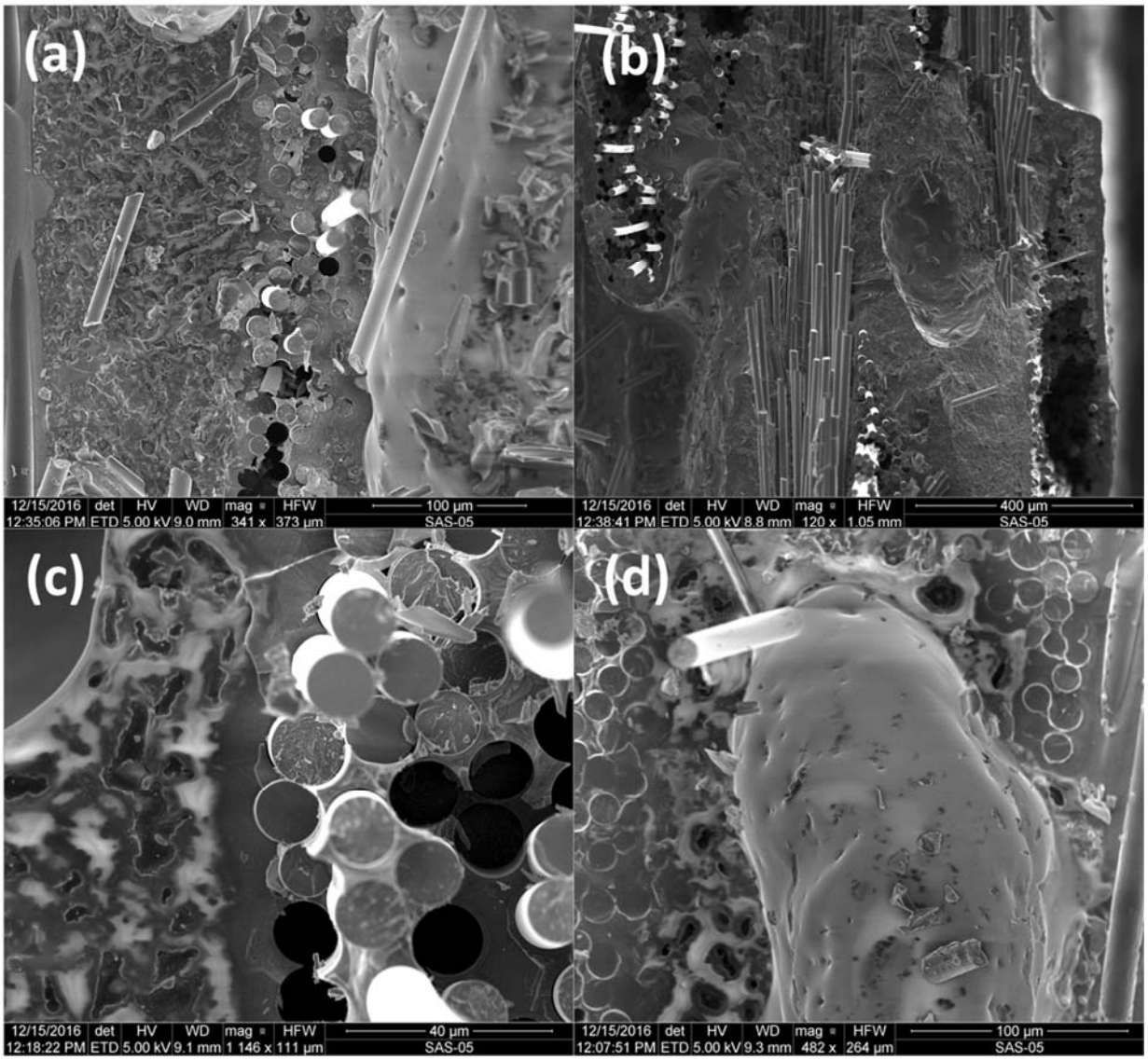

Figure A28: Higher-magnification images of the fracture surface of specimen 16-045 tested in fatigue at 1200°C in air showing (a) fiber pull-out on edge of exterior void; (b) void interiors; (c) non-oxide region showing charging under SEM; (d) oxidized fiber tows surrounding void

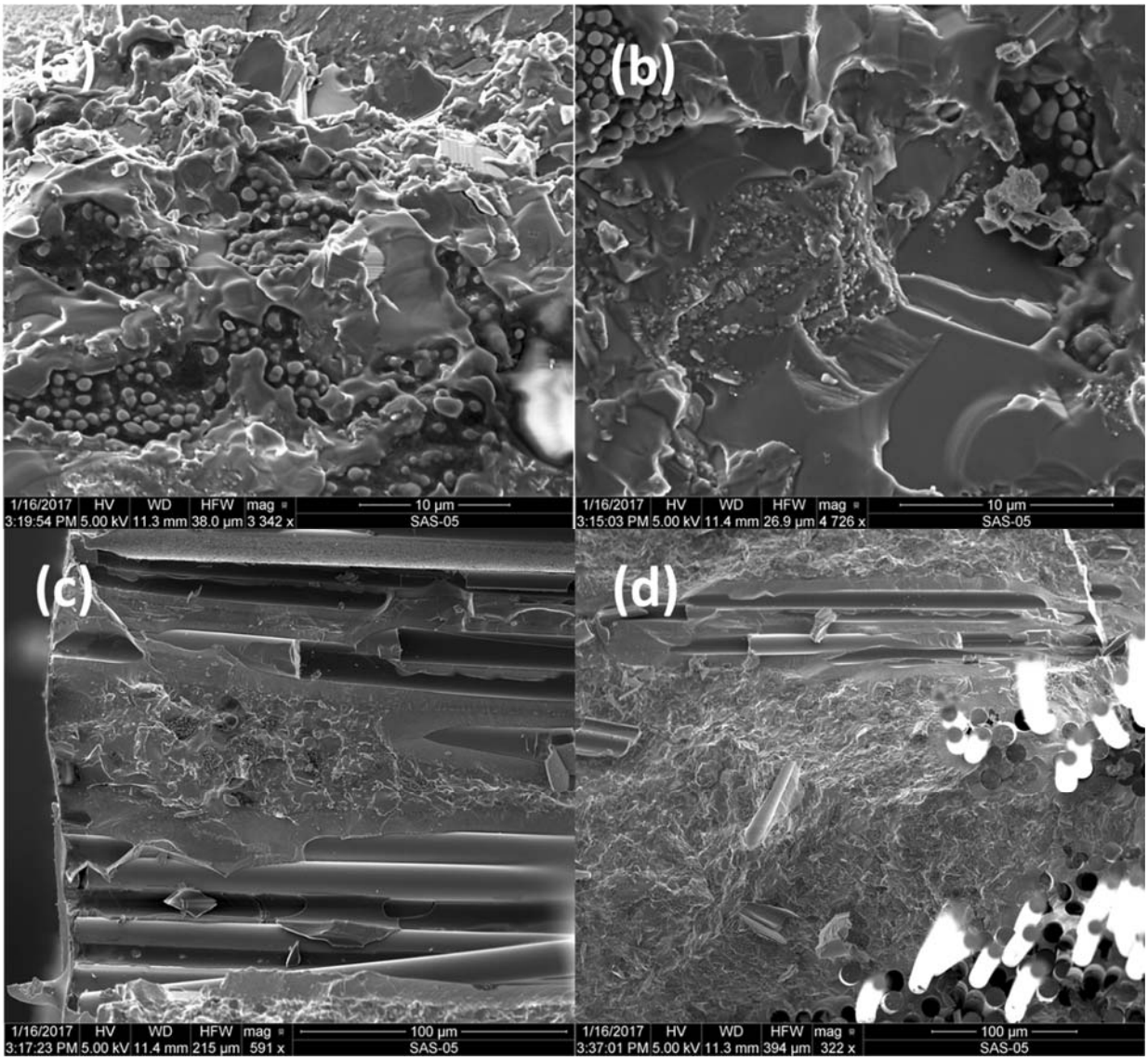

Figure A29: Higher-magnification images of the fracture surface of specimen 16-045 tested in fatigue at 1200°C in air showing (a) fractograph of non-oxidized fiber interphase; (b) fractograph of non-oxizdized matrix material; (c) overview of fractograph region; (d) non-oxidized matrix region

Specimen 16-057, tested in tension-tension fatigue at 1200°C in air.

σ_{max} = 160 MPa, N_f = 1,220

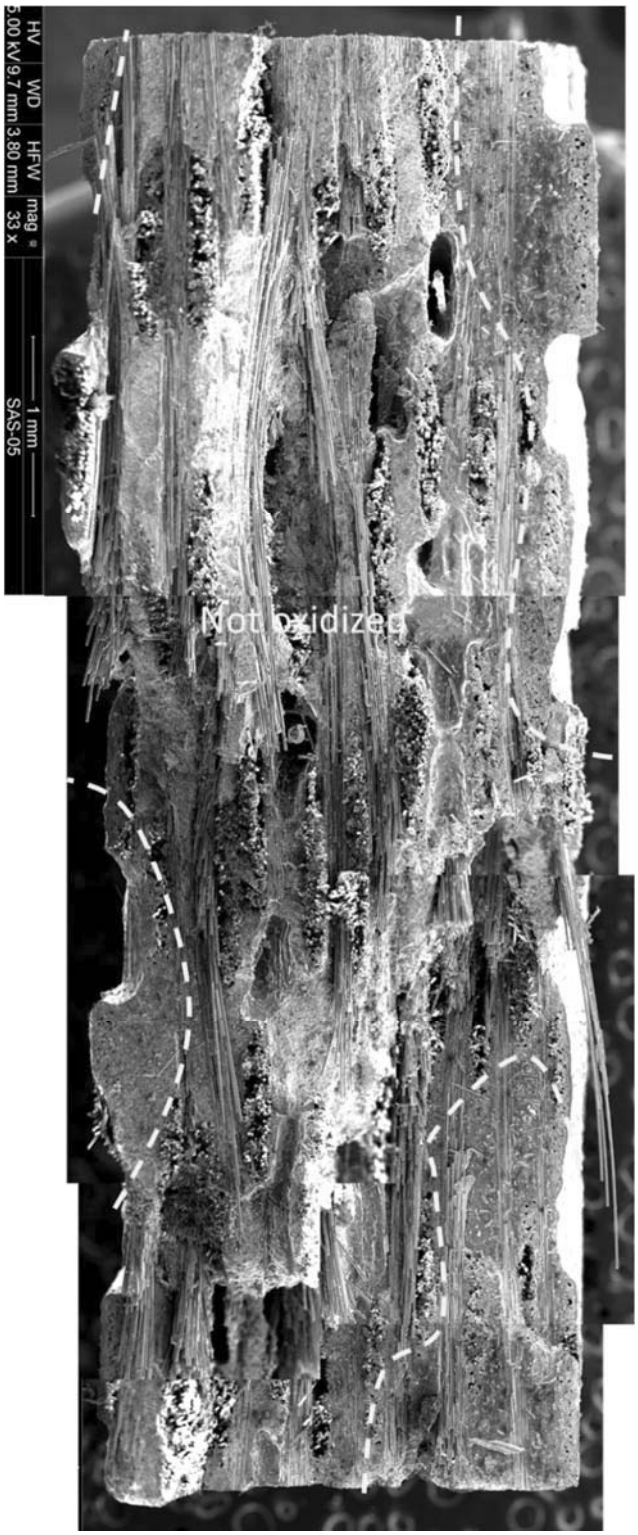

Figure A30: Micrograph of the fracture surface of specimen 16-057, tested in fatigue at 1200°C in air. σ_{max} = 160 MPa, N_f = 1,220

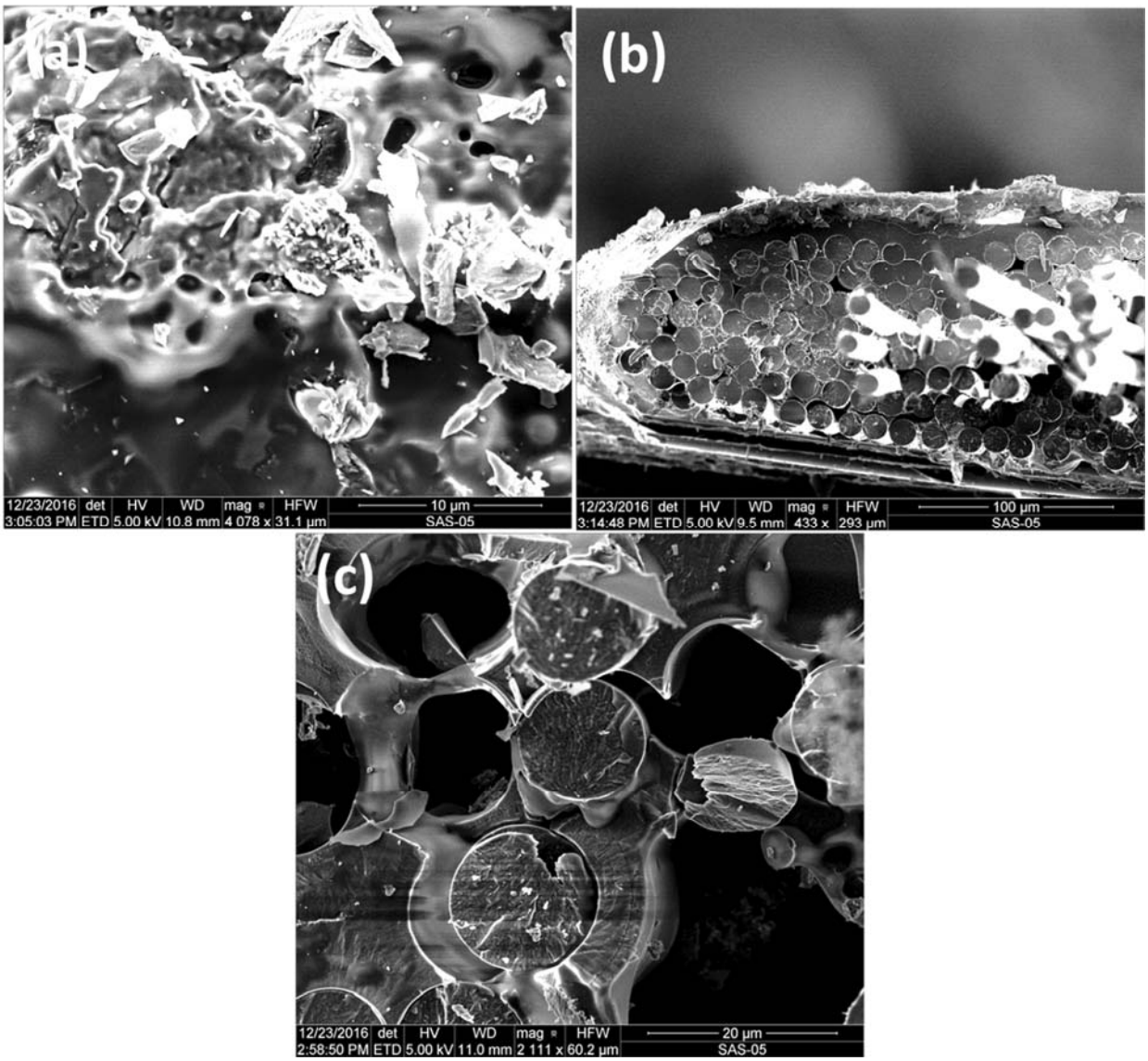

Figure A31: Higher-magnification images of the fracture surface of specimen 16-057 tested in fatigue at 1200°C in air showing (a) glassy region of f matrix; (b) oxidation causing partial fusion of fibers in tow; (c) non-oxidized fiber pull-out

Specimen 16-033, tested in tension-tension fatigue at 1200°C in steam.

σ_{max} = 100 MPa, N_f > 200,000

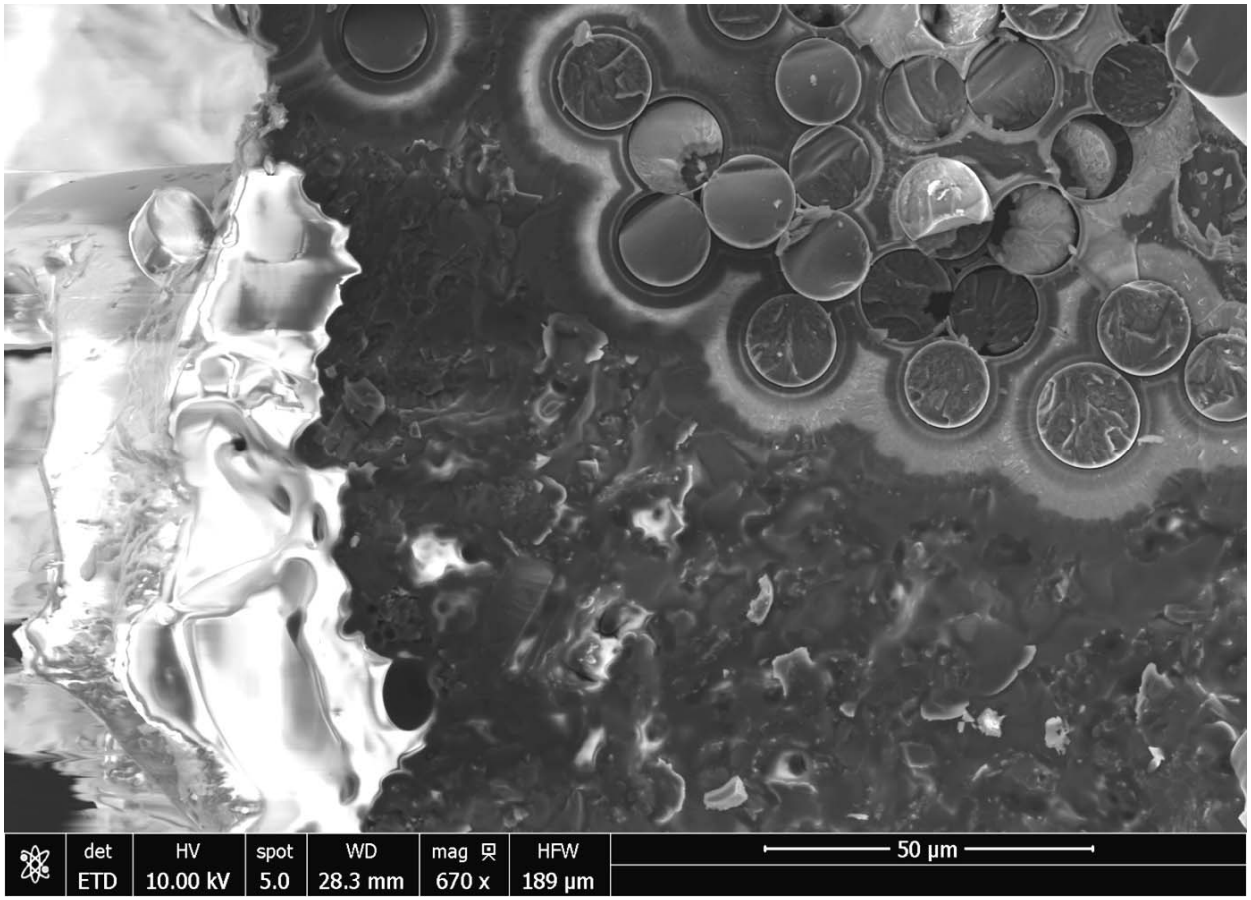

Figure A32: Higher-magnification image of the fracture surface of specimen 16-033 tested in fatigue at 1200°C in steam showing microscope charging on the glassy phase on the exterior of the specimen

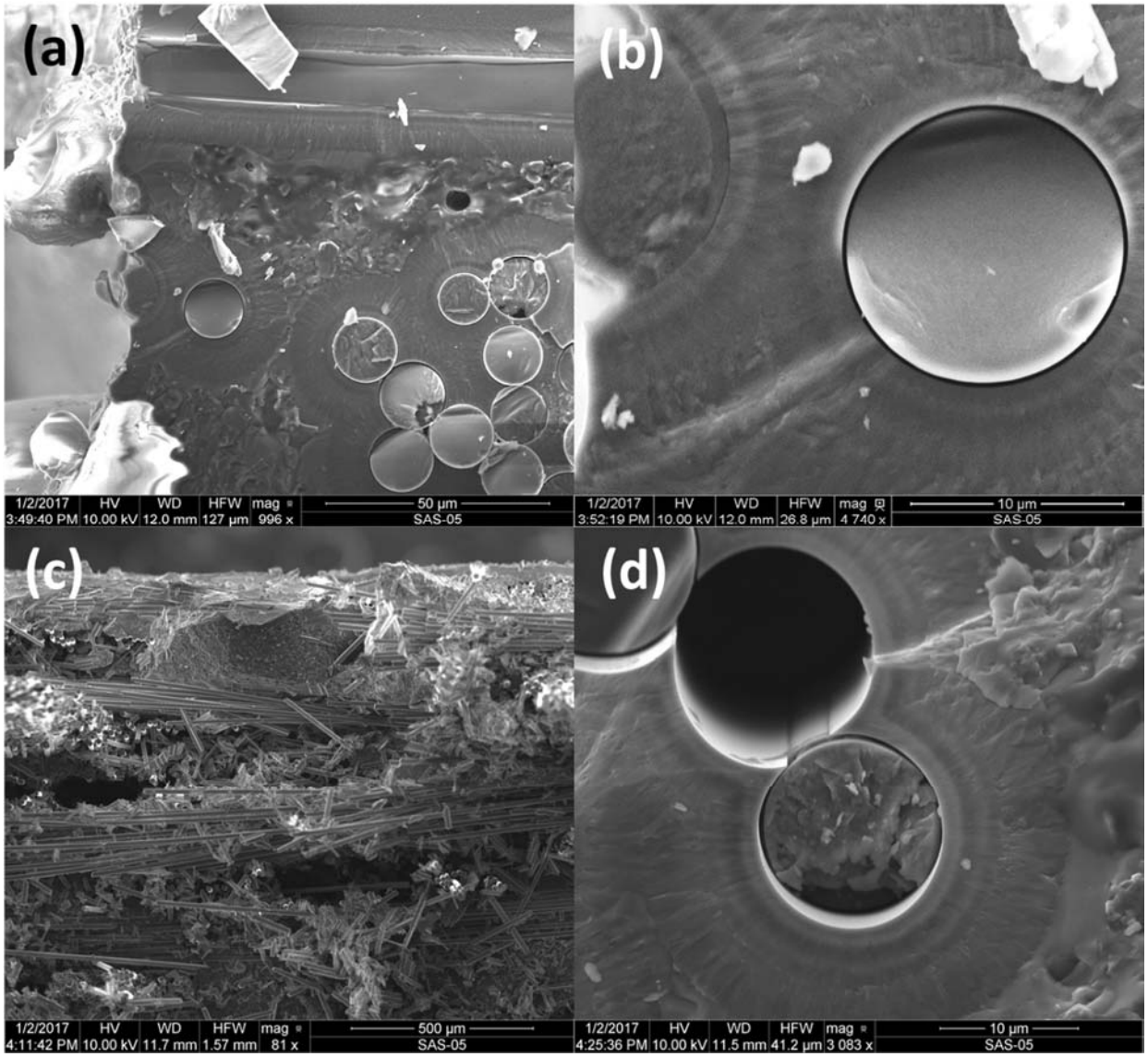

Figure A33: Higher-magnification images of the fracture surface of specimen 16-033 tested in fatigue at 1200°C in steam showing (a) oxidized and non-oxidized fiber fracture surfaces; (b) fiber fracture surface; (c) matrix fractograph amidst fiber pull-out region; (d) non-oxidized fiber fracture

Specimen 16-046, tested in tension-tension fatigue at 1200°C in steam.

σ_{max} = 110 MPa, N_f > 200,000

Figure A34: Fracture surface overview of specimen 16-046, tested in fatigue to runout at 1200°C in steam. σ_{max} = 110 MPa, N_f > 200,000. Evidence of oxidation was present on the face of the specimen and within an exterior void.

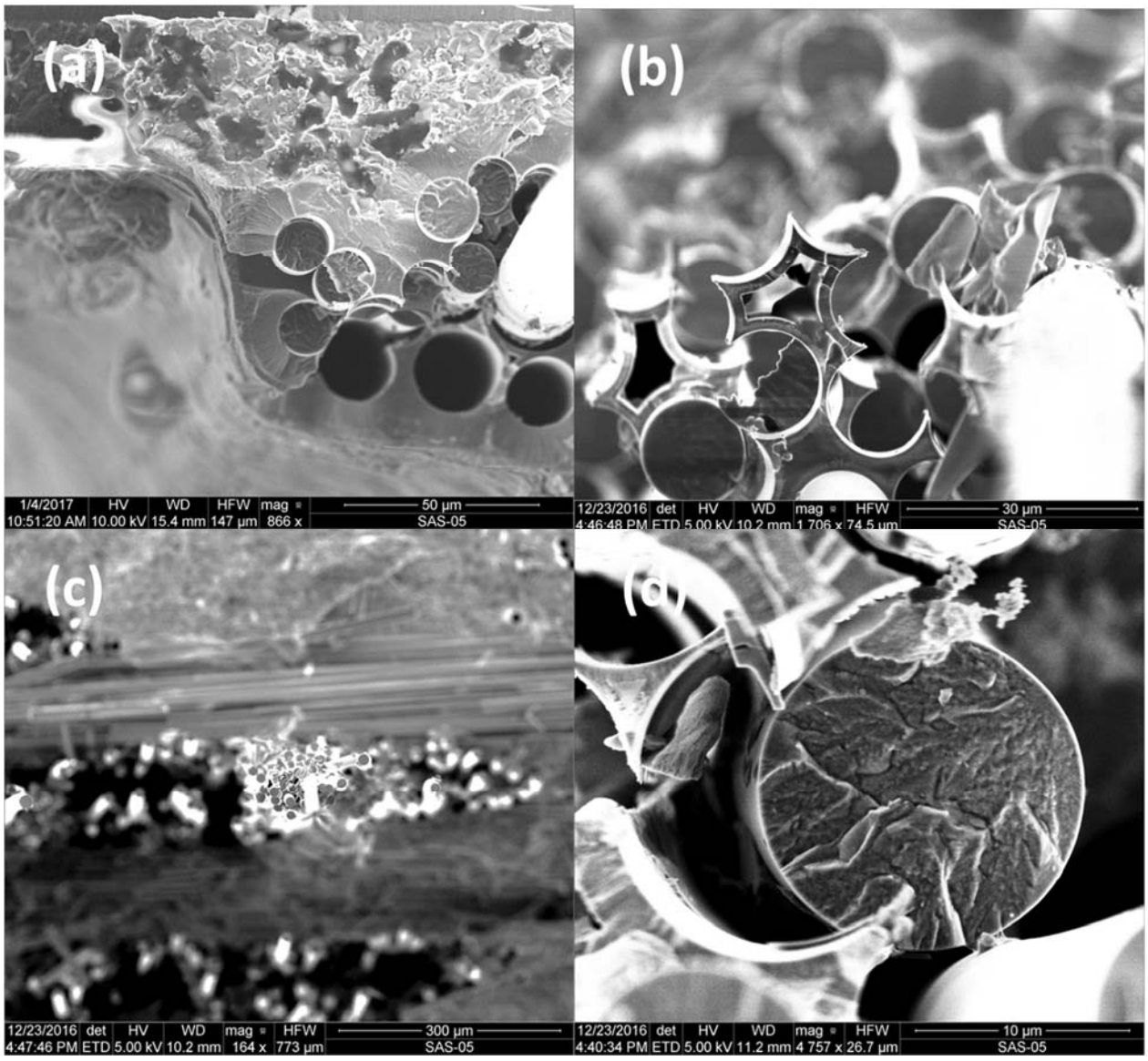

Figure A35: Higher-magnification images of the fracture surface of specimen 16-046 tested in fatigue at 1200°C in steam showing (a) non-oxidized fiber pull-out in exterior tow; (b) non-oxidized fiber features; (c) multiple fiber pull-out; (d) fiber fracture surface

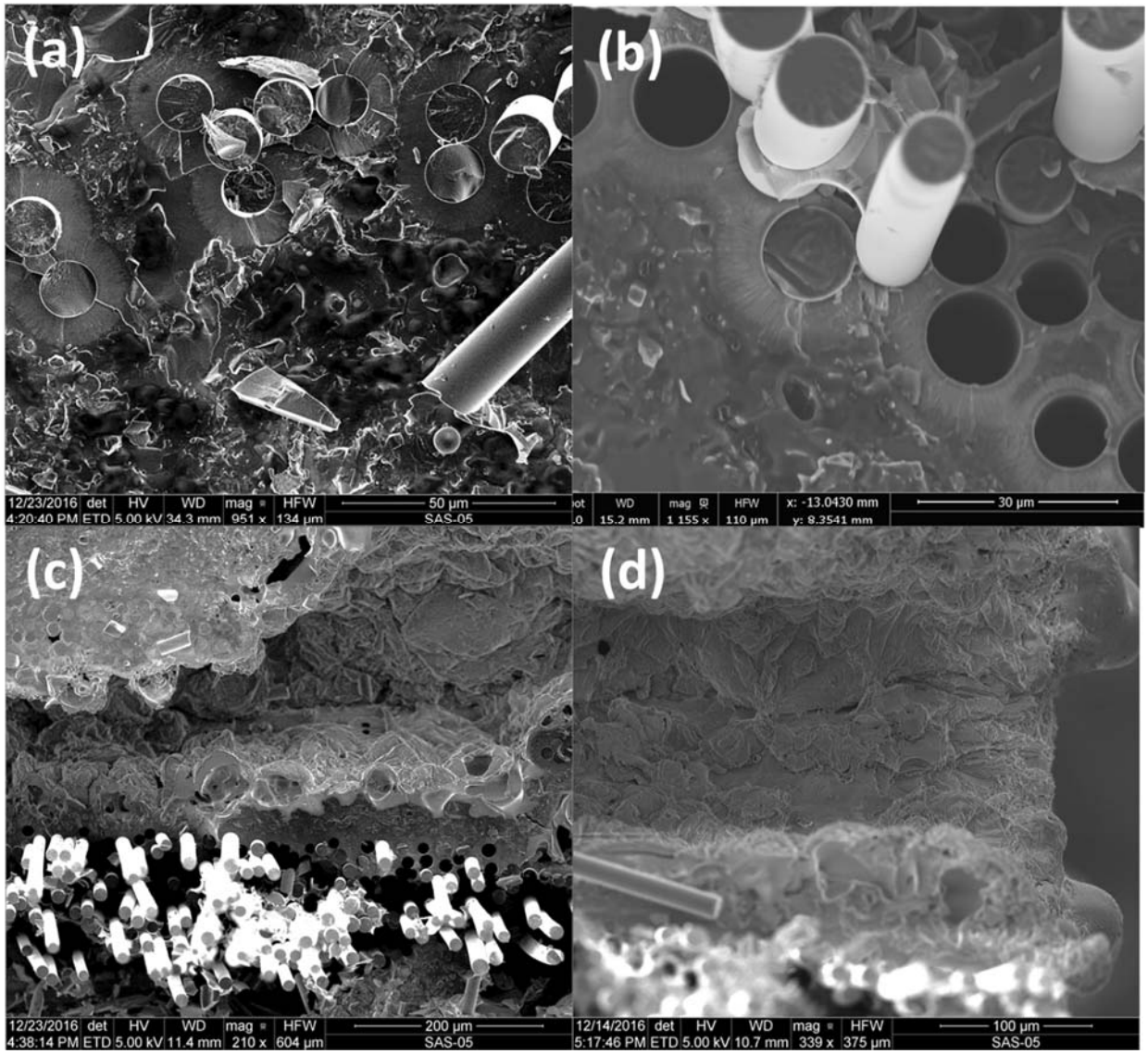

Figure A36: Higher-magnification images of the fracture surface of specimen 16-046 tested in fatigue at 1200°C in steam showing (a) non-oxidized fibers and matrix; (b) non-oxidized fiber pull-out; (c) glassy surface of exterior void with adjacent fiber-to-fiber bonding at top of image; (d) glassy surface detail

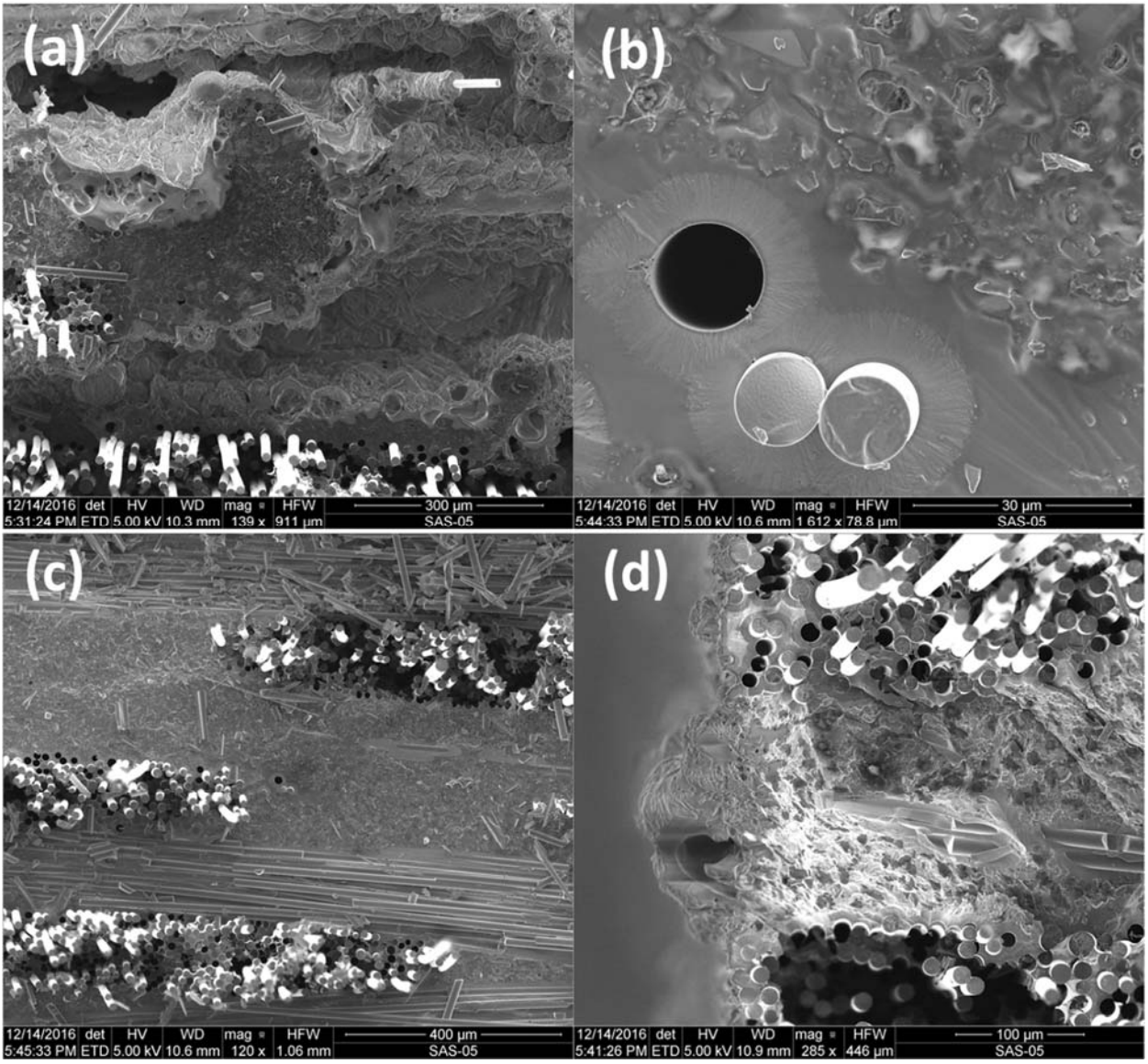

Figure A37: Higher-magnification images of the fracture surface of specimen 16-046 tested in fatigue at 1200°C in steam showing (a) environmental ingress through void; (b) non-oxidized fiber pull-out region; (c) non-oxidized fiber pull-out; (d) glassy buildup on exterior of specimen with adjacent not-oxidized fiber pull-out

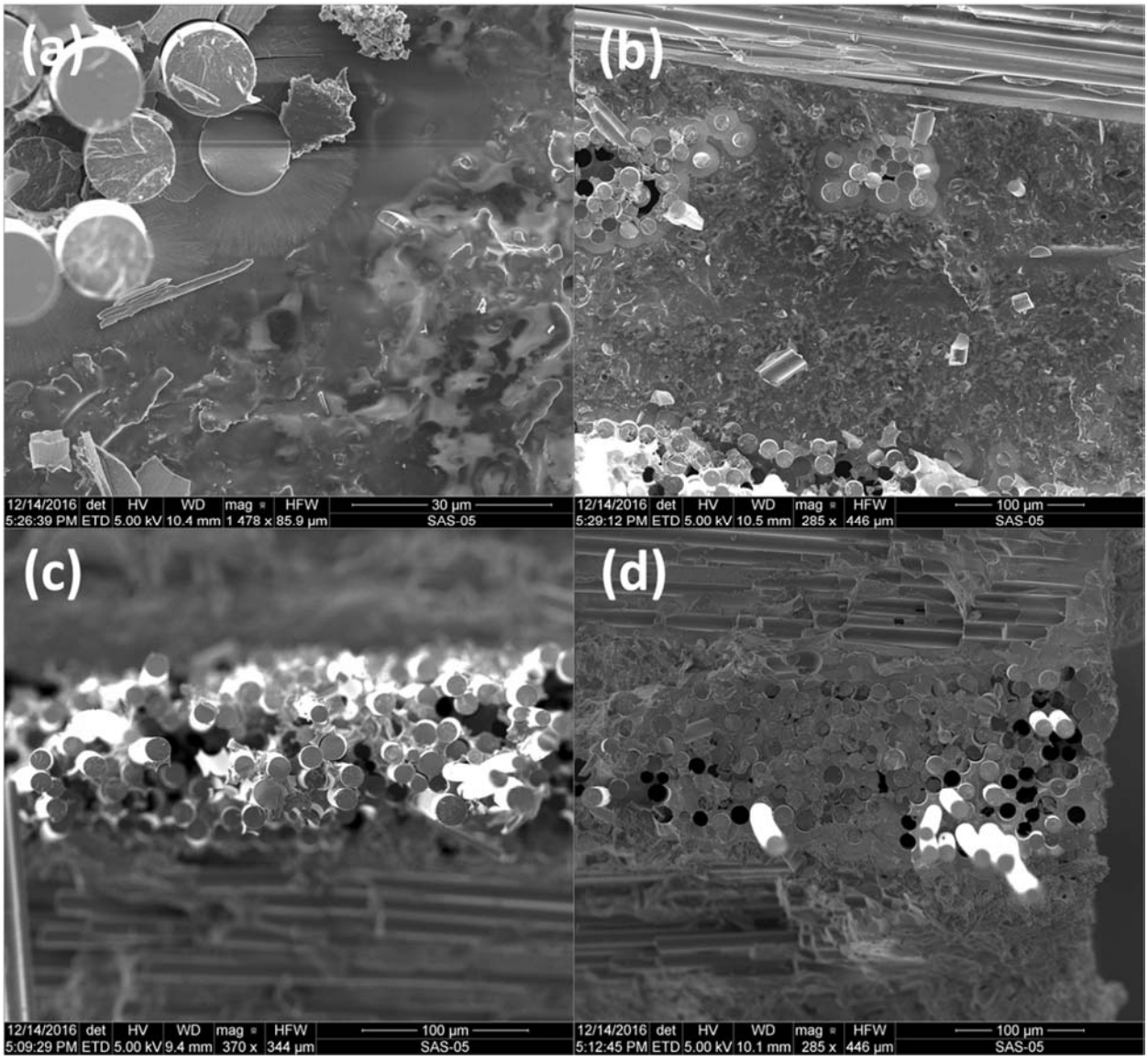

Figure A38: Higher-magnification images of the fracture surface of specimen 16-046 tested in fatigue at 1200°C in steam showing (a,b) isolated fiber pull-out; (c) pull-out of fiber tow; (d) mixed oxidized and non-oxidized fiber pull-out

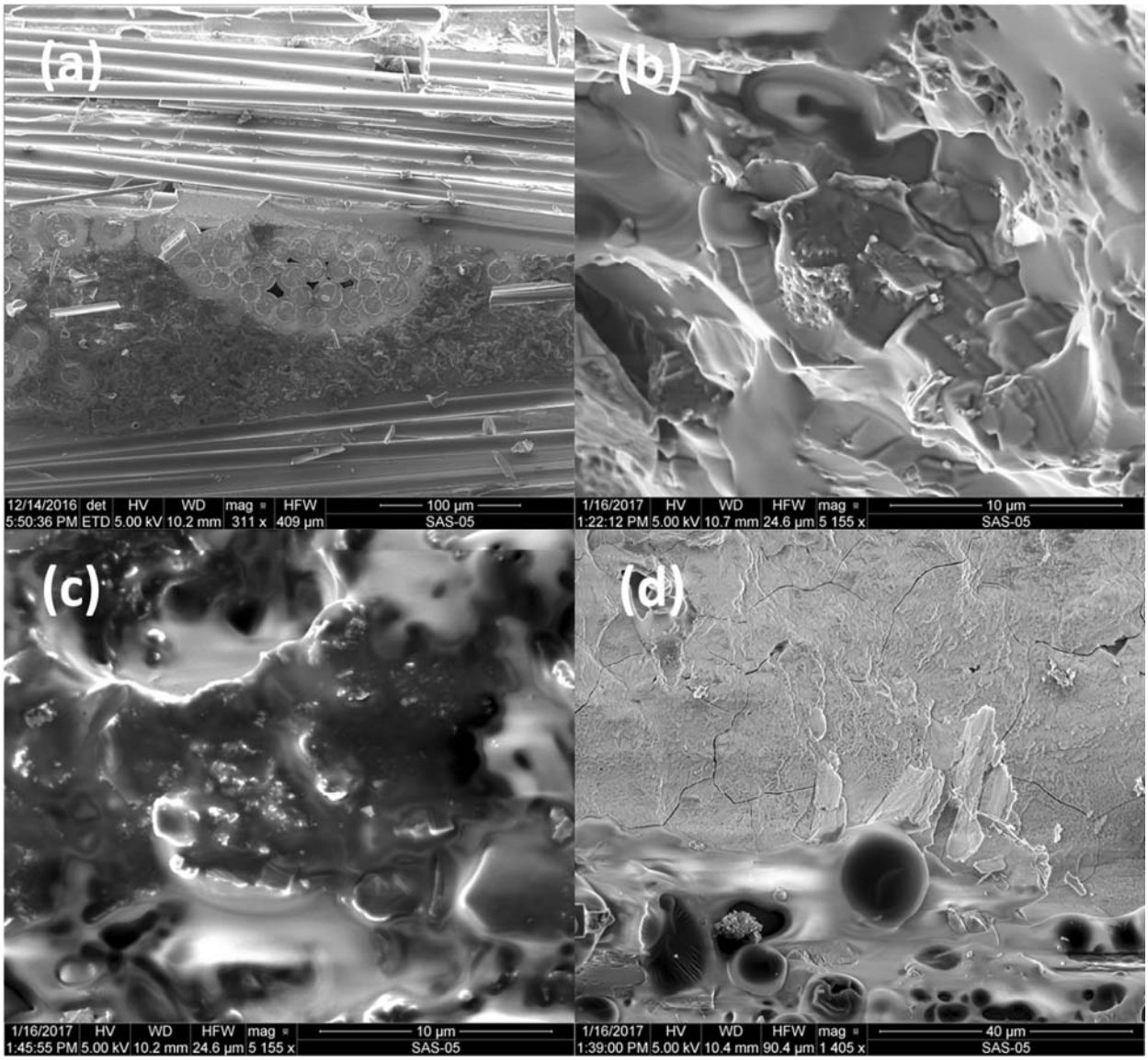

Figure A39: Higher-magnification images of the fracture surface of specimen 16-046 tested in fatigue at 1200°C in steam showing (a) fiber-to-fiber bonding causing fracture to form a single cleavage plane; (b,c) fractographs of non-oxidized matrix regions; (d) surface of oxidized region on specimen edge showing glassy layer and bubbling

Specimen 16-032, tested in tension-tension fatigue at 1200°C in steam.

σ_{max} = 120 MPa, N_f = 5,311

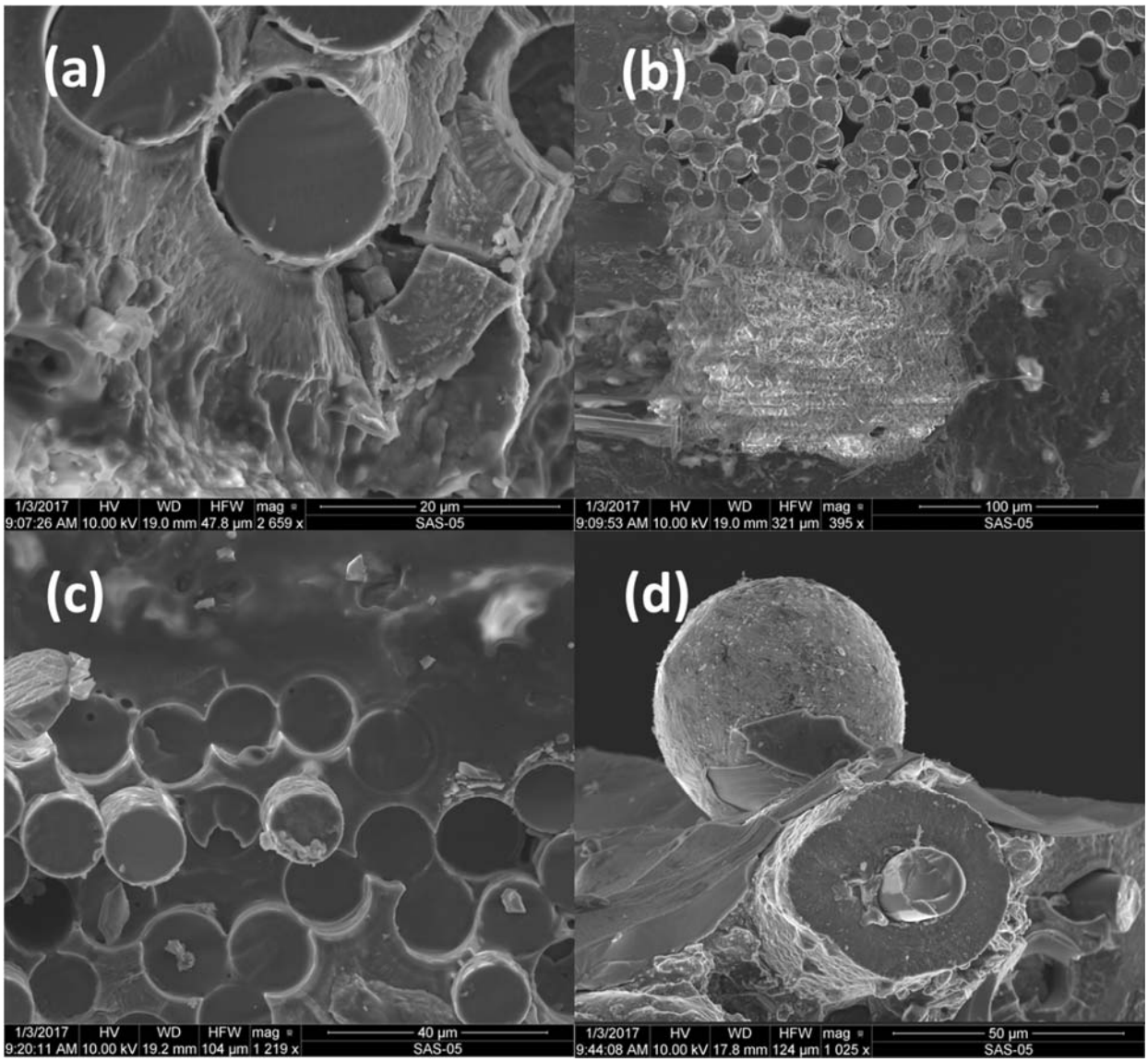

Figure A40: Higher-magnification images of the fracture surface of specimen 16-032 tested in fatigue at 1200°C in steam showing (a) non-oxidized fracture surface around fiber; (b) possible oxidation from exterior void influencing fiber tow; (c) glassy buildup on fibers; (d) surface buildup in steam

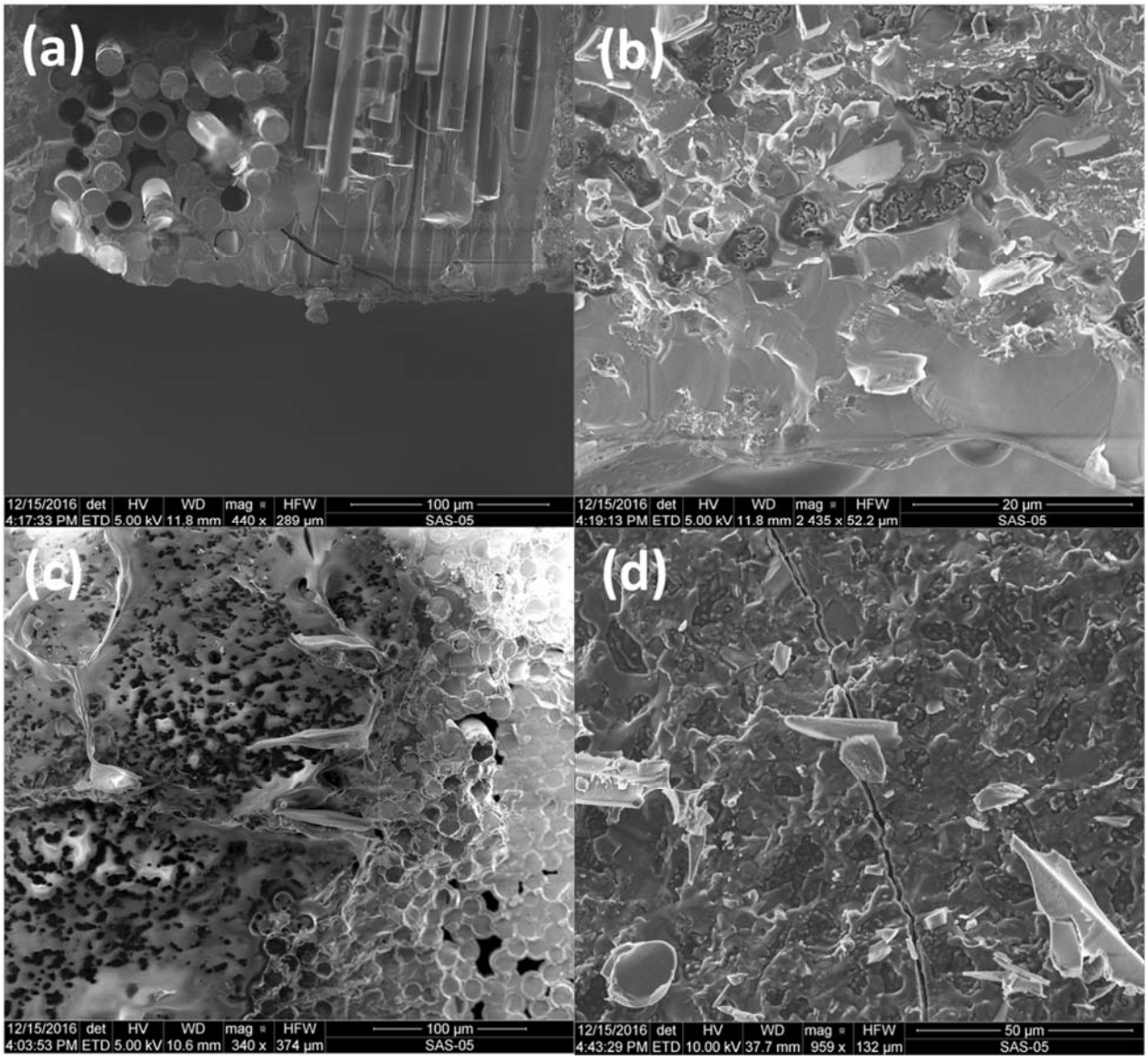

Figure A41: Higher-magnification images of the fracture surface of specimen 16-032 tested in fatigue at 1200°C in steam showing (a) fiber pull-out at edge; (b) non-oxidized matrix fractograph; (c) glassy layer near fibers; (d) cracking in non-oxidized region

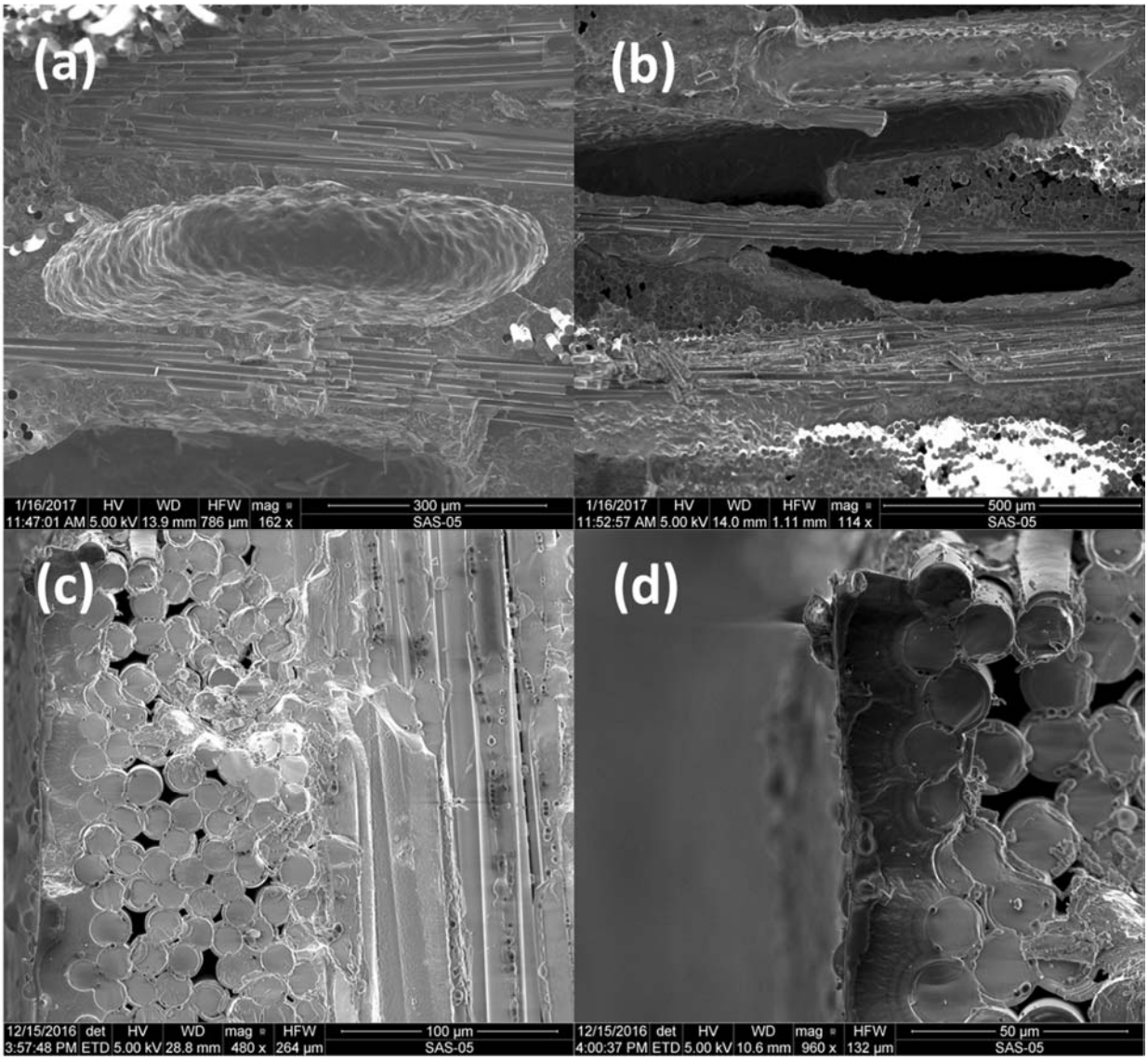

Figure A42: Higher-magnification images of the fracture surface of specimen 16-032 tested in fatigue at 1200°C in steam showing (a,b) void interior surface; (c) fiber-to-fiber bonding; (d) corner fiber region with signs of oxidation

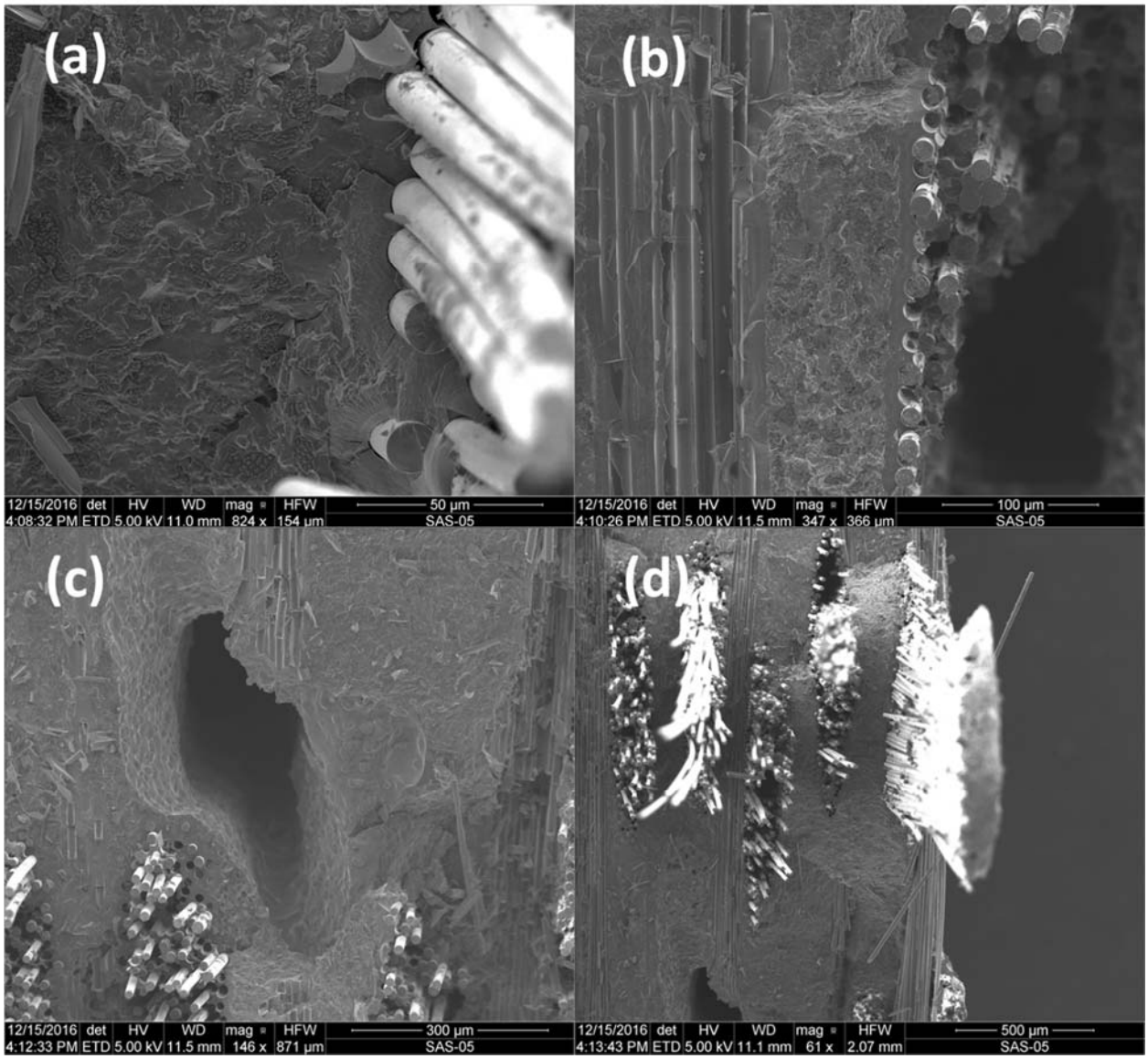

Figure A43: Higher-magnification images of the fracture surface of specimen 16-032 tested in fatigue at 1200°C in steam showing (a) non-oxidized fiber pull-out; (b) matrix and fiber features on void edge; (c) void appearance in steam-tested specimens; (d) individual fiber pull-out and tow pull-out

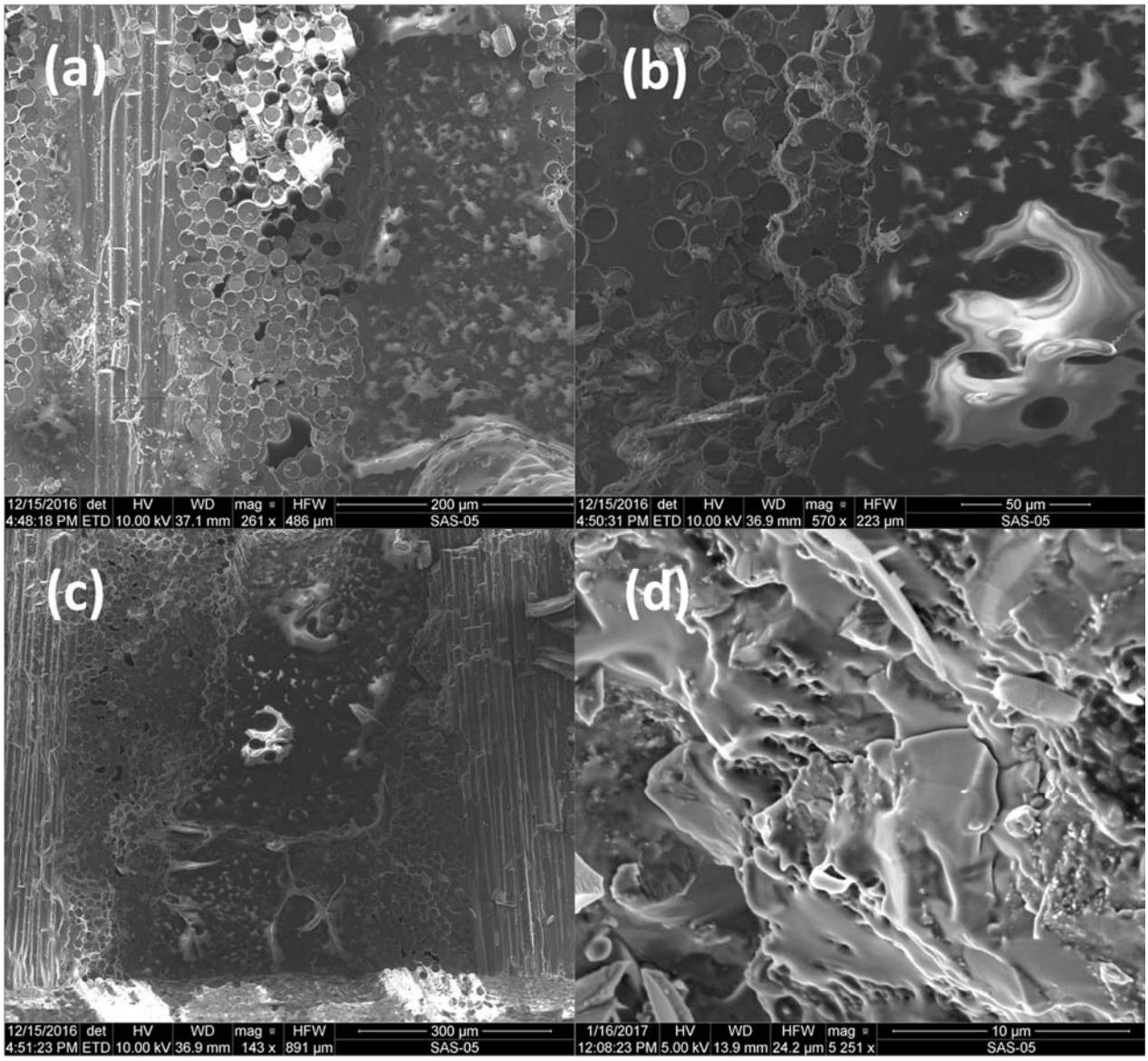

Figure A44: Higher-magnification images of the fracture surface of specimen 16-032 tested in fatigue at 1200°C in steam showing (a) some fiber pull-out amidst glassy layer and fiber-to-fiber bonding at bottom of image; (b) microscope charging on glassy surface; (c) overview of glassy region; (d) non-oxidized matrix fracture surface

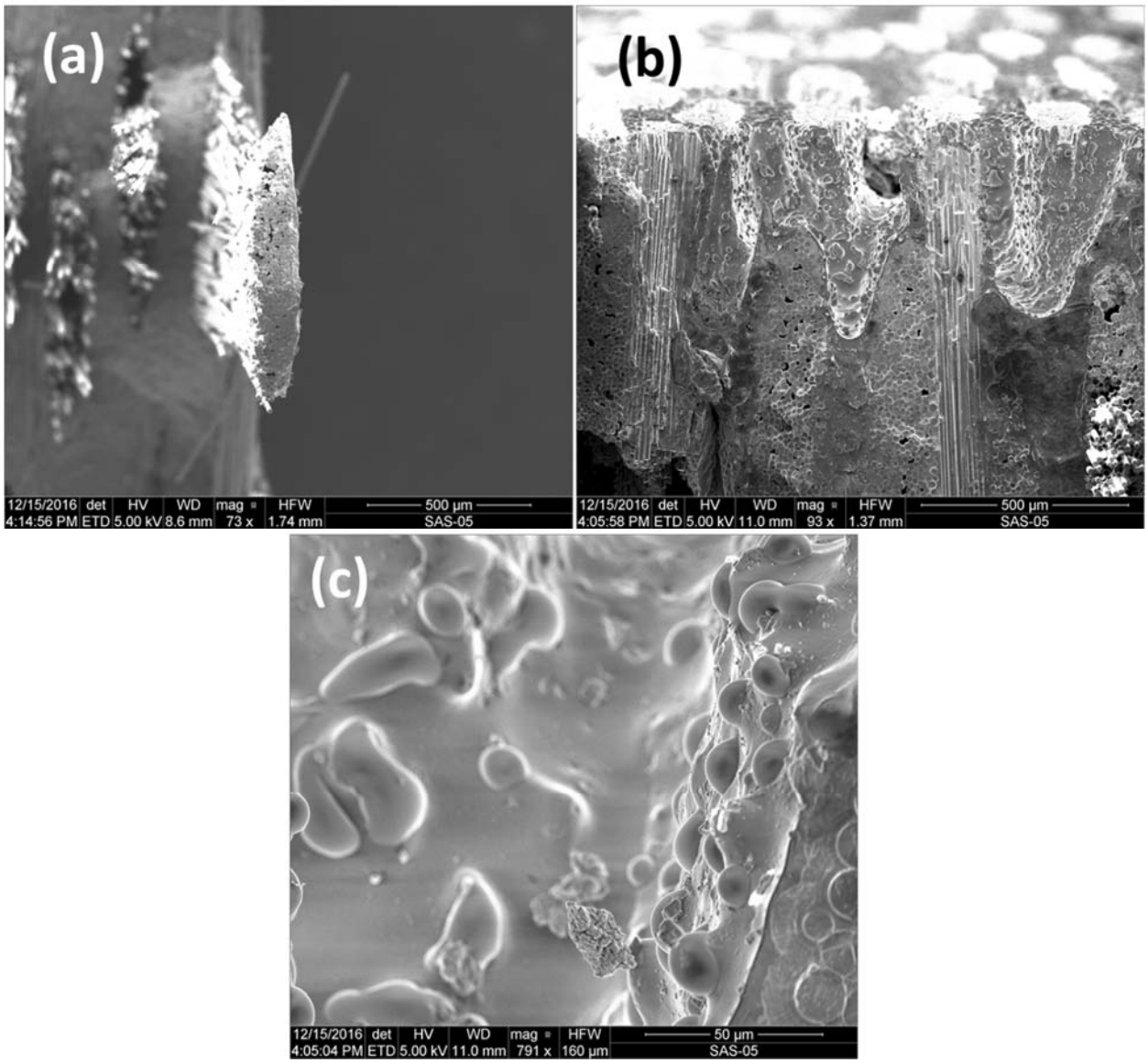

Figure A45: Higher-magnification images of the fracture surface of specimen 16-032 tested in fatigue at 1200°C in steam showing (a) evidence of fiber-to-fiber bonding in pulled-out tow; (b) exterior voids leading into specimen; (c) surface of void interior

Specimen 16-058, tested in tension-tension fatigue at 1200°C in steam.

σ_{max} = 130 MPa, N_f = 3,201

Figure A46: SEM micrograph of the fracture surface of specimen tested in fatigue at 1200°C in steam. σ_{max} = 130 MPa, N_f =3,201.

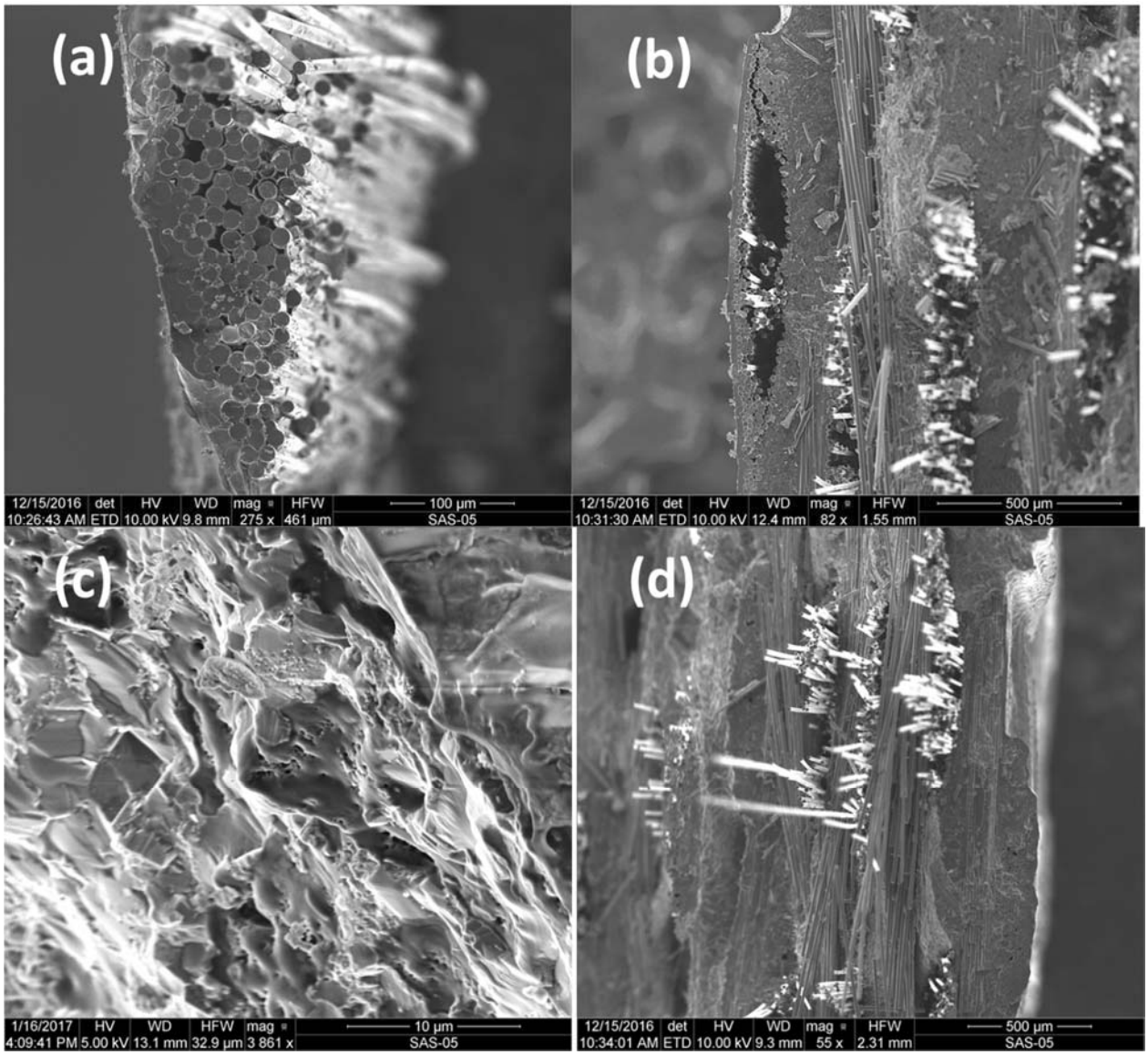

Figure A47: Higher-magnification images of the fracture surface of specimen 16-058 tested in fatigue at 1200°C in steam showing (a) fiber-to-fiber bonding in pulled-out tow; (b) cracking in tow exterior; (c) non-oxidized matrix fractograph; (d) fiber pull-out region

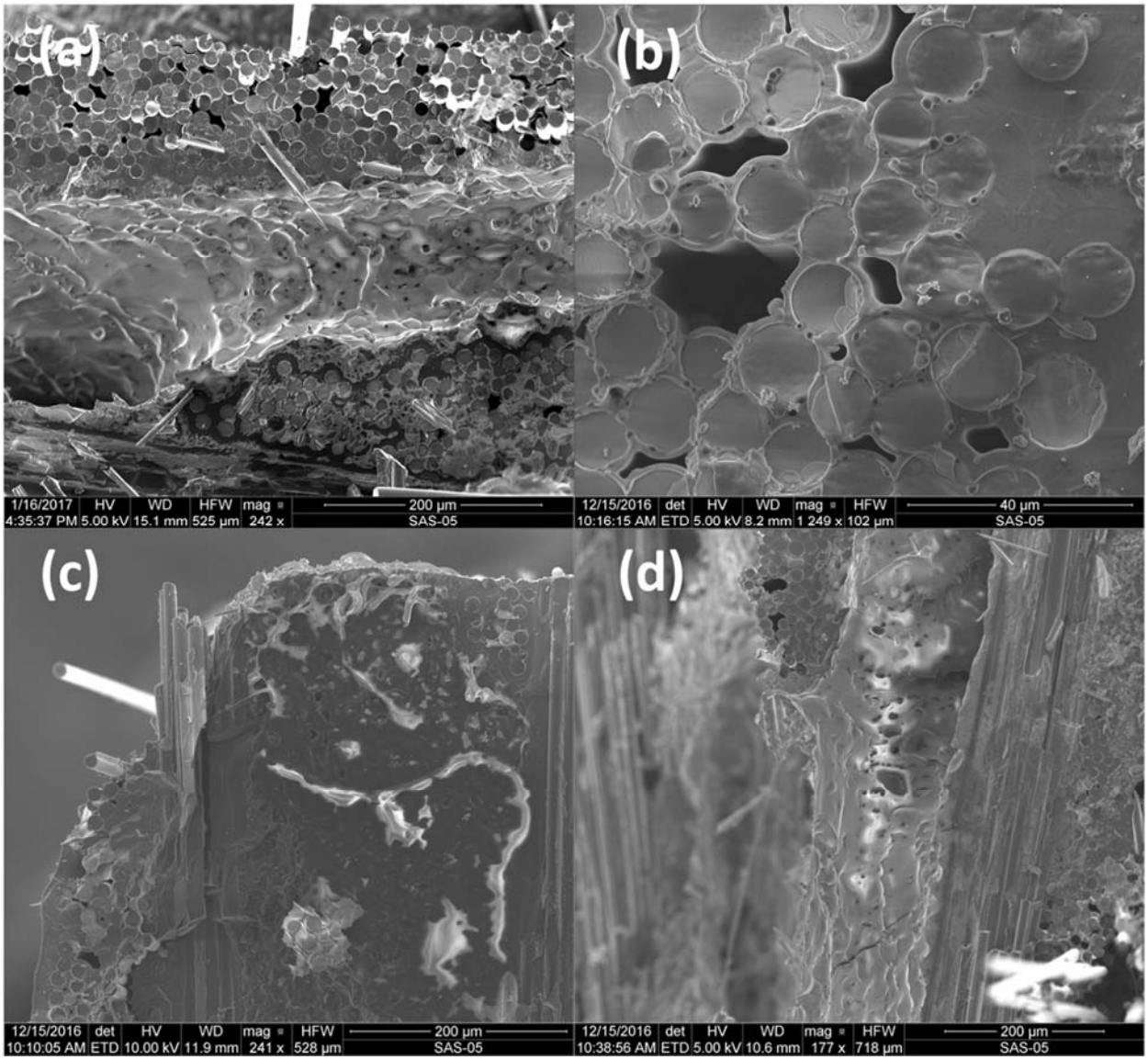

Figure A48: Higher-magnification images of the fracture surface of specimen 16-058 tested in fatigue at 1200°C in steam showing (a) void interior in glassy region; (b) fiber-to-fiber bonding indicating oxidation; (c) glassy layer; (d) viscous layer indicating oxidation

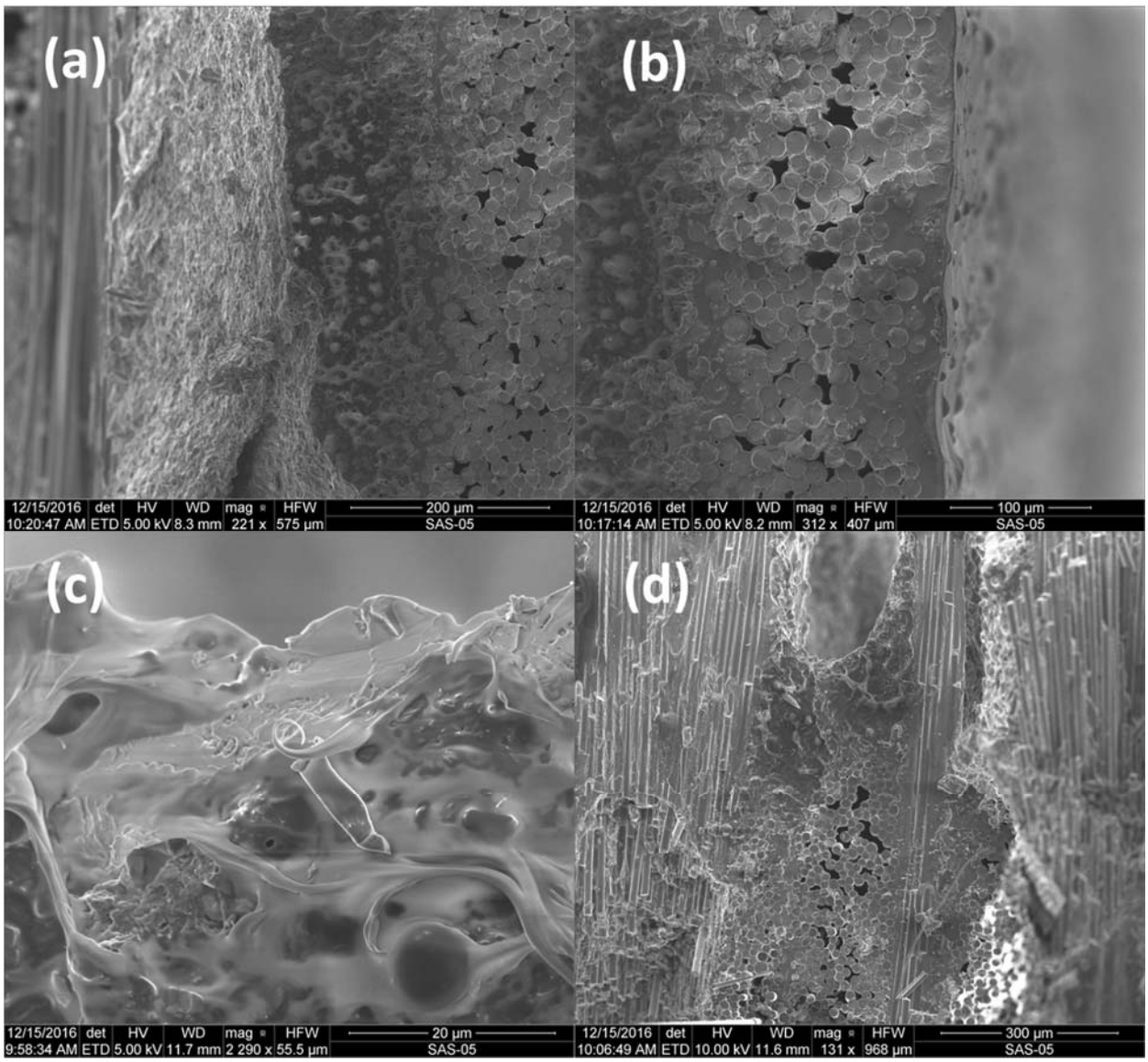

Figure A49: Higher-magnification images of the fracture surface of specimen 16-058 tested in fatigue at 1200°C in steam showing (a) non-oxide matrix region transitioning to glassy region with fiber fusion; (b) fiber-to-fiber bonding on edge of surface; (c) glassy region near specimen edge; (d) glassy region on edge of void

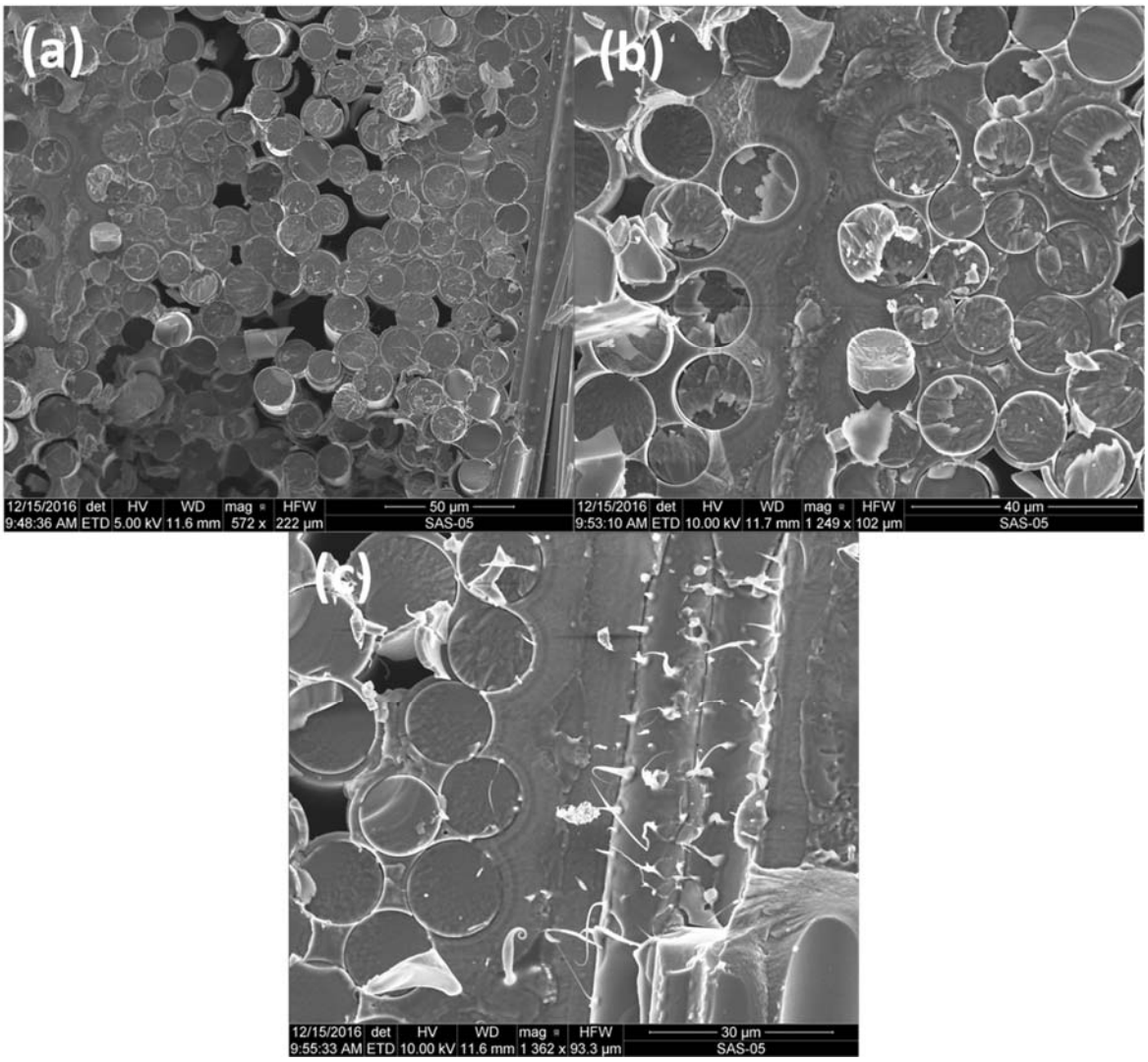

Figure A50: Higher-magnification images of the fracture surface of specimen 16-058 tested in fatigue at 1200°C in steam showing (a) some fiber-to-fiber bonding; (b) non-oxide fiber failure; (c) interphase forming glass features on transverse fibers

Appendix C - Microstructural Characterization of Temperature Calibrator Test Specimen

Interaction occurred between the surface of specimen 16-044 and calibration thermocouples. After calibration was no longer needed, the specimen was tested in fatigue in air at 1200°C with a max stress of 130 MPa, and survived for 4,506 cycles. The specimen surface had a black residue located where the thermocouples had been placed shown in Fig. A51. The specimen failed in the same region, shown in Fig. A52.

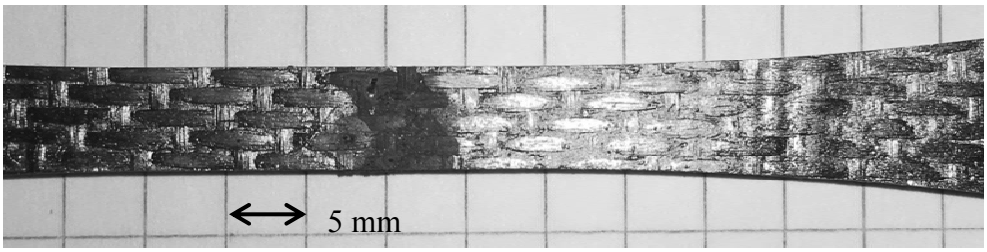

Figure A51: Discoloration where Type-R (Pt/Rh) thermocouple contacted the surface

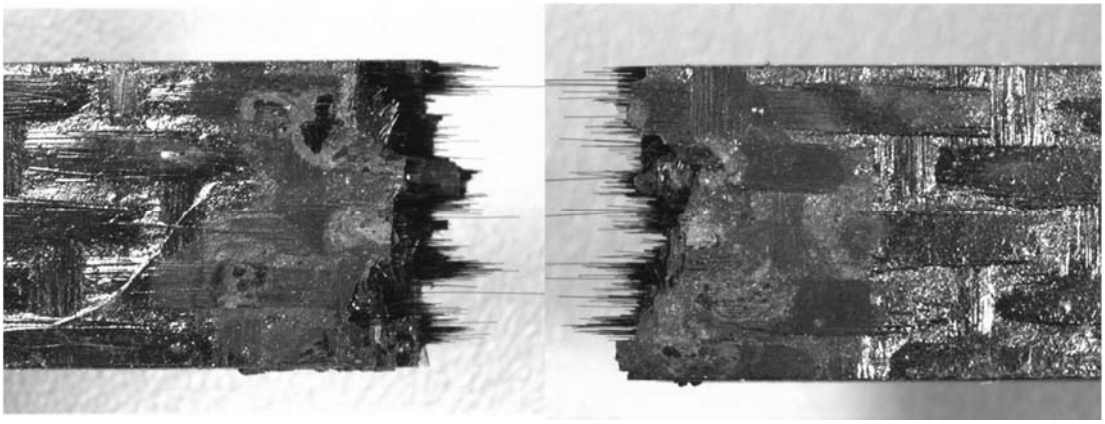

Figure A52: Failure initiated where thermocouples beads contacted the calibrator specimen.

Imaging the specimen fracture surface in the SEM revealed the presence of spheroid structures not present on the other fracture surface. EDS was performed on these structures and

revealed a eutectic composition of Platinum and Silicon. The platinum came from the thermocouples themselves. Silicon combines with platinum to form a eutectic alloy that has a much lower melting point than platinum itself, around 850°C [51]. The micrograph of the structure and resulting EDS spectrum is shown in Fig. A53.

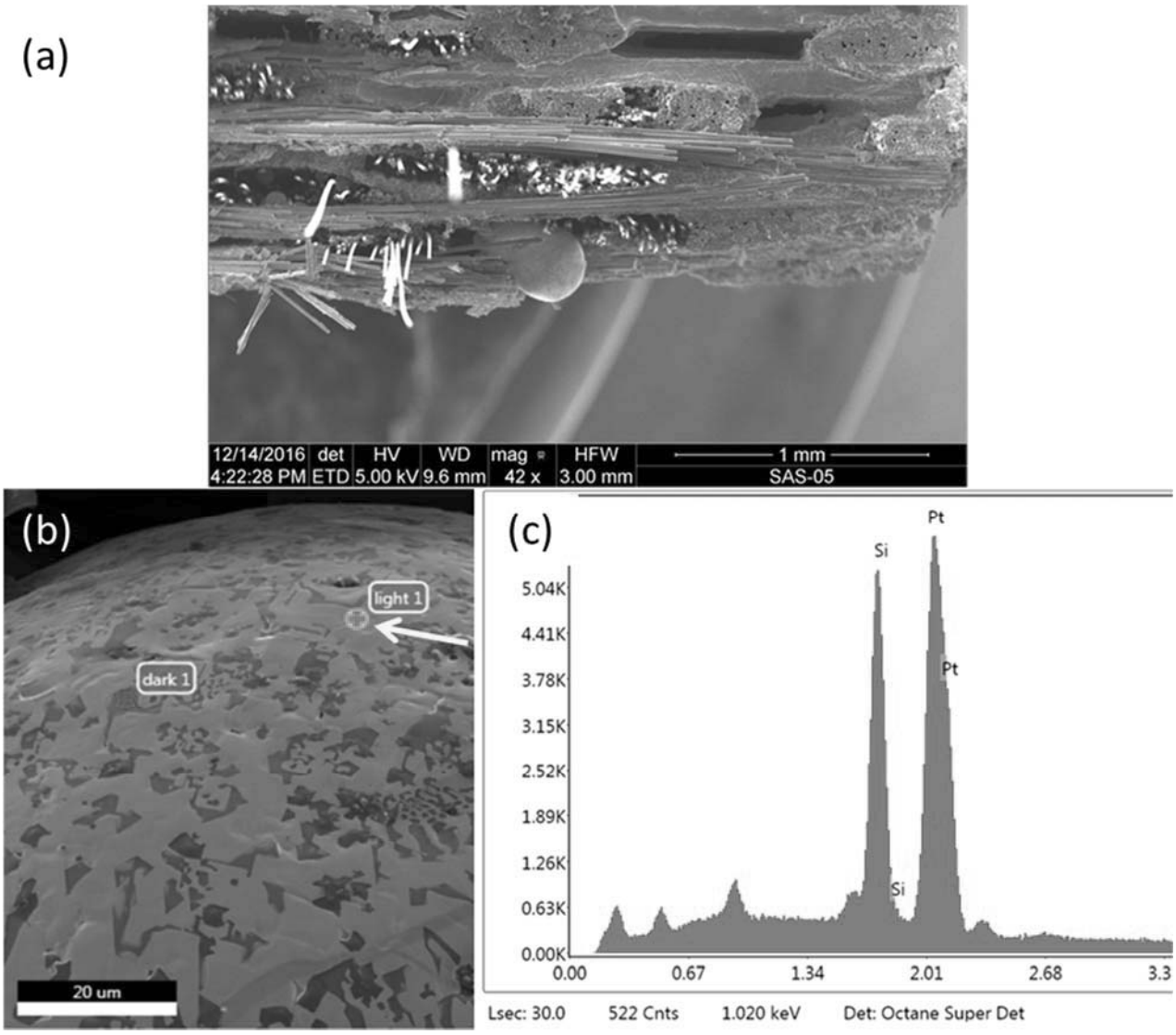

Figure A53: (a) Broken thermocouple tip embedded in fiber bundle, (b) Eutectic surface, (c) EDS spectrum displaying approximate concentration of Si and Pt

Fig. A54 confirms that silicon leftover from fabrication remains as a coating on the specimen surface, and is free to react with material in contact with it. Since Type–R thermocouples are extremely common in high-temperature testing, this result is significant for future research on melt-infiltrated materials. The reaction has considerable implications for machine design as well. For instance, if CMC part is held in place with a metal fastener or is in contact with a metallic structure, the free silicon would react with the metal and potentially cause a failure.

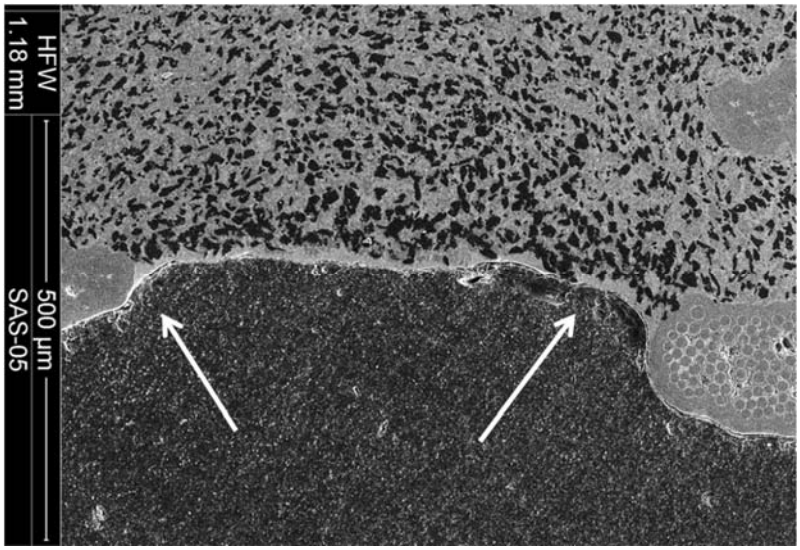

Figure A54: Light-colored layer indicates leftover silicon from infiltration dominates the specimen exterior.

Appendix D – Threshold Stress Intensity Factor for Crack Growth

The Hi-Nicalon^{TM}/BN/SMI-SiC composite exhibits threshold fatigue behavior, meaning if the threshold for crack initiation is not crossed, the material survives to run-out. This is analogous fatigue crack growth in metals. The increase in crack length per fatigue cycle, da/dN, occupies three different regimes as shown in Figure A55. First, the crack is initiated at the threshold cyclic stress intensity, ΔK_{th}. The crack then enters a stable growth regime until it becomes unstable in region III, where the stress intensity factor is high enough to cause uncontrolled fracture and ultimately failure [52].

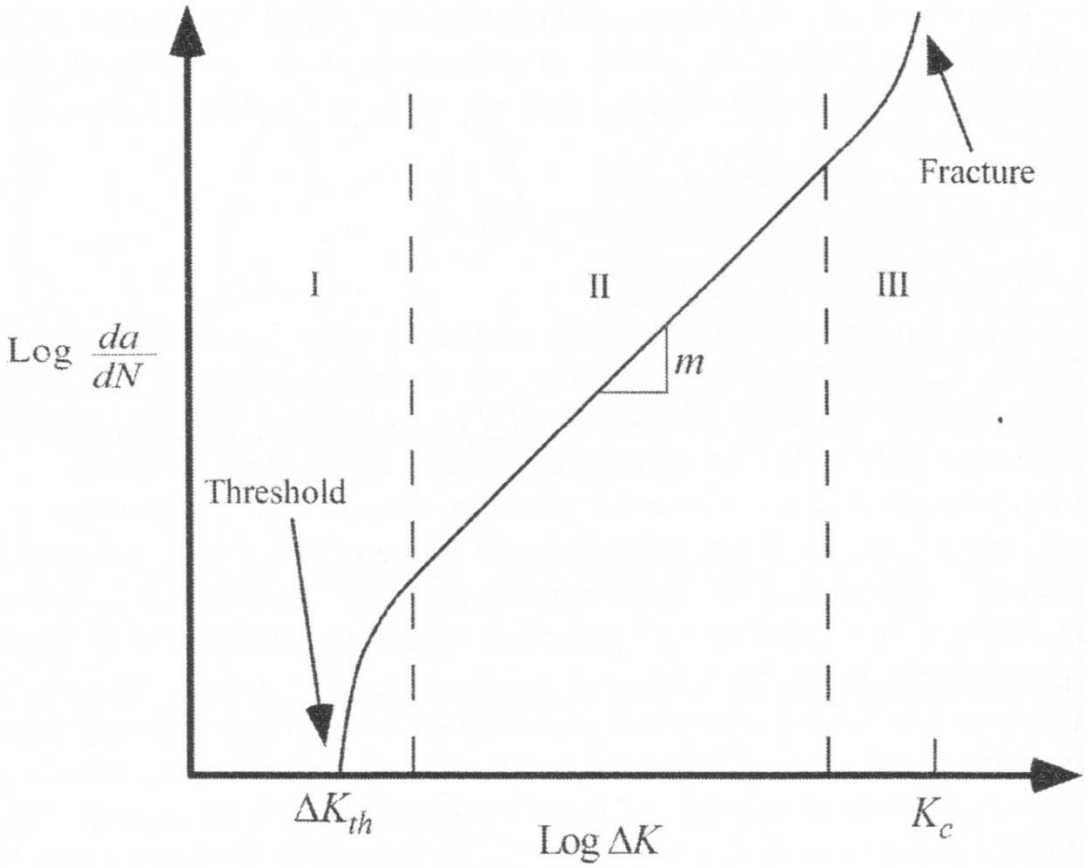

Figure A55: Crack growth regimes in engineering metals, where region II is described by the Paris law. CMCs show a much narrower region II and transition quickly to fast fracture.

Region I is typical of environmentally-assisted crack growth and depends on the concentration of chemical species that contributes to oxidation embrittlement [48]. Region II can be described with the Paris law,

$$\frac{da}{dN} = C\Delta K^m$$

where da/dN is the increase in crack length per cycle, C and m are material constants, and ΔK is the difference in cyclic stress intensity factor, ($K_{max} - K_{min}$) [44]. The specimens that that short fatigue lives showed oxidation over more of the fracture surface than the specimens that survived to run-out, indicating the surface must have been exposed to the environment for a number of cycles as the crack grew. One can conclude the material does not fail immediately upon crack initiation, but further studies are needed to accurately say whether crack growth is stable or uncontrolled.

Bibliography

[1] M. J. Moran and H. N. Shapiro, Fundamentals of Engineering Thermodynamics, 6th, Ed., Hoboken, NJ: Wiley, 2008.

[2] M. Standridge, "Aerospace materials - past, present and future," *Aerospace manufacturing and design,* 13 August 2014.

[3] T. Materia, "High Temperature Nickel-Based Superalloys for Turbine Discs: Part One," March 2011. [Online]. Available: http://www.keytometals.com/freedemo/page.aspx?ID=CheckArticle&site=ktn&NM=259. [Accessed 30 June 2016].

[4] M. F. Ashby and D. R. H. Jones, Engineering Materials I, third ed., Oxford: Elsevier, 2005.

[5] A. P. Mouritz, Introduction to Aerospace materials, Cambridge: Woodhead Publishing, 2012.

[6] General Electric, *GE Successfully Tests World's first rotating ceramic matrix composite material for next-gen combat engine,* Cincinnati, OH, 2015.

[7] A. A. Baker, Composite materials for aircraft structures, 2nd ed., AIAA, 2004, pp. 15-20.

[8] K. L. Luthra, "Emerging Applications and Challenges in using Ceramics at General Electric," *Ceramic Leadership Summit,* 2011.

[9] M. C. Halbig, M. H. Jaskowiak, J. D. Kiser and D. Zhu, "Evaluation of ceramic matrix composite technology for aircraft turbine engine applications," *51st AIAA Aerospace Sciences Meeting including the New Horizons Forum and Aerospace Exposition,* 2013.

[10] W. Cai and V. V. Bulatov, "Dislocation Core Effects on Mobility," in *Dislocations in Solids*, vol. 12, Elsevier, 2004, pp. 3-76.

[11] K. K. Chawla, Ceramic Matrix Composites, 2nd ed., Norwell, MA: Kluwer Academic Publishers, 2003.

[12] Accuratus, "Silicon Carbide, SiC Ceramic Properties," 2013. [Online]. Available: http://accuratus.com/silicar.html. [Accessed 28 May 2016].

[13] M. N. Rahaman, Ceramic Processing and Sintering, New York: Marcel Dekker, 2003.

[14] D. W. Richerson, Modern Ceramic Engineering: Properties, Processing, and Use in Design, 3rd ed., Boca Raton, Florida: CRC Press, 2006.

[15] D. C. Cranmer and D. W. Richerson, Mechanical Testing Methodology for Ceramic Design and Reliability, New York, New York: Marcel Dekker, inc., 1998, pp. 51-85.

[16] S. Ackert, "Engine maintenance concepts for financiers: elements of turbofan shop maintenance costs," *Aircraft Monitor,* pp. 1-42, September 2011.

[17] I. Ferro-Ceramic Grinding, "Ceramic Industry," 2012. [Online]. Available: https://www.ceramicindustry.com/ext/resources/pdfs/2013-CCD-Material-Charts.pdf. [Accessed 15 August 2016].

[18] F. Campbell, "Introduction to Composite Materials," in *Structural Composite Materials*, ASM International, 2010, pp. 1-27.

[19] I. M. Daniel and O. Ishai, Engineering Mechanics of Composite Materials, 2nd ed., New York: Oxford University Press, 2006.

[20] T. L. Anderson, "Ceramics and Ceramic composites," in *Fracture Mechanics: Fundamentals and Applications*, 3rd ed., Boca Raton, Florida: CRC Press, Taylor & Francis group, 2005, pp. 282-90.

[21] D. Koch, "Microstructural modeling and thermomechanical properties," in *Ceramic Matrix Composites: Fiber Reinforced Ceramics and their Applications*, Weinstein, Wiley, 2008, pp. 231-256.

[22] B. Budiansky, J. W. Hutchinson and A. G. Evans, "Matrix fracture in fiber-reinforced ceramics," *Journal of the Mechanics and Physics of Solids,* vol. 34, no. 2, pp. 167-189, 1986.

[23] M. Braginskya and C. P. Przybyla, "Simulation of crack propagation/deflection in ceramic matrix continuous fiber reinforced composites with weak interphase via the extended finite element method," *Composite Structures,* vol. 136, pp. 538-545, 2016.

[24] A. Evans and D. B. Marshall, "The mechanical behavior of ceramic matrix composites," *Acta Metallurgica,* vol. 37, no. 10, pp. 2567-2583, October 1989.

[25] S. Schmidt, S. Beyer, H. Knabe, H. Immich, R. Meistring and A. Gessler, "Advanced ceramic matrix composite materials for current and future propulsion technology applications," *Acta Astronautica,* vol. 55, no. 3-9, pp. 409-420, 2004.

[26] W. Krenkel, Ceramic Matrix Composites: Fiber Reinforced Ceramics and their Applications, Wiley, 2008.

[27] K. A. Keller, G. Jefferson and R. J. Kerans, "Oxide-Oxide Composites," in *Handbook of Ceramic Composites*, N. P. Bansal, Ed., Kluwer Academic Publishers, 2005, pp. 375-421.

[28] J. A. DiCarlo and H.-M. Yun, "Non-oxide (Silicon Carbide) Fibers," in *Handbook of Ceramic Composites*, N. P. Bansal, Ed., NASA Glenn Research Center, Kluwer Academic Publishers, 2005, pp. 33-52.

[29] J. Roy, S. Chandra, S. Das and S. and Maitra, "Oxidation behaviour of silicon carbide - a review," *Reviews on Advanced Material Science,* vol. 38, no. 1, pp. 29-39, 2014.

[30] R. Naslain, A. Guette, S. Rebillat, F. Le Gallet, F. Lamourox, L. Filipuzzi and C. Louchet, "Oxidation mechanisms and kinetics of SiC-matrix composites and their constituents," *Journal of Materials Science,* vol. 39, pp. 7303-7316, 2004.

[31] L. Li, "Fatigue life prediction of fiber-reinforced ceramic-matrix composites wiht different fiber preforms at room and elevated temperatures," *Materials,* vol. 9, no. 3, p. p. 207, 2016.

[32] B. Heidenreich, "CARBON FIBRE REINFORCED SIC MATERIALS BASED ON MELT INFILTRATION," in *Ceramic Matrix Composites: Fiber Reinforced Ceramics and their Applications*, Weinheim, Wiley, 2008, pp. 113-139.

[33] D. Christensen, "Fatigue Behavior of an Advanced SiC/SiC Composite at Elevated Temperature in Air and Steam," *MS Thesis. AFIT/GAE/ENY/09-D02,* December 2009.

[34] J. Delepasse, "Fatigue Behavior of an Advanced SiC/SiC Composite with an Oxidation Inhibited Matrix at 1200C in Air and in Steam," *MS thesis, AFIT/GAE/ENY/10-M07,* 2010.

[35] M. Lee, "Fatigue Behavior of an Advanced SiC/SiC Composite at 1300 C in Air and Steam," *Masters Thesis, Air Force Institute of Technology (AU),* 2016.

[36] ACP-Composites, "Woven Fabric Style Guide," 2010.

[37] N. P. Bansal and J. P. Singh, "Tensile strength and microstructure of Hi-Nicalon fibers extracted from Celsian Matrix Composites," *Advances in Ceramic Matrix Composites IV,* 1999.

[38] Rolls-Royce, "Personal correspondance," 2016.

[39] T. Jones, "Tension-Compression Fatigue of Hi-Nicalon/SiC Ceramic Matrix Composite at 1200°C in Air and in Steam," *MS Thesis, Air Force Institute of Technology, AFIT/GA/ENY/11-M09,* 2011.

[40] L. Li, "Comparisons of Damage Evolution between 2D C/SiC and SiC/SiC Ceramic-Matrix Composites under Tension-Tension Cyclic Fatigue Loading at Room and Elevated

Temperatures," *MDPI Materials,* vol. 9, pp. 844-72, 2016.

[41] W. T. Cissel, "Personal communication: Best practices in sample preparation for SEM characterization," 2016.

[42] P. L. Murthy, J. P. Gyekenyesi and S. Mital, "Reliability and Confidence Interval Analysis of a CMC Turbine Stator Vane," *International Conference on Computational & Experimental Engineering and Sciences,* pp. 8-9, 2008.

[43] Ruggles-Wrenn, "Personal correspondance," 2016.

[44] P. C. Paris, M. P. Gomez and W. P. Anderson, "A Rational Analytic Theory of Fatigue," *The Trend in Engineering,* vol. 13, pp. 9-14, 1961.

[45] S. Baste, "Fatigue Damage evaluation in ceramic matrix composites," *Review of progress in quantitative nondestructive evaluation,* vol. 14, pp. 2027-2034, 1995.

[46] V. Ramakrishnan and N. Jayaraman, "Fatigue behaviour of borosilicate glass-ceramic matrix, nicalon (silicon carbide) fibre composites," *Journal of materials science,* no. 28, pp. 5580-91, 1993.

[47] G. N. Morscher and V. V. Pujar, "Melt-infiltrated SIC composites for gas turbine engine applications," *ASME Turbo Expo Land, Sea and Air*, 2004.

[48] D. J. Green, An introduction to the mechanical properties of ceramics, D. Clarke, S. Suresh and I. Ward, Eds., Cambridge: Cambridge University Press, 1998, pp. 264-66.

[49] G. Morscher, G. Ojard, R. Miller, Y. Gowayed, U. Santhosh and J. Ahmad, "Tensile creep and fatigue of Sylramic-iBN melt-infiltrated SiC matrix composites: retained properties, damage development, and failure mechanisms," *Composite Science and Technology,* vol. 68, pp. 3305-13, 2008.

[50] K. Kollins and C. Przybyla, "Matrix Crack Detection using UV Dye Penetrant," WPAFB, OH, 2016.

[51] D. F. Lupton, J. Merker and F. Scholz, "The correct use of platinum in the XRF laboratory," in *19th Durham Conference on X-Ray Analysis*, University of Durham, England, 1995.

[52] T. L. Anderson, "Fatigue Crack Propagation," in *Fracture Mechanics: Fundamentals and Applications*, Third ed., Taylor & Francis, 2005, pp. 451-507.

REPORT DOCUMENTATION PAGE

Form Approved
OMB No. 074-0188

1. REPORT DATE *(DD-MM-YYYY)*	**2. REPORT TYPE**	**3. DATES COVERED** *(From – To)*
23-03-2017	Master's Thesis	January 2016 – March 2017

TITLE AND SUBTITLE
Fatigue behavior of an advanced melt-infiltrated SiC/SiC composite at 1200˚C in air and in steam

5a. CONTRACT NUMBER

5b. GRANT NUMBER

5c. PROGRAM ELEMENT NUMBER

6. AUTHOR(S)

Boucher, Nicholas J., Captain, USAF

5d. PROJECT NUMBER

5e. TASK NUMBER

5f. WORK UNIT NUMBER

7. PERFORMING ORGANIZATION NAMES(S) AND ADDRESS(S)
Air Force Institute of Technology
Graduate School of Engineering and Management (AFIT/ENY)
2950 Hobson Way, Building 640
WPAFB OH 45433-8865

8. PERFORMING ORGANIZATION REPORT NUMBER
AFIT-ENY-MS-17-M-242

9. SPONSORING/MONITORING AGENCY NAME(S) AND ADDRESS(ES)
Air Force Research Lab, Materials and Manufacturing Division
POC: Craig Przybyla (937-255-9396)
craig.przybyla@us.af.mil
Wright Patterson Air Force Base, OH 45433-7750

10. SPONSOR/MONITOR'S ACRONYM(S)
AFRL RXCCP

11. SPONSOR/MONITOR'S REPORT NUMBER(S)

12. DISTRIBUTION/AVAILABILITY STATEMENT
DISTRIBUTION STATEMENT A. APPROVED FOR PUBLIC RELEASE; DISTRIBUTION UNLIMITED

13. SUPPLEMENTARY NOTES

14. ABSTRACT
The tension-tension fatigue behavior of an advanced melt-infiltrated (MI) silicon carbide/silicon carbide (SiC/SiC) ceramic matrix composite (CMC) was investigated at 1200°C in air and in steam. The MI composite consisted of ten 0/90 plies of Hi-Nicalon-S SiC fibers woven in a five harness satin weave (5HSW), a CVI BN interphase to provide a weak fiber-matrix interphase, and a CVI SiC matrix layer followed by infiltration with SiC particulate slurry and molten silicon. Nine tensile specimens of the material were used in a pilot investigation of mechanical performance at elevated temperature. One specimen was used in a monotonic tensile test at 1200°C in air to determine tensile properties. The remaining specimens were tested in tension-tension fatigue; four were tested in air and four in steam. Tests were performed at 1200°C at 1.0 Hz with a stress ratio of minimum to maximum stress of R=0.05. Maximum stress ranged from 120 to 160 MPa in air and from 100 to 120 MPa in steam. Fatigue run-out was defined as 2×10^5 cycles. All specimens that achieved fatigue run-out were tested in tension to failure to evaluate retained strength and modulus. Strain accumulation and changes in modulus with cycles were measured to qualitatively evaluate damage development. The fatigue life was shorter in steam with a fatigue limit between 110 and 120 MPa. The fatigue limit in air was between 120 and 130 MPa. Specimens that achieved fatigue run-out retained 83-97% of their tensile strength. Post-test microstructure of the composite was examined in order to study damage and failure mechanisms.

15. SUBJECT TERMS
Ceramics, ceramic matrix composite, fatigue, high temperature, microstructure

16. SECURITY CLASSIFICATION OF:			**17. LIMITATION OF ABSTRACT**	**18. NUMBER OF PAGES**	**19a. NAME OF RESPONSIBLE PERSON**
a. REPORT	**b. ABSTRACT**	**c. THIS PAGE**			Marina Ruggles-Wrenn, AFIT/ENY
U	**U**	**U**	**UU**	144	**19b. TELEPHONE NUMBER** *(Include area code)* (937) 255-3636, ext 4641 (Marina.ruggles-wrenn@afit.edu)

Standard Form 298 (Rev. 8-98)
Prescribed by ANSI Std. Z39-18